Revista Brasileira de Ciências Mecânicas

Journal of the Brazilian Society of Mechanical Sciences

4

PUBLICAÇÃO DA ABCM - ASSOCIAÇÃO BRASILEIRA DE CIÊNCIAS MECÂNICAS

VOL. XVIII - No.4 - DECEMBER 1996 ISSN 0100-7386

REVISTA BRASILEIRA DE CIÊNCIAS MECÂNICAS
JOURNAL OF THE BRAZILIAN SOCIETY OF MECHANICAL SCIENCES
Vol. 1, Nº 1 (1979)-
Rio de Janeiro: Associação Brasileira de Ciências Mecânicas
Trimestral
Inclui referências bibliográficas.
1. Mecânica
ISSN-0100-7386

A REVISTA BRASILEIRA DE CIÊNCIAS MECÂNICA publica trabalhos que cobrem os vários aspectos da ciência e da tecnologia em Engenharia Mecânica, incluindo interfaces com as Engenharias Civil, Elétrica, Química, Naval, Nuclear, Aeroespacial Alimentos, Agrícola, Petróleo, Materiais, etc., bem como aplicações da Física e da Matemática à Mecânica.

INDEXED by Applied Mechanics Reviews and Engineering Information, Inc.

Publicação da / Published by
ASSOCIAÇÃO BRASILEIRA DE CIÊNCIAS MECÂNICAS
THE BRAZILIAN SOCIETY OF MECHANICAL SCIENCES

Secretária da ABCM : **Ana Lúcia Fróes de Souza**
Avenida Rio Branco, 124 18º Andar
20040-001 Rio de Janeiro RJ
Tel.: (021) 221-0438/Fax: (021) 222-7128

Presidente: **Carlos Alberto de Almeida**
Vice-Presidente: **Arthur Palmeira Ripper Neto**
Secretário Geral: **Hans Ingo Weber**
Diretor de Patrimônio: **Felipe Bastos de F. Rachid**
Secretário: **Paulo Batista Gonçalves**

Secretária da RBCM: **Maria de Fátima Alonso de Souza**
UNICAMP - FEM - C.P. 6122
13083-970 Campinas SP
Tel.: (019) 239-8353/Fax: (019) 239-3722

JOURNAL OF THE BRAZILIAN SOCIETY OF MECHANICAL SCIENCES
REVISTA BRASILEIRA DE CIÊNCIAS MECÂNICAS

REVISTA FINANCIADA COM RECURSOS DO
Programa de Apoio a Publicações Científicas
MCT CNPq FINEP

RBCM - J. of the Braz. Soc. Mechanical Sciences
Vol. XVIII - No.4 - 1996 - pp. 308-317

ISSN 0100-7386
Printed in Brazil

Position Control of Mechanical Manipulators Using the Optimal Root Locus

José Jaime da Cruz
Carlos Alberto Matuoka
Universidade de São Paulo
Escola Politécnica - C. P. 61548
Departamento de Engenharia Elétrica
05424-970 São Paulo, SP Brasil

Abstract

The design of a robust joint independent position control scheme for mechanical manipulators using a pole placement approach based on the Optimal Root Locus is discussed in this paper. Its performance is compared to that of the traditional PD structure, widely used in industrial applications, in situations where the last one is not recommended. The influence of various feedforward schemes is also analysed.
Keywords: Position Control, Mechanical Manipulators, Pole Placement, Optimal Root Locus, Linear Quadratic Regulator.

Introduction

The objective of this paper is to design a robust position control scheme for mechanical manipulators by using a pole placement technique based on the Optimal Root Locus Method (ORLM). The controller structure is joint independent (Spong and Vidyasagar, 1989).

The ORLM is a particular way of designing a Linear Quadratic Regulator (LQR) such that the closed-loop poles of the system can be allocated in pre-specified locations of the *s*-plane (Thompson, 1980). The use of the LQR as a basis for the design is motivated by its robustness characteristics: large stability margins, robustness in face of nonlinearities and tolerance to delays (Anderson and Moore, 1971).

A comparison of its performance with the traditional PD scheme is done, particularly in conditions where the use of this controller is not recommended, namely, when low gear ratio and/or high speeds are present.

The PD controller design is performed based on a linear dynamical model of the manipulator. An upper bound on the system closed-loop natural frequencies at 50% of the joint structural resonant frequencies is imposed (Luh, Walker and Paul, 1980).

The flexibility of the actuators axes is included in the ORLM design model to allow a larger bandwidth for the closed-loop system.

The performance comparison mentioned above is done through digital simulation. A planar two degree-of-freedom manipulator with revolute joints is used for this purpose. The simulation model is distinct from the nominal one in that the former includes the following aspects: existence of an unknown load at the end-effector, Coulomb friction at the joints and random errors in the parameters of the dynamical model.

The influence of various feedforward schemes in the global performance of the control system is also studied.

Mathematical Model

The simulation model will be discussed next since it contains as a particular case the nominal (design) model.

The equations of the joint torques have been obtained by the Newton-Euler method (Spong and Vidyasagar, 1989)

Manuscript received: December 1995. Technical Editor: Agenor de Toledo Fleury

$$\tau_1 = \left[m_1 d_1^2 + J_1 + m_2 l_1^2 + m_2 l_1 d_2 \cos(\phi_{s2} - \phi_{s1}) + Ml_1^2 + Ml_1 l_2 \cos(\phi_{s2} - \phi_{s1})\right] \ddot{\phi}_{s1} + \left[Ml_2^2 + Ml_1 l_2 \cos(\phi_{s2} - \phi_{s1}) + m_2 l_1 d_2 \cos(\phi_{s2} - \phi_{s1}) + m_2 d_2^2 + J_2\right] \ddot{\phi}_{s2} + \left[Ml_1 l_2 \sin(\phi_{s2} - \phi_{s1}) + m_2 l_1 d_2 \sin(\phi_{s2} - \phi_{s1})\right] (\dot{\phi}_{s1}^2 - \dot{\phi}_{s2}^2) + (m_1 d_1 + m_2 l_1 + Ml_1) g \cos(\phi_{s1}) + (m_2 + 2M) d_2 g \cos(\phi_{s2}) \quad (1)$$

and

$$\tau_2 = Ml_1 l_2 \cos(\phi_{s2} - \phi_{s1}) + m_2 l_1 d_2 \cos(\phi_{s2} - \phi_{s1}) \ddot{\phi}_{s1} + (Ml_2^2 + m_2 d_2^2 + J_2) \ddot{\phi}_{s2} + (Ml_1 l_2 + m_2 l_1 d_2) \sin(\phi_{s2} - \phi_{s1}) \dot{\phi}_{s1}^2 + (2M + m_2) d_2 g \cos(\phi_{s_1^2}), \quad (2)$$

where, for i=1,2 τ_i is the torque applied to joint i, ϕ_{si} is the angle of link i with the horizontal (Fig. 1) and, for each link i, m_i is its mass, l_i is its length, J_i is its moment of inertia with respect to the center of mass, d_i is the distance from its center of mass to joint i and M is the mass of the load at the end-effector. All these symbols correspond to the simulation model ("real" manipulator); g is the local gravity acceleration.

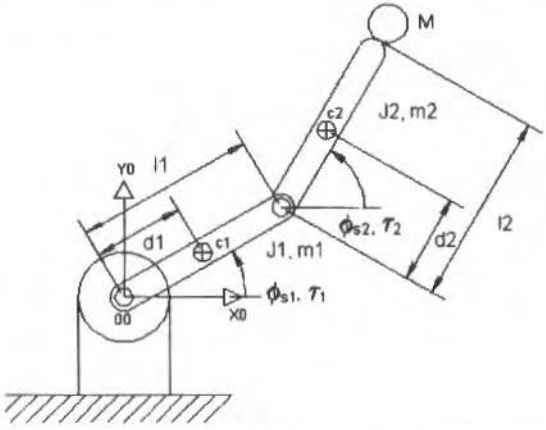

Fig. 1 Scheme of the Two Degree-of-freedom Manipulator

Those terms containing second order time derivatives of the joint angles correspond to inertial torques; those ones with first order derivatives are associated to the centrifugal effects; the terms that depend directly on the joint angles represent the gravitational torques.

Notice that the Coriolis torques do not appear in this formulation since the angles are measured in an inertial frame.

Let T_i, i=1,2, denote the torque on joint i, excluding the inertial torque corresponding to link i, i.e.

$$T_i = \tau_i - J_i \ddot{\phi}_{si} \quad (3)$$

Each actuator is assumed to be a DC motor coupled to a gear train through a flexible axis, as shown in Fig. 2. The motor torques T_{mi}, i=1,2 are taken as the control variables.

The dynamical model of joint i can be written as:

$$J_{mi}\ddot{\phi}_{mi} + B_{mi}\dot{\phi}_{mi} + K_{mi}(\phi_{mi} - \phi_{si}/n_i) + C_{mi}\,\mathrm{sgn}(\dot{\phi}_{mi}) = T_{mi} \tag{4}$$

$$J_i\ddot{\phi}_{si} + B_i\dot{\phi}_{si} - (K_{mi}/n_i)(\phi_{mi} - \phi_{si}/n_i) + T_i = 0 \tag{5}$$

where, for each actuator i, J_{mi} is the moment of inertia, ϕ_{mi} is the angular displacement, B_{mi} is the viscous friction coefficient, K_{mi} is the torsional spring constant of the axis, C_{mi} is the Coulomb friction torque, n_i is the gear ratio and B_i is the viscous friction coefficient corresponding to the link i. sgn(.) is the sign function.

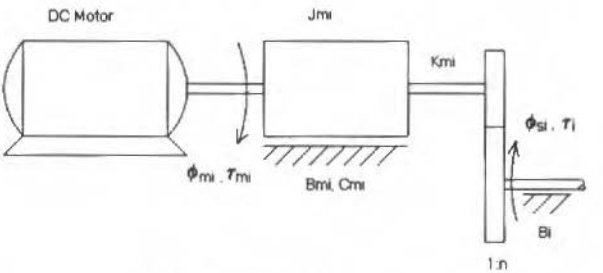

Fig. 2 Scheme of an Actuator

Notice that Eqs. 4 and 5 express the conditions of (dynamical) balance of the torque corresponding, respectively, to the motor and link sides of joint i.

The nominal model can be obtained from the simulation model above after elimination of the terms that contain the mass of the load at the end-effector (since its is admitted as unknown in the design) as well as those which represent the Coulomb friction effects. Furthermore, the nominal variables are denoted with the same symbols as above but with an over bar. For example, $\bar{\tau}_i$ and $\bar{m}_i$ are respectively the nominal torque at joint i and the nominal mass of link i.

In Luh, Walker and Paul, 1980, the PD controller design is based on the assumption that the actuator axis isinfinitely rigid (in fact the flexibility of the axis just imposes a constraint on the bandwidth of the system). This assumption means that

$$\phi_{mi} = \phi_{si}/n_i \tag{6}$$

Pole Placement Using the ORLM

Consider the LQR that results from the minimization of

$$J = \int_0^\infty [y^2(t) + ru^2(t)]\,dt \tag{7}$$

subject to

$$\dot{x}(t) = Ax(t) + bu(t), \qquad x(t_0) = x_0 \tag{8}$$

$$y(t) = hx(t), \tag{9}$$

where $x(t) \in \Re^n$, $u^t, y(t) \in \Re$, being the remaining dimensions compatible and $r > 0$. As usual, assume that (A,b) and (h,A) are controllable and observable respectively.

It is well known (see, e.g., Kwakernaak and Sivan, 1972) that the solution to this problem has the state feedback form

$$u(t) = -kx(t) \tag{10}$$

A procedure to choose r and h such that the locations of the closed-loop poles are pre-specified is presented in the following.

Let the polynomials

$$n(s) = b_p \prod_{i=1}^{p} (s - z_i) \tag{11}$$

and

$$d(s) = \prod_{i=1}^{n} (s - p_i), \tag{12}$$

where $p < n$, be defined by

$$\frac{n(s)}{d(s)} = h(sI - A)^{-1} b \tag{13}$$

and let D(s) be defined as

$$D(s) = d(s)\,d(-s) + r^{-1} n(s)\,n(-s) \tag{14}$$

The closed-loop poles $(\lambda_i(A - bk))$ are the left half plane roots of D(s) (Kailath, 1980).

Equation D(s) = 0 can be rewritten as

$$(-1)^{n-p_r-1} \frac{\Pi_{i=1}^{p} (s + z_i)(s - z_i)}{\Pi_{i=1}^{n} (s + p_i)(s - p_i)} = -1 \tag{15}$$

Hence for varying r the closed-loop poles can be obtained using the classical root locus techniques (Ogata, 1982), with the parameter $(-1)^{n-p_r-1}$ playing the role of the gain.

In this way, given n(s)/d(s), we take its poles and zeros as well as their symmetrical ones with respect to the imaginary axis and then draw the root locus following the classical rules. The left half plane portion of the plot represents the LQR poles.

When $r \to 0^+$, the roots of D(s) that remain finite tend to the zeros of n(s)n(-s); those ones that go to ∞, follow a Butterworth pattern (Kailath, 1980)

Since the poles p_i correspond to the eigenvalues of the open-loop system matrix A, they are fixed. On the other hand the zeros z_i depend on vector h which can be considered as a design parameter.

In this way, once the p desired closed-loop poles $(z_1, z_2, \ldots, z_p)$ have been chosen, the pole placement procedure using the ORLM can be reduced to the determination of the vector h which can be summarized as (Thompson, 1980):

- if (A,b) is in the cannonical controllable form, h is given by

$$h = [b_0 \; b_1 \ldots b_p], \tag{16}$$

where b_i is the i-th degree coefficient of n(s);

- otherwise,

$$h = [0 \ldots 01]\left[x_1 \ldots x_p \; b \; Ab \ldots A^{n-p-1}b\right]^{-1}, \tag{17}$$

where

$$x_i = (z_i I - A)^{-1} b \qquad (i = 1, 2, \ldots, p) \tag{18}$$

Controller Designs

PD Controller Design

The block diagram of the control system for the i-th joint is shown in Fig. 3 (Luh, Walker and Paul, 1980) where ϕ_{si} is the reference signal, K_{ti} is the gain of the tachometer that measures the angular velocity of the motor axis, $K_{\phi i}$ and K_{1i} are respectively the proportional and derivative gains of the controller, K_{Ii} is the torque constant of the motor, R_i is the armature resistance, K_{bi} is the back electromotive force constant and T'_{mi} is the feedforward torque.

From Fig. 3 the actual motor torque can be written as

$$T_{mi} = \frac{K_{Ii}}{R_i}\left[K_{\phi i}(\bar{\phi}_{si} - \phi_{si}) - (K_{bi} + K_{1i}K_{ti})\dot{\phi}_{mi}\right] - n_i\tau_i - n_i^2 B_i \dot{\phi}_{mi} + T'_{mi} \tag{19}$$

$K_{\phi i}$ and K_{1i} are usually set such that: i) the closed-loop poles must be such that the natural undamped frequency must be less than or equal to 50% of the structural resonant frequency of the actuator axis; ii) the closed-loop poles must be critically damped. These conditions lead to (for details see Luh et al., 1980):

$$K_{\phi i} \le \frac{K_{mi}R_i}{4n_iK_{Ii}} \tag{20}$$

and

$$K_{1i} \ge R_i \; \frac{\sqrt{K_{mi}J_{mi} - B_{mi}}}{K_{Ii}K_{ti}} - \frac{K_{bi}}{K_{ti}} \tag{21}$$

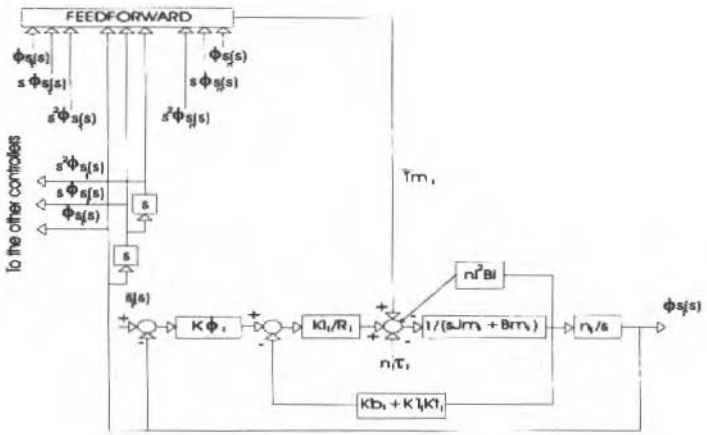

Fig. 3 Control System Diagram for Joint i

The feddforward torque T'_{mi} is evaluated using the link generalized coordinates and is based on pre-calculated estimates of the inertia, gravitational, Coriolis, centrifugal and viscous torques (Luh et al., 1980).

Controller Design Using the ORLM

The following state vector has been adopted in this case:

$$x^{(i)} = \left[\phi_{mi} - \bar{\phi}_{mi} \;\; \phi_{si} - \bar{\phi}_{si} \;\; \dot{\phi}_{mi} - \hat{\dot{\phi}}_{mi} \;\; \dot{\phi}_{si} - \hat{\dot{\phi}}_{si} \;\; \int(\phi_{si} - \bar{\phi}_{si})\,dt\right] \tag{22}$$

The last element of the vector represents an integration included to guarantee that the steady-state position of the i-th link coincides with the nominal (desired) one for a step command.

The control variable has been taken as

$$u^{(i)} = T_{mi} - \bar{T}_{mi}, \tag{23}$$

which has the nature of a correction torque.

With the above choices and considering T_i as a disturbance in the nominal version of Eqs. 4 and 5 it is easy to obtain the following state model:

$$\dot{x}^{(i)} = A^{(i)} x^{(i)} + B^{(i)} u^{(i)} \tag{24}$$

where

$$A^{(i)} = \begin{bmatrix} 0 & 0 & 1 & 0 & 0 \\ 0 & 0 & 0 & 1 & 0 \\ -\bar{K}_{mi}/\bar{J}_{mi} & \bar{K}_{mi}/(n_i\bar{J}_{mi}) & -\bar{B}_{mi}/\bar{J}_{mi} & 0 & 0 \\ \bar{K}_{mi}/(n_i\bar{J}_i) & -\bar{K}_{mi}/(n_i^2\bar{J}_i) & 0 & -\bar{B}_i/\bar{J}_i & 0 \\ 0 & 1 & 0 & 0 & 0 \end{bmatrix} \quad B^{(i)} = \begin{bmatrix} 0 \\ 0 \\ 1/\bar{J}_{mi} \\ 0 \\ 0 \end{bmatrix} \tag{25}$$

Then a set of p = 4 closed-loop poles is chosen on the negative real axis from 1.5 to 2.0 times faster than those corresponding to the PD controller in order to include the structural resonant frequency of the actuator axis in the bandwidth of the closed-loop system. Finally the methodology described in section 3 is applied to find a gain vector k such that

$$u^{(i)} = -kx^{(i)} \tag{26}$$

Notice that in the proposed scheme (see Fig. 4) the nominal motor torque $\bar{T}_{mi}$ represents a feedforward control signal. According to the nominal model described, $\bar{T}_{mi}$ is given by

$$\bar{T}_{mi} = \bar{J}_{mi}\ddot{\bar{\phi}}_{mi} + \bar{B}_{mi}\hat{\dot{\phi}}_{mi} + \bar{K}_{mi}(\bar{\phi}_{mi} - \bar{\phi}_{si}/n_i) \tag{27}$$

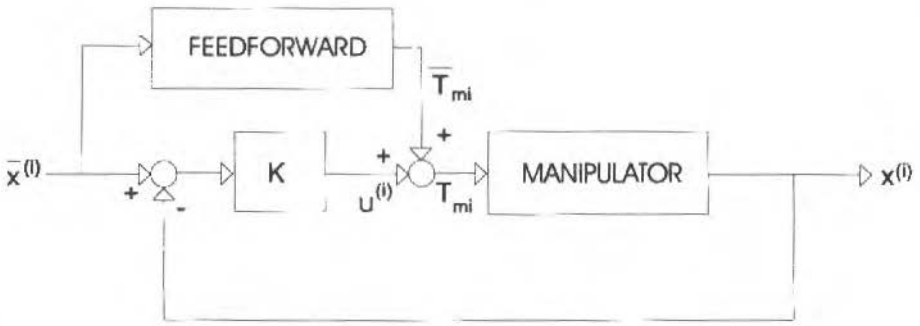

Fig. 4 Block Diagram of the ORLM Controller.

In the position control problem the function $\bar{\phi}_{si}(t)$ is given. To compute $\bar{T}_{mi}$ it should be noticed that

$$\bar{\phi}_{mi} = \frac{n_i}{\bar{K}_{mi}} (\bar{J}_i \ddot{\bar{\phi}}_{si} + \bar{B}_i \dot{\bar{\phi}}_{si} + \bar{T}_i) + \bar{\phi}_{si}/n_i \tag{28}$$

and that both $\dot{\bar{\phi}}_{mi}$ and $\ddot{\bar{\phi}}_{mi}$ can be evaluated analytically by successively differentiating the last expression with respect to time.

In view of Eqs. 1-2 it is evident that the computation of $\dot{\bar{\tau}}_i$ and $\ddot{\bar{\tau}}_i$ is an extremely laborious task (even in the case of a two degree-of-freedom manipulator) (Matuoka, 1993).

For the reasons exposed above this scheme is called here full analytical feeedforward.

Motivated by this structure and by the computational burden to evaluate $\bar{T}_{mi}$, three alternative schemes have been tested:

- Full numerical feedforward

An efficient way of evaluating $\dot{\bar{\phi}}_{mi}$ and $\ddot{\bar{\phi}}_{mi}$ is through a numerical approach. An approximate differentiation scheme based on the Newton interpolation formula (Demidovich and Baron, 1973) has been used.

Recall that the functions to be differentiated have not to be measured but just evaluated numerically being thus not affected by significant noise. For this reason the numerical derivatives match closely the analytical ones (Matuoka, 1993).

- Simplified feedforward

In this case the axis is considered to be infinitely rigid. Hence, given $\bar{\phi}_{si}(t)$, we compute

$$\bar{\phi}_{mi} = \bar{\phi}_{si}/n_i \tag{29}$$

and

$$\bar{T}_{mi} = J_{mi} \ddot{\bar{\phi}}_{mi} + \bar{B}_{mi} \dot{\bar{\phi}}_{mi} \tag{30}$$

- No feedforward

This is the simplest case and corresponds obviously to take

$$\bar{T}_{mi} = 0 \tag{31}$$

Results

The values of the nominal model parameters are shown in Table 1.

Table 1 Parameters of the Nominal Model

Parameter	Value	Parameter	Value
$l_{1,2}$	0.75 m	$d_{1,2}$	0.375 m
$m_{1,2}$	3.0 kg	$J_{l1,2}$	0.5625 kg.m^2
$J_{m1,2}$	0.0233 kg.m^2	$R_{1,2}$	0.91 Ω
$K_{t1,2}$	2.0 Nm/A	$B_{m1,2}$	8.09E-05 Nms/rad
$K_{t1,2}$	0.05062 Vs/rad	$K_{b1,2}$	0.10123 Vs/rad
$B_{1,2}$	8.09E-05 Nms/rad	$K_{m1,2}$	574.9 Nm/rad
$n_{1,2}$	0.5		

The values of the parameters of the simulation model have been obtained by adding a 5 % pseudo-random error to the corresponding nominal ones (except $n_{1,2}$). Furthermore the load at the end-effector has been taken as M=1.0 kg and the Coulomb friction magnitude C_{mi}, 0.5% of the maximum gravitational torque at joint i.

The value of the gear ratio (2:1) has been chosen intentionally low (in practice, it is usually of the order of 100:1) to permit the comparison of controller performances in cases where joint independent control is not recommended (Spong and Vidyasagar, 1989). Obviously in a concrete design problem the use of such a gear ratio would require the choice of the actuators to be reviewed. This is not the case here since we are only interested in the comparison of controllers performance.

The PD controller design produced a double pole at -75s^{-1} for the system of Fig. 3. In view of this the design parameters z_i of the ORLM have been chosen as {-100; -110; -120; -130}(s^{-1}). Joint 1 is dynamically more complex and hence harder to control. For this reason only the results corresponding to it are presented in the following.

The simulation has been carried out for a position reference signal composed of a pair of parabollic arcs corresponding to two acceleration pulses with duration 0.5 sec and amplitude $+\pi/9$ and $-\pi/9$rd/sec^2, respectively. The ORLM controller has been simulated with no feedforward.

Figures 5 to 8 show the results obtained. It can be noted that the position errors are of the order of 10^3 times smaller for the ORLM controller, although the control effort has similar magnitudes for both controllers. Hence the performance of the ORLM controller is significantly better than that of the PD controller.

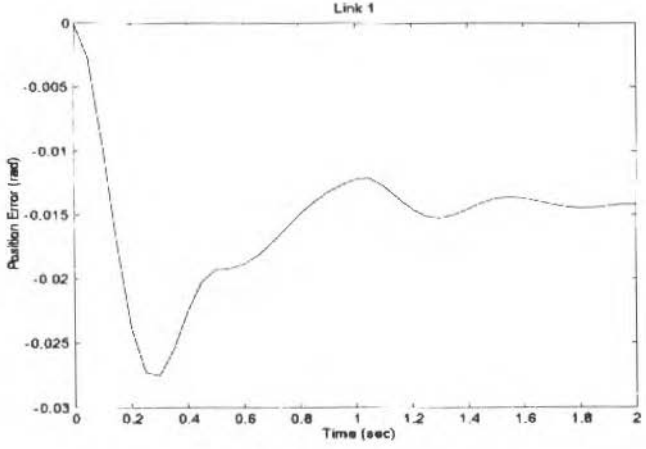

Fig. 5 Position Error - PD Controller

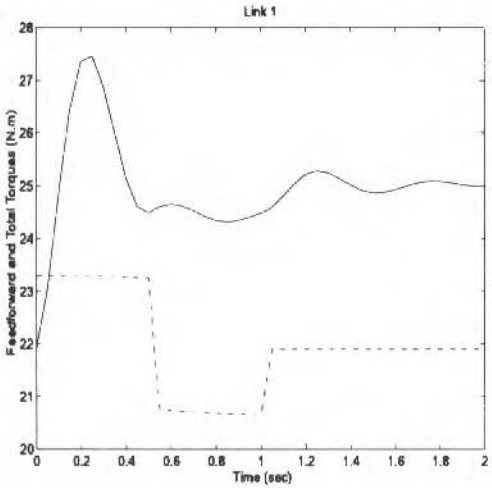

Fig. 6 Total Torque (continuous line) and Feedforward Torque (dashed line) - PD Controller

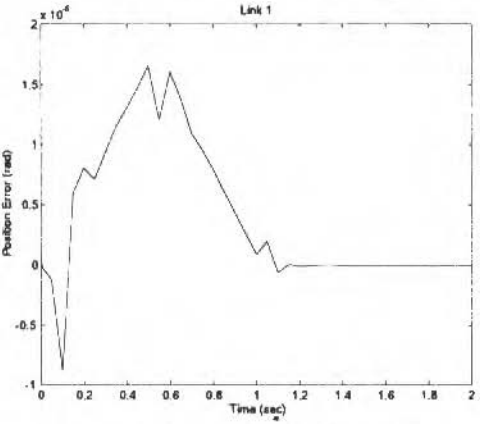

Fig. 7 Position Error - ORLM Controller

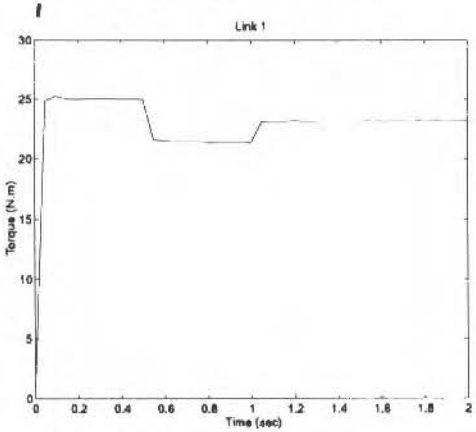

Fig. 8 Total Torque - ORLM Controller

Furthermore the tests showed that a good performance of the PD controller required the presence of a feedforward term.

All feedforward schemes described in have been tested for the ORLM controller. The results showed that the feedforward terms could be eliminated since they did not improve the performance when compared to the case with no feedforward. This fact has thus verified in practice the robustness of the LQR in face of model uncertainties and nonlinearities.

Both full analytical and numerical computation schemes gave practically identical results for the feedforward term. Hence, if the feedforward scheme had been required, the numerical approach should be taken in view of its simplicity, particularly in the case of manipulators with a large number of degrees of freedom.

In the simplified feedforward scheme the magnitude of the feedforward torque is relatively small when compared to the full feedforward scheme. The axis infinite rigidity is the characteristic of the simplified scheme responsible for this behavior. So under this point of view we can say that the simplified feedforward scheme is closer to the the case with no feedforward.

Tests were also performed for the case where the end-effector describes a spiral trajectory. Results obtained confirmed the conclusions above (Matuoka, 1993).

Conclusions

The results obtained with the ORLM controller indicate that it must be considered as an alternative to the solution of the position control problem in cases where the PD scheme is not appropriate. Low gear ratio and high speed motion of the links are typical situations where this occurs.

Since the ORLM controller has the structure of a state feedback, both position and velocity must be measured for each actuator axis and each link axis. One alternative currently under investigation considers the use of a Kalman Filter in such a way as to recover the original robustness properties of the LQR as in the LQG/LTR procedure (Doyle and Stein, 1981).

With respect to the simulations performed, it should be emphasized that the test conditions can be considered severe with respect to modeling errors. The simulation model (but not the nominal model) included a load at the end-effector, Coulomb friction at the actuators as well as random errors in the model parameters. The tests have clearly confirmed in practice the well-known robustness characteristics of the LQR.

Acknowledgments

The first author wishes to express his gratitude to CNPq - Conselho Nacional de Desenvolvimento Científico e Tecnológico (Proc. No. 304071/85-4(NV)) and to FAPESP - Fundação de Amparo à Pesquisa do Estado de São Paulo (Proc. No. 91/0508-3).

References

Anderson, B.D.O., and Moore, J.B., 1971 "Linear Optimal Control", Prentice-Hall, Englewood Cliffs, NJ.
Demidovich B.P., and Maron, I.A., 1973, "Computational Mathematics", MIR, Moscow.
Doyle, J.C. and Stein, G., Feb 1981, "Multivariable Feedback Design: Concepts for a Classical/Modern Synthesis" . IEEE Trans. Auto. Contr., Vol. AC-26.
Kailath, T., 1980, "Linear Systems", Prentice-Hall, Englewood Cliffs, NJ.
Kwakernaak H. and Sivan R., 1972, "Linear Optimal Control", Wiley, New York, NY.
Luh, J.Y.S., Walker, M.W. and Paul, R.P., 1980, "On-Line Computational Scheme for Mechanical Manipulators". Trans. ASME J. Dyn. Syst. Meas. Contr.
Matuoka, C.A., 1993, "Controle de Posição de Manipuladores Mecânicos Usando o Método do Lugar das Raízes Otimo", Tese de Mestrado, EPUSP, São Paulo, SP.
Ogata, K., 1982, "Engenharia de Controle Moderno", Prentice Hall do Brasil, Rio de Janeiro, RJ.
Paul, R.P., 1981, "Robot Manipulators: Mathematics, Programming and Control", MIT Press, Cambridge, MA.
Spong, M.W. and Vidyasagar, M., 1989, "Robot Dynamics and Control", Wiley International, New York, NY.
Thompson, P.M., 1980, "Multivariable Control Systems -The Optimal Root Locus (Lecture Notes)", MIT, Cambridge, MA.

RBCM - J. of the Braz. Soc. Mechanical Sciences
Vol. XVIII - No.4 - 1996 - pp. 318-329

ISSN 0100-7386
Printed in Brazil

Dinâmica do Rodeiro Ferroviário

Railway Wheelset Dynamics

Roberto Spinola Barbosa
IPT - Instituto de Pesquisas Tecnológicas
Divisão de Tecnologia de Transportes - C.P. 7141
01064-970 São Paulo, SP Brasil

Alvaro Costa Neto
USP - Universidade de São Paulo
Escola de Engenharia de São Carlos
Departamento de Engenharia Mecânica - C.P. 359
13560-970 São Carlos, SP Brasil

Abstract

A velocity parametrized railway wheelset model was produced for dynamic behavior analysis. Lateral wheelset excursion related to the track is the first vibration mode. It was observed in the eigen-properties that the wave length of this movement is approximately constant and dependent on the wheel conicity. Modal damping of the first mode is inversely proportional to velocity and becames negative for high speed, resulting on system instability. At low speed, real, distinct and overdamped second mode eigenvalues are inversely proportional to velocity and strongly coupled with contact stiffness. Dynamic wheelset behavior through a variable track trajetory may be observed during model simulation.
Keywords: Railway Wheelset, Dynamic Behavior Analysis, Simulation

Resumo

Foi elaborado um modelo linear do rodeiro ferroviário parametrizado em função da velocidade para análise de propriedades e avaliação do comportamento dinâmico. O primeiro modo de vibrar corresponde ao movimento de passeio lateral do rodeiro em relação a via. Observa-se nas autopropriedades que este modo possui comprimento de onda de movimento no espaço aproximadamente constante e fortemente dependente da conicidade da pista de rolamento da roda. O amortecimento modal é inversamente proporcional à velocidade e fica negativo para velocidades elevadas tornando o sistema instável. O segundo modo de vibrar, sobreamortecido, possui, a baixas velocidades, raízes reais distintas inversamente proporcionais à velocidade e fortemente acoplado com a rigidez das forças de contato. A simulação deste modelo permite visualizar o comportamento dinâmico do rodeiro em sua interação com a via férrea para um percurso com trajetória variável.
Palavras-chave: Rodeiro Ferroviário, Comportamento Dinâmico, Modelo linear.

Nomenclatura

- n = ordem do sistema;
- u_y = coordenada de deslocamento lateral;
- φ_r = coordenada angular;
- m = massa do rodeiro;
- Θ = momento de inercia;
- T_{xl} = Força de Contato;
- ϑ_x = Velocidades relativas;
- λ = conicidade da pista de rolamento da roda;
- r = vetor de coordenadas;
- V_o = velocidade de translação;
- f = forçamento externo;
- t = tempo;
- Δt = intervalo de cálculo;
- α = ângulo de kick;
- T = intervalo de tempo;
- t_k = tempo no k-éssimo intervalo de tempo T;
- ζ = fator de amortecimento;
- δ_L = comprimento de onda;
- λ_i = i-éssimo autovalor;
- $\{x\}$ = representação vetorial de estado de espaço;
- $\{x\}^t$ = vetor de estado transposto;
- $\{\dot{x}\}$ = 1ª derivada do vetor de estado;
- $\{u\}$ = vetor de forçamento externo;
- $\{f\}$ = vetor de força externa;
- $\{v\}$ = autovetor do sistema 2n;
- $[M]$ = matriz de massa;
- $[C]$ = matriz de amortecimento;
- $[K]$ = matriz de rigidez;
- $[R]$ = matriz modal;
- $[A]$ = matriz dinâmica do sistema;
- $[I]$ = matriz identidade;
- $[\Phi]$ = matriz Fundamental;
- $[\Lambda]$ = matriz diagonal da exponencial dos autovalores;

Manuscript received: January 1996. Technical Editor: Agenor de Toledo Fleury

Introdução

A inscrição de um rodeiro ferroviário em curvas se faz com o auxílio de um inteligente sistema dinâmico estabelecido pela conicidade da pista de rolamento das rodas que produzem diferentes raios de rolamento para cada roda em função do deslocamento lateral do rodeiro.

Um observador trafegando junto ao rodeiro em uma trajetória retilínea percebe que a via férrea se desloca lateralmente quando passa sobre uma trajetória curva. Este deslocamento lateral relativo faz com que o raio de rolamento da roda externa, devido à conicidade, seja maior do que o raio da roda interna à curva. Desta forma, como a rotação angular do rodeiro é idêntica para as duas rodas (rodeiro considerado rígido não havendo, portanto, movimento rotacional diferencial entre as rodas) haverá produção de forças longitudinais diferenciadas entre os pontos de contato de cada roda. Estas forças tenderão a produzir um ângulo de ataque do rodeiro em relação à direção da via férrea buscando a inscrição do rodeiro na curva.

Este efeito restituidor garante a centralização do rodeiro quando trafegar em trajetória retilínea pelas irregularidades da via férrea. Induz também a contribuição individual de cada roda na geração das forças laterais (centrípetas) necessárias para inscrição de trajetória curvilínea (melhorando inclusive a segurança contra o descarrilamento) garantindo a guiagem automática do rodeiro em curvas. Esta propriedade, entretanto, resulta num sistema dinâmico com freqüência natural definida, amortecimento modal inversamente proporcional à velocidade e podendo apresentar velocidade crítica acima da qual o sistema torna-se instável.

Equacionamento

O rodeiro ferroviário pode ser representado pelo sistema mecânico mostrado na Fig. 1. O sistema de referência utilizado está vinculado à estrutura do truque e trafega junto a este a uma velocidade constante V_0. O rodeiro foi modelado com dois graus (n=2) de liberdade: deslocamento lateral do rodeiro em relação à via u_y e rotação angular φ_z na direção z conhecido como ângulo de yaw.

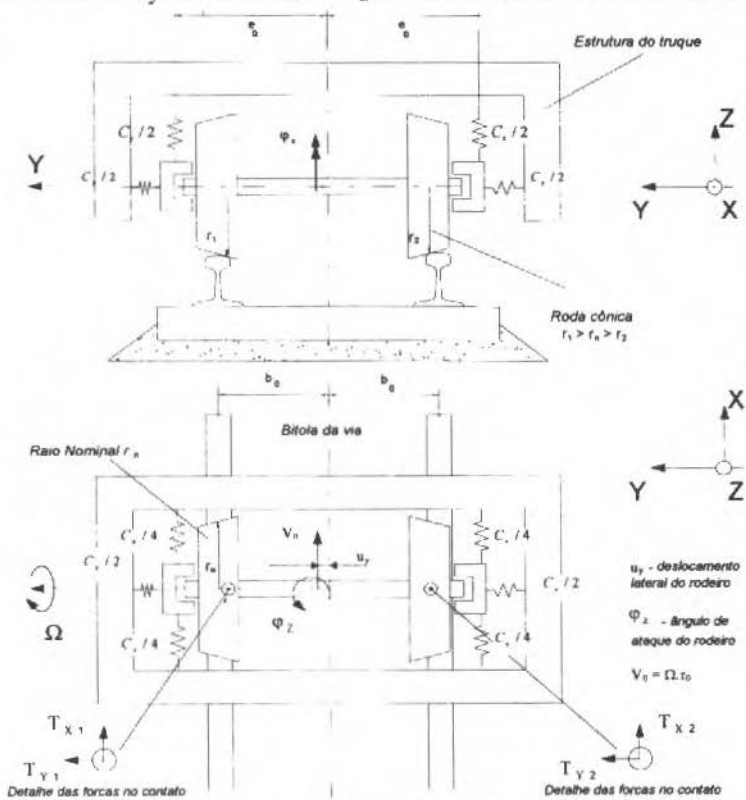

Fig. 1 Elementos do Rodeiro Ferroviário

A obtenção das equações de movimento deste sistema pode ser feita de várias maneiras. Para modelos simples com poucos graus de liberdade, as equações podem ser escritas manualmente sem muita dificuldade. Entretanto, para modelos mais complexos e extensos, esta atividade torna-se desgastante e passível de erros. Programas computacionais para Sistemas Multicorpos (MBS) permitem a geração automática das equações de movimento para sistemas complexos e não lineares com facilidade, rapidez e segurança.

Neste caso as equações são obtidas manualmente, assumindo pequenos deslocamentos e desconsiderando os efeitos inerciais do truque, a partir da aplicação da 2ª lei de Newton sobre o rodeiro nas direções dos graus de liberdade, como pode ser observado na Eq. (1).

$$\begin{bmatrix} m & 0 \\ 0 & \Theta \end{bmatrix} \begin{Bmatrix} \ddot{u}_y \\ \ddot{\varphi}_z \end{Bmatrix} + \begin{vmatrix} c_y & 0 \\ 0 & c_x e_o^2 \end{vmatrix} \begin{Bmatrix} u_y \\ \varphi_z \end{Bmatrix} + \begin{Bmatrix} T_{y1} + T_{y2} \\ b_o (T_{x1} - T_{x2}) \end{Bmatrix} = \begin{Bmatrix} F_y \\ T_\varphi \end{Bmatrix} \tag{1}$$

As forças desenvolvidas no contato $\mathbf{T_{xi}}$ e $\mathbf{T_{yi}}$ entram do lado direito da equação como forçamento externo. Entretanto, devido a mecânica de contato, estas forças são proporcionais à velocidade relativa entre as superfícies de contato, dependente dos graus de liberdade e suas derivadas podendo, portanto, tornarem-se parte integrante do sistema passando para o lado esquerdo da equação geral.

De maneira simplificada, conforme a teoria de mecânico de contato, pode-se exprimir as forças nas direções longitudinal T_{xi} e lateral T_{yi} como sendo proporcionais às velocidades relativas ϑ_{xi} e ϑ_{yi} entre as superfícies de contato roda/trilho. As constantes de proporcionalidade, k_x e k_y, que relacionam os micro-escorregamentos entre as superfícies (conhecidos como creep) e as forças são expressas da seguinte forma:

$$T_{x1} = k_x \frac{\vartheta_{x1}}{V_o} \quad \text{e} \quad T_{x2} = k_x \frac{\vartheta_{x2}}{V_o} \tag{2}$$

$$T_{y1} = k_y \frac{\vartheta_{y1}}{V_o} \quad \text{e} \quad T_{y2} = k_y \frac{\vartheta_{y2}}{V_o} \tag{3}$$

Os valores de micro-escorregamento resultantes das velocidades relativas no contato são função das coordenadas do sistema e suas derivadas, da conicidade da pista de rolamento λ, raio nominal de rolamento r_o, semidistância dos pontos de contato $\mathbf{b_0}$. Como $r_1 = r_o + \lambda\, u_y$ e $r_2 = r_o - \lambda\, u_y$ as forças são obtidas pelas expressões a seguir:

$$T_{x1} = -k_x \left(\frac{\lambda u_y}{r_o} + \frac{\dot{\varphi}_z b_o}{V_o} \right) \quad \text{e} \quad T_{x2} = +k_x \left(\frac{\lambda u_y}{r_o} + \frac{\dot{\varphi}_z b_o}{V_o} \right) \tag{4}$$

$$T_{y1} = T_{y2} = k_y \left(-\varphi_z + \frac{\dot{u}_y}{V_o} \right) \tag{5}$$

Substituindo estes valores na Eq. (1) e rearranjando os termos de forma matricial, tem-se a seguinte expressão:

$$\begin{bmatrix} m & 0 \\ 0 & \Theta \end{bmatrix} \begin{Bmatrix} \ddot{u}_y \\ \ddot{\varphi}_z \end{Bmatrix} + \frac{1}{V_o} \begin{bmatrix} 2k_y & 0 \\ 0 & 2k_x b_o^2 \end{bmatrix} \begin{Bmatrix} \dot{u}_y \\ \dot{\varphi}_z \end{Bmatrix} + \begin{bmatrix} c_y & -2k_y \\ 2k_x \lambda b_o / r_o & c_x e_o^2 \end{bmatrix} \begin{Bmatrix} u_y \\ \varphi_z \end{Bmatrix} = \begin{Bmatrix} F_y \\ T_\varphi \end{Bmatrix} \tag{6}$$

Observa-se que após a inclusão das forças de contato aparece o termo de primeira derivada do vetor de coordenadas, revelando que o sistema possui amortecimento relacionado com as propriedades de contato e inversamente proporcional à velocidade.

A Equação 6 é valida apenas para trajetórias retilíneas e pequenos deslocamentos (angular e lateral). Durante a inscrição de uma curva, a trajetória do rodeiro se altera em função da solicitação externa imposta pela variação da posição da via no plano, combinada com as características de resposta do próprio sistema. Considerando a situação de regime da inscrição em uma curva, a força centrípeta aplicada sobre o rodeiro e o torque proveniente da rotação deste em relação ao centro da curva, correspondente as força externas $\mathbf{F_y}$ e T_φ, e aparecem do lado direito da equação.

Na situação de regime, durante a inscrição de uma curva de raio **R**, a solicitação externa sobre o rodeiro é composta de duas parcelas: aceleração centrípeta expressa por V^2/R e o torque produzido pela velocidade angular de regime do rodeiro $\Psi = V_o/R$, conforme Fig. 2.

Como o rodeiro é considerado rígido, o acréscimo de velocidade relativa para cada roda devido à velocidade angular na curva, é dado por: $\vartheta_{x1} = V_o b_o/R$ e $\vartheta_{x2} = V_o b_o/R$ (pois $\vartheta_x = \Psi b_o$). A força centrípeta e o torque decorrente do contato, normalizadas por V_o, são introduzidas do lado direito da Eq. 6, resultando na equação de movimento do sistema mecânico em curvas:

$$\begin{bmatrix} m & 0 \\ 0 & \Theta \end{bmatrix} \begin{Bmatrix} \ddot{u}_y \\ \ddot{\varphi}_z \end{Bmatrix} + \frac{1}{V_o} \begin{bmatrix} 2k_y & 0 \\ 0 & 2k_x b_o^2 \end{bmatrix} \begin{Bmatrix} \dot{u}_y \\ \dot{\varphi}_z \end{Bmatrix} + \begin{bmatrix} c_y & -2k_y \\ 2k_x \lambda b_o / r_o & c_x e_o^2 \end{bmatrix} \begin{Bmatrix} F_y \\ T_\varphi \end{Bmatrix} + \begin{Bmatrix} mV_o^2/R \\ 2k_x b_o^2/R \end{Bmatrix} \tag{7}$$

adotando $r^t = \{u_y \ \varphi_z\}^t$, $f^t = \{(F_y + mV_o^2/R) \ (T_\varphi + 2k_x b_o^2/R)\}^t$ e resumindo a expressão matricial, obtém-se:

$$[M]\{\ddot{r}\} + \frac{1}{V_o}[C]\{\dot{r}\} + [K]\{r\} = \{f\} \tag{8}$$

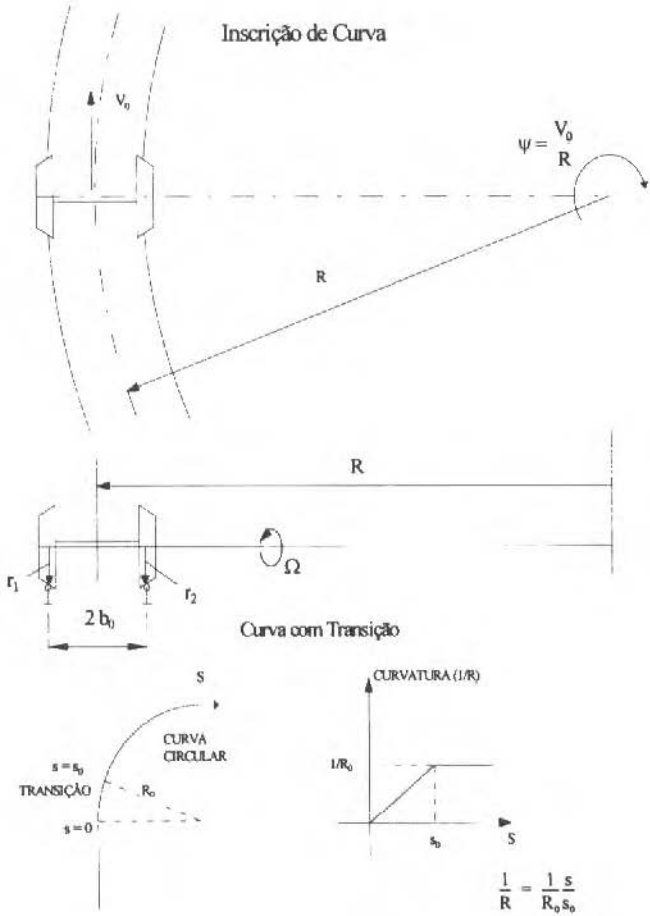

Fig. 2 Descrição de Curva Circular e de Transição

Solução do Sistema de Equações

A solução do sistema de equações diferenciais de segunda ordem é feita com a redução do grau do sistema passando para a representação de estado de espaço com $x^t = \{\ddot{u}_y\ \ddot{\varphi}_z\ u_y\ \varphi_z\}^t$, sua respectiva derivada $\dot{x}^t = \{\dddot{u}_y\ \dddot{\varphi}_z\ \dot{u}_y\ \dot{\varphi}_z\}^t$ e $u^t = \{f\ 0\}^t$, resultando num sistema contínuo de ordem 2n do tipo $\dot{x} = Ax + Bu$. Neste caso obtém-se:

$$\{x\} = \begin{bmatrix} -\frac{1}{V_o}[M]^{-1}[C] & -[M]^{-1}[K] \\ [I] & [0] \end{bmatrix} \{x\} + \begin{bmatrix} [M]^{-1} \\ [0] \end{bmatrix} \{u\} \tag{9}$$

Para sistemas dinâmicos homogêneos com coeficientes constantes a solução temporal contínua direta (Gasch e Knothe, 1987), que leva o vetor de estado $\{x\}_{t_o}$ de condições iniciais no tempo t_o, para o tempo t qualquer, é dada por:

$$\{x\}_t = [\Phi]_{(t-t_o)} \{x\}_{t_o} \tag{10}$$

A forma construtiva da matriz fundamental $[\Phi]$ para sistemas amortecidos é expressa por seus autovalores arranjados de forma matricial multiplicados pela matriz modal:

$$[\Phi]_{(t-t_o)} = [R]\,[\Lambda]_{(t-t_o)}\,[R]^{-1} \tag{11}$$

onde a matriz diagonal $[\Lambda]$ é constituída da exponencial dos autovalores λ_i como segue:

$$[\Lambda] = \begin{bmatrix} e^{\lambda_1(t-t_o)} & 0 & : & 0 \\ 0 & e^{\lambda_2(t-t_o)} & : & 0 \\ .. & .. & & .. \\ 0 & 0 & : & e^{\lambda_{2n}(t-t_o)} \end{bmatrix} \tag{12}$$

e a matriz modal [**R**] constituída dos 2n autovetores $\{v\}$ da seguinte forma:

$$[R] = \left[\{r_1\}\ \{r_2\} \ldots \{r_n\} \right] = \begin{bmatrix} \lambda_1 v_1 & \lambda_2 v_2 & \ldots \lambda_{2n} v_{2n} \\ v_1 & v_2 & \ldots v_{2n} \end{bmatrix} \tag{13}$$

A solução completa do sistema de equações diferenciais ordinárias não homogêneas pode ser obtida de forma contínua no tempo com auxílio da integral de convolução para uma excitação externa $\{u\}$ qualquer a partir das condições iniciais $\{x\}_{(to)}$ do sistema por:

$$\{x\}_{(t-t_o)} = [\Phi]_{(t-t_o)}\,[x]_{(t_o)} + \int_{t_o}^{t} [\Phi]_{(t-\tau)}\,[B]\,\{u\}_{(\tau)} d\tau \tag{14}$$

A representação em tempo discreto da Eq. 14, assumindo o interesse apenas nos instantes de tempo $T_k = k\,T$ de período $T = t - t_o$ igualmente espaçado com excitação constante, terá a forma:

$$\{x\}_{(t_{k+1})} = [\Phi]_{(T)}\{x\}_{(t_k)} + [H]_{(T)}\{u\}_{(t_k)} \tag{15}$$

para to = 0 tem-se : $[\Phi]_{(T)} = e^{[A]T}$ e $[H]_{(T)} = \int_0^T e^{[A]\tau} d\tau\,[B] = [A]^{-1}([\Phi]_{(T)} - [I])[B]$

resultando na expressão final completa na forma matricial utilizada para o cálculo do vetor de estado no instante t_{k+1} a partir do estado do instante t_k com a matriz dinâmica do sistema **[A]**, matriz de transição $[\Phi]$ e matriz **[B]** de combinação de aplicação do forçamento externo **{u}** (conforme proposto em Ogata, 1993):

$$\{x\}_{(t_{k+1})} = [\Phi]_{(T)}\{x\}_{(t_k)} + [A]^{-1}([\Phi]_T - [I])[B]\{u\}_{(t_k)} \qquad (16)$$

Análise das Propriedades do Sistema

O cálculo das autopropriedades da matriz dinâmica **[A]** do sistema, de ordem 2n, permite obter as características naturais e modos de vibrar do sistema parametrizado em função da velocidade **Vo**.

Observa-se na Fig. 3a os autovalores do primeiro modo, pares complexos conjugados, apresentados no plano complexo para diferentes valores de velocidade. Este modo corresponde ao movimento de passeio lateral do rodeiro conhecido como ***Lacet*** ou ***Hunting*** (ver Fig. 4a).

A freqüência natural deste modo é linearmente proporcional à velocidade, conforme apresentado na Fig 5a, o que corresponde a um comprimento de onda de movimento lateral δ_L aproximadamente constante (Fig. 6b - 11,5 metros para este caso). O fator de amortecimento ζ possui valores em torno de 0,24 atenuando-se com o aumento da velocidade. A 60 m/s o autovalor apresenta parte real positiva (fator de amortecimento menor que zero) caracterizando a velocidade crítica acima da qual o sistema torna-se instável, conforme apresentado nas Figs. 3a e 5b.

Inspecionando os autovetores deste modo, observa-se que possuem valores complexos, o que representa movimentos relativos com ângulo de fase. O atraso do ângulo de yaw (φ_z)em relação ao movimento lateral na direção lateral y (u_y) é de aproximadamente $\pi/2$ (Tabela I - 104,19° e Fig. 6a). Portanto, quando o movimento lateral é máximo, o ângulo de yaw é próximo de zero (ver Fig. 4).

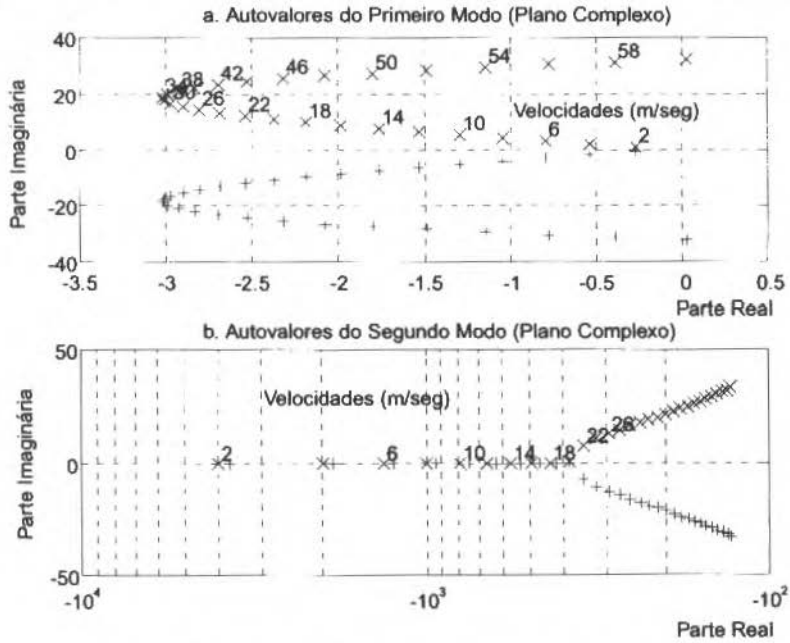

Fig. 3 Autovalores do Primeiro (x,+) e Segundo Modos (x, +)

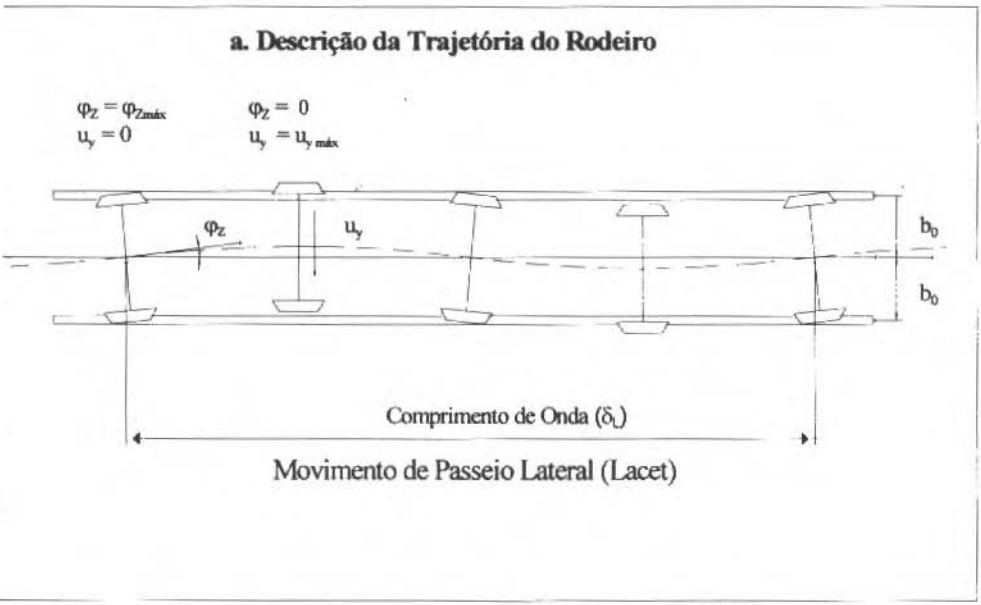

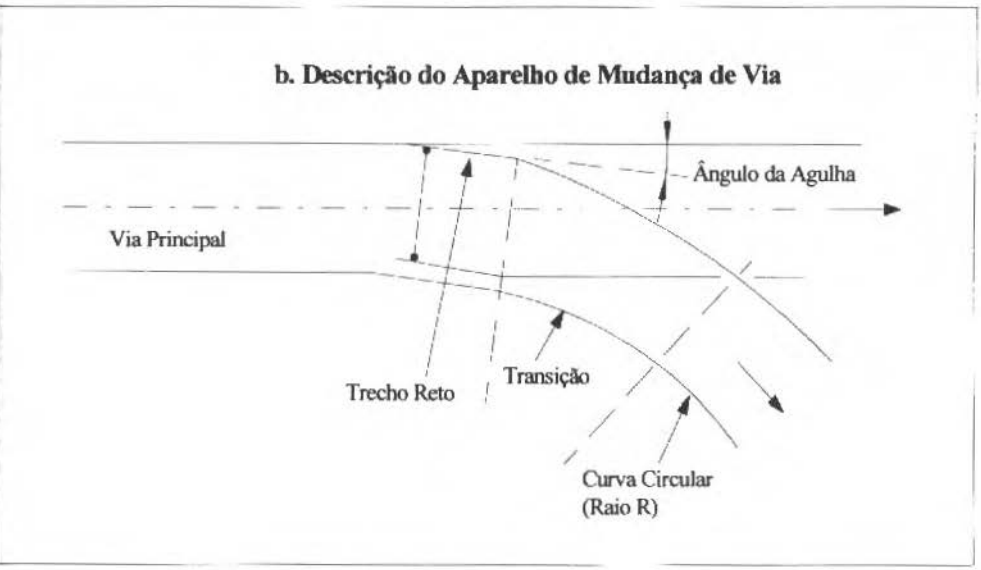

Fig. 4 Descrição da Trajetória do Rodeiro e do Aparelho de Mudança de Via

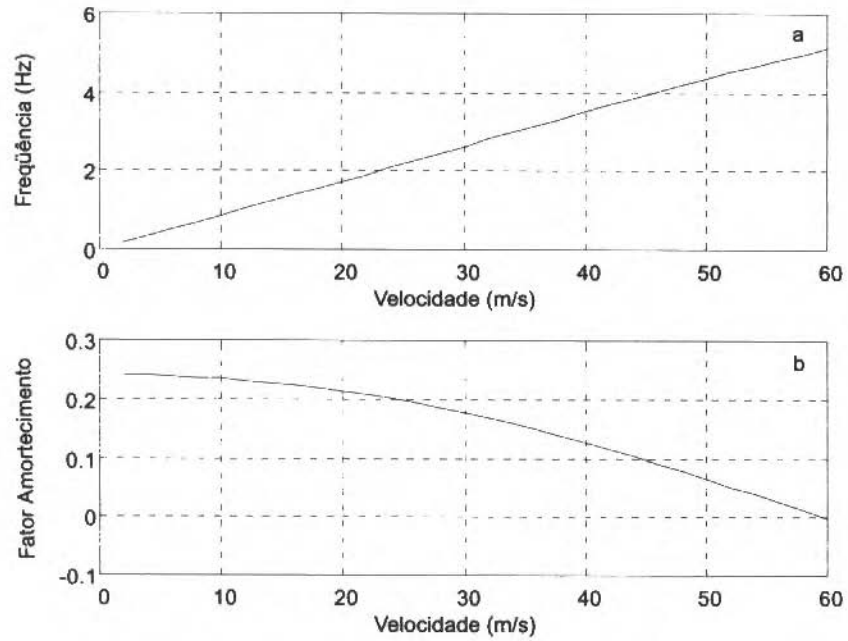

Fig. 5 Propriedades do Primeiro Modo: Frequência Natural e Fator de Amortecimento

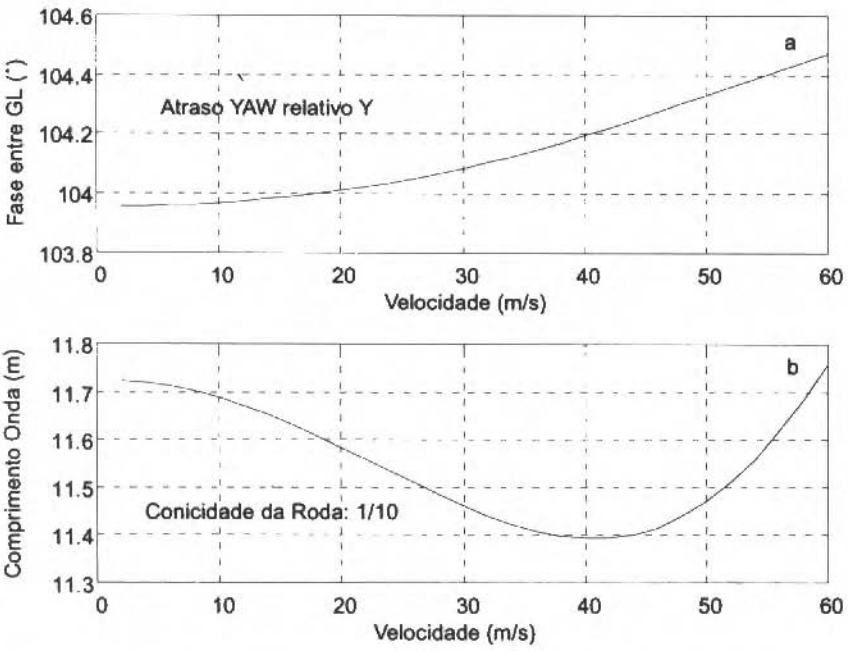

Fig. 6 Características do Primeiro Modo: Ângulo de Fase do Primeiro Modo e Comprimento de Onda do Movimento Lateral

Tabela 1 Autovetores dos Modos para Velocidade de 40 m/s

Coordenadas	Autovetor 1º Modo	Autovetor 2º Modo
Deslocamento Lateral (u_y)	-0,0174 + i 0,0353	-0,0045 + i 0,0002
Ângulo de yam (φ_z)	+ 0,0212 + i 0,0045	-0,0003 + i 0,0027
Ângulo de Fase	104,19º	93,42º

O segundo modo possui um par de autovalores reais distintos (sistema sobreamortecido) até 20 m/s conforme apresentado na Fig. 3b. A partir desta velocidade os autovalores passam a ter parte imaginária diferente de zero, formando um par complexo conjugado subamortecido (Fig. 3b). Em baixas velocidades, o módulo dos autovalores reais (correspondente a constantes de tempo) são inversamente proporcionais à velocidade (Fig. 7a). A partir de 20 m/s a freqüência natural amortecida cresce rapidamente para valores idênticos ao primeiro modo (Fig. 7b). O fator de amortecimento deste modo é elevado chegando a 0,97 para velocidade de 60 m/s (Fig. 8a). O ângulo de fase observado na Fig. 8b, cresce rapidamente com a velocidade, sendo 93,42° para velocidade de 40 m/s (Tabela 1)

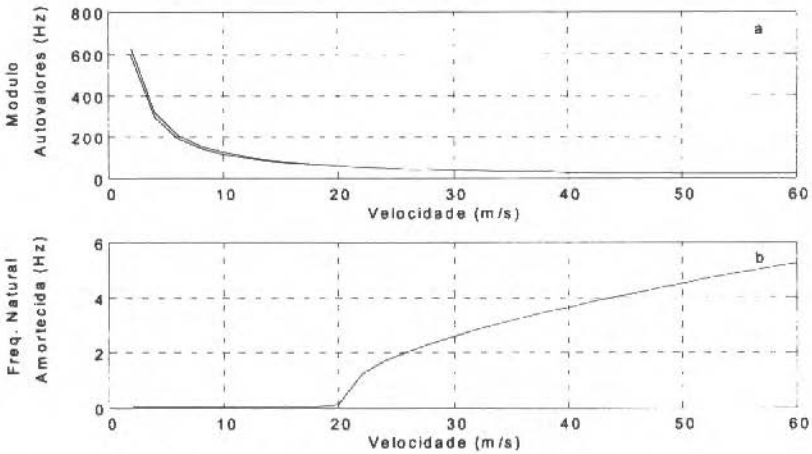

Fig. 7 Propriedades do Segundo Modo: Módulo dos Autovalores Freqüência Natural Amortecida

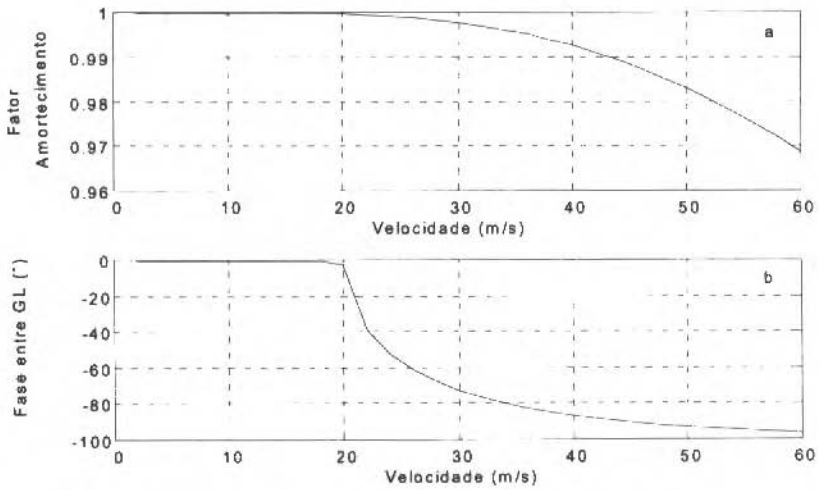

Fig. 8 Caracteristicas do Segundo Modo: Fator de Amortecimento do Segundo Modo Ângulo de Fase entre os Graus de Liberdade

Avaliação da Sensibilidade

A Equação 7 foi parametrizada em $\mathbf{V}_o$ onde foram analisadas as autopropriedades. Entretanto outros parâmetros possuem variações, inclusive não lineares, do sistema mecânico real. Observando o perfil da roda constata-se que a conicidade varia bastante próximo da região do friso. Adicionalmente a rigidez das forças de contato roda/trilho é influenciada, entre outros fatores, pelas proporções da elipse de contato (a/b). Torna-se conveniente o conhecimento das tendências das autopropriedades devido a variação destes valores.

Para um determinada velocidade constata-se, por inspeção da matriz dinâmica do sistema [**A**], que para o primeiro modo, devido ao aumento da conicidade da roda λ ou aumento da rigidez do contato (k_x e k_y):

- Freqüência natural deste modo aumenta;
- Velocidade crítica diminui;
- Fator de amortecimento diminui e
- Comprimento de onda diminui.

O comprimento de onda não se altera com a variação da rigidez. Entretanto, o módulo da raiz do segundo modo aumentou bastante especialmente em baixas velocidades (diminuiu a constante de tempo). A conicidade afeta pouco as características do segundo modo.

Simulação

A partir do modelo construído é possível simular, utilizando algoritmo apropriado (Barbosa, 1993), o comportamento do rodeiro na inscrição de uma curva ou em um aparelho de mudanças de via (AMV) com variação da trajetória da via. Esta é a situação onde se encontra maior adversidade para inscrição do rodeiro e local de elevada incidência de acidentes.

Um AMV é constituído basicamente por três elementos primários de geometria: trechos de reta, curva de transição e curva circular. Ao inscrever o AMV o rodeiro se depara inicialmente com uma mudança angular repentina da direção da via (ângulo de kick). Este trecho corresponde à agulha, que nos modelos mais simples de AMV é um segmento reto de trilho que desloca a direção da via lateralmente iniciando o desvio. Após este trecho inicia-se a curva de transição com variação linear de curvatura (clotóide - ver Fig. 2), variando de zero a 1/R e, finalmente, o trecho em curva circular de raio R. A Figura 4b apresenta de forma esquemática os elementos do AMV.

Uma aproximação simplificada da entrada da agulha do AMV (trecho reto com ângulo α de kick) pode ser feita por um pequeno trecho de grande curvatura, resultando num pulso de curvatura de valor $R = Vo\ \Delta t / \alpha$ (onde Δt = intervalo de cálculo).

O resultado da simulação do comportamento do rodeiro entrando em um AMV pode ser visualizado na Fig. 9. São apresentados o deslocamento lateral do rodeiro em relação ao centro da via (**Y**) e o ângulo de ataque do rodeiro em relação à direção da via (ângulo de yaw).

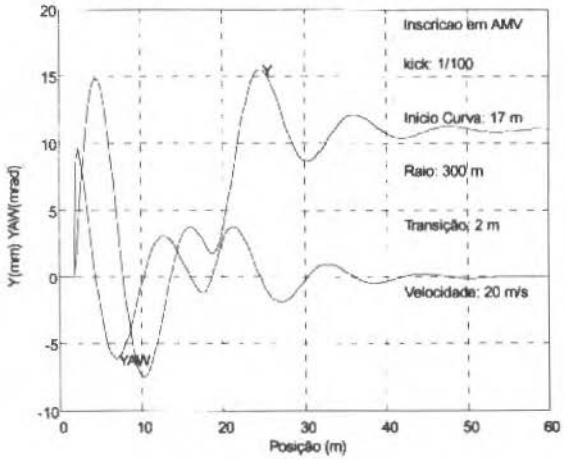

Fig. 9 Resultados da Simulação da Dinâmica do Rodeiro

Observa-se durante o início da inscrição do AMV (localizado à 2 metros da posição inicial) a mudança repentina do ângulo de ataque devido a agulha e do deslocamento lateral. Em seguida o rodeiro reverte o deslocamento lateral buscando a centralização, atingindo deslocamento lateral de 14,8 mm no trecho reto da agulha a 4,5 metros do início da simulação.

A partir de 17 metros inicia-se a curva de transição de 2 metros em seguida a curva circular. O valor máximo de 15,5 mm de deslocamento lateral ocorre na posição de 24,7 metros, estabilizando posteriormente a oscilação em torno do valor de equilíbrio de 10,95 mm de deslocamento lateral na curva circular de 300 metros de raio.

Conclusões

Foram apresentados os elementos mecânicos para elaboração do modelo linear do rodeiro ferroviário. As forças no contato roda/trilho, fundamentais para a representatividade do sistema, foram modeladas e incluídas nas equações. As autopropriedades do sistema parametrizado em função da velocidade V_0 foram calculadas e analisadas.

O primeiro modo de movimento com freqüência baixa corresponde ao passeio lateral do rodeiro em relação à via. Este modo possui comprimento de onda de movimento no espaço aproximadamente constante para a faixa de velocidades investigada, sendo fortemente influenciado pela conicidade λ da pista de rolamento da roda. O amortecimento modal apresenta valores decrescentes em função da velocidade, tornando-se menor que zero para velocidades acima de 60 m/s, o que corresponde a um sistema instável, definindo-se uma velocidade crítica.

O segundo modo, sobreamortecido, apresenta raízes reais distintas com módulo inversamente proporcional à velocidade e fortemente dependente da rigidez k_x e k_y do contato. A partir de 20 m/s as raízes tornam-se complexas conjugadas (subamortecido) e com valor de freqüência natural amortecida que se aproxima do primeiro modo em alta velocidade (Figs. 5a e 7b).

A simulação da inscrição do rodeiro em via com trajetória variável, permite observar o comportamento dinâmico do rodeiro. O cálculo dos movimentos permite identificar os locais de maior deslocamento lateral e ângulos máximos. Apesar de simplificado, este modelo permite visualizar o comportamento rodeiro na sua interação com a via para percurso com trajetórias variáveis como é o caso de AMV's. Desta forma é possível investigar o comportamento dinâmico do rodeiro em vias curvas gerando subsídio para analise, concepção e projeto de AMV's.

A análise do sistema linear permite identificar o substrato das características do sistema dinâmico como preparação para implementação do modelo tridimensional completo não linear utilizando a técnica e programas de Sistemas Multicorpos (MBS).

Dados do Sistema

Conicidade da Roda	$\lambda = 0{,}10$
Raio Nominal da Roda (36")	$r_o = 0{,}4572$ m
SemiLarg. Rodeiro (bitola via)	$b_o = 0{,}7175$ m
Semidistância da Susp. Primária	$e_o = 0{,}61$ m
Massa do Rodeiro	$m = 1751$ kg
Momento de Inércia do Rodeiro	$\Theta = 800$ kg m^2
Rigidez Lat. Susp. Primária	$cy = 1{,}00 \times 10^2$ N/m
Rigidez Long. Contato	$kx = 6{,}20 \times 10^6$ N
Rigidez Lat. Contato	$ky = 6{,}50 \times 10^6$ N
Rigidez Torc. Susp Prim.	$kzz = 1{,}70 \times 10^6$ N m/rad.
Rigidez Long. Susp. Primaria	$cx = 4{,}5687 \times 10^6$ N/m

Referências

Barbosa, R. S., Setembro, 1993, "Estudo da Dinâmica Longitudinal do Trem", Dissertação de Mestrado, Universidade Estadual de Campinas (Unicamp), Campinas, São Paulo, Brasil.

Costa, A., 1994, "Application of Multibody Systems (MBS) Techniques to Vehicle Modelling" S.A.E. São Paulo.

Costa, A., Barbosa R. S., Weber, H. I. e Pascal J. P., Junho 1994, "Um Programa Modular de Sistemas Multicorpos (MBS) para a Simulação de Veículos e Composições Ferroviárias", Seminário Franco Brasileiro de Transportes Públicos, São Paulo.

Gasch, R. e Knothe, K. , 1987, "Strukturdynamik Diskrete Systeme", Springer-Verlag, Vol. 1.

Ogata, K., 1993, "Discrete-Time Systems", Prentice-Hall, 2ª Ed.

RBCM - J. of the Braz. Soc. Mechanical Sciences
Vol. XVIII - No.4 - 1996 - pp. 330-337

ISSN 0100-7386
Printed in Brazil

Cogeneration System Design Optimization

José Antônio Perrella Balestieri
UNESP - Universidade Estadual Paulista
Faculdade de Engenharia de Guaratinguetá
Departamento de Energia
12500-000 Guaratinguetá, SP Brasil

Paulo de Barros Correia
UNICAMP - Universidade Estadual de Campinas
Faculdade de Engenharia Mecânica
Departamento de Energia
13083-970 Campinas, SP Brasil

Abstract

Cogeneration system design deals with several parameters in the synthesis phase, where not only a thermal cycle must be indicated but the general arrangement, type, capacity and number of machines need to be defined. This problem is not trivial because many parameters are considered as goals in the project.
An optimization technique that considers costs and revenues, reliability, pollutant emissions and exergetic efficiency as goals to be reached in the synthesis phase of a cogeneration system design process is presented. A discussion of appropriated values and the results for a pulp and paper plant integration to a cogeneration system are shown in order to illustrate the proposed methodology.
Keywords: Cogeneration, Optimization, Multiple Programming, Design, Efficient Solutions.

Introduction

Design can be defined as any activity developed in a synthesis phase, where a new or a modified concept is created to satisfy certain demands, and in an analysis phase, that involves testing the concepts proposed in the previous step in its capacity to satisfy such demands.

Cogeneration system planning and design can be developed according to analytical or optimization models that will permit the definition of the equipment and operational procedures.

Some important questions must be answered in the cogeneration system planning:

- How is the thermal cycle to be adopted?
- Which equipment must be chosen?
- How many units of each equipment is indicated?
- How is the individual capacity of each equipment?
- Which enthalpy level drop must be explored?

Both analytical and optimization models can be used to generate different technical solutions to a specific case-study; all the proposed solutions can be grouped on a rectangle, as proposed by Bohem, 1987, and represented in Fig. 1.

Nomenclatura

ECO_2 = emission factor of CO_2, kg CO_2/kg fuel
ESO_2 = emission factor of SO_2, kg SO_2/kg fuel
ENOx = emission factor of NOx, kg Nox/kg fuel
F = capital recovery factor, year^{-1}
M = operating/maintenance costs
FIX = equipment capital cost. 10^6 US$
S = feasible region of a problem
m = flow rate. 10^6 kg/year
P[i] = power generated, MW
nK = number of arcs in a network
pe = earning for selling electricity, US$/kg steam
pu = fuel costs, US$/kg fuel
rhs = steam demand in the process, 10^6 kg/year
χ = exergetic loss factor, $\chi_i = 1 - T_0(\Delta s/\Delta h)$
Δh = enthalpy drop, kJ/kg
ST = steam turbine
GT = gas turbine
HRSG = heat recovery steam generator

Presented at the 1995 ASME International Mechanical Engineering Congress and Exposition - San Francisco, CA, November 12-17, 1995. ASME permission to reprint the paper is acknowledged. Associate Technical Editor: Carlos Alberto Carrasco Altemani.

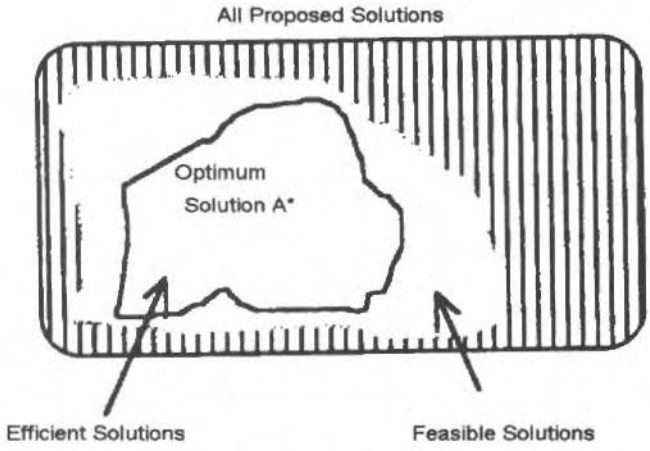

Fig. 1 Solutions Space (Boehm, 1987)

Feasible solutions are those that satisfy all constrains of a problem, considering that it can be formulated as a set of criteria to be reached subject to some constraints.

When an optimization problem has only one objective to be reached, the solution obtained will be an optimum point; if the model is used to generate maximum and/or minimum solutions according to multiple criteria, each one will be an optimum solution for the respective criterion and they can be grouped on an efficient set of solutions ,each one related to this individual goal.

From an economic point of view, it is intended to synthesize a cogeneration system that reaches minimum operating and capital costs with maximum production of electrical surplus to be sent to the grid; point A can represent this special solution, that is an optimum point.

Cogeneration plant reliability can be another important criterion to be considered; these systems must be planned to operate on a continuous condition or at design point for many hours during the year (more than 6500 hours/year) and must have redundant equipment to warrant the continuity of electrical supply even in the case of a fault of some generators.

Environmental regulations are another important criterion to be considered in a cogeneration system planning. CO_2, SO_2 and NOx emission levels are becoming more and more restrictive, conducting the optimization problem to several solutions, perhaps different to the previous ones.

The fact of choosing one single criterion in the design of a cogeneration system will imply in a project that reaches the maximum (or minimum) for that goal but with unsatisfactory (or perhaps not acceptable) results to all the others. A trade-off methodology must be defined for helping in the decision-making process.

Multiobjective Condition of Design

The planning of a cogeneration system can be developed by means of a simulation process (varying thermodynamic conditions of a proposed plant)) with satisfactory results. However, in the case of designing new plants, this tool can only be used after the choosing process of a cycle and the definition of a certain scheme.

Optimization models can be used successfully in the design and operation of cogeneration plants. Operational analysis is usually done by formulating linear (Balestieri and Correia, 1994).

Cogeneration system operation optimization models generally consider as objective function an economical expression of net benefit that maximizes the revenues from electricity and minimizes investment and operational costs (Ehmke, 1990; Nath et al., 1989; Puttgen and Macgregor, 1989).

Suppose that point B of Fig. 2 represents the optimum value for net benefit in the feasible region S: this solution maximizes the vector **b** that represents this objective function.

Considering the same constraints but using now as objective function an expression related to the cogeneration system electrical reliability, it is expected that a new solution, represented by R, will be generated and will be certainly different to the other; vector **r** indicates the preferential direction of reliability function.

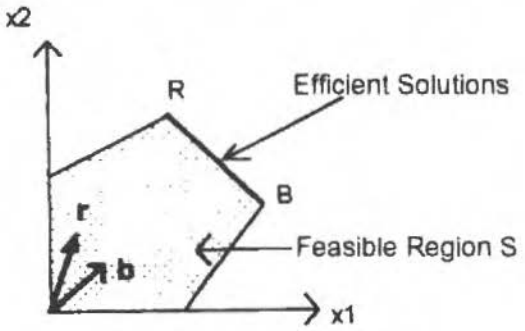

Fig. 2 Feasible Region in the Decision Space

Schemes (R) and (B) of Fig. 3 are the corresponding schemes (physical solution) of optimum values reached by net benefit vector b and reliability vector r.

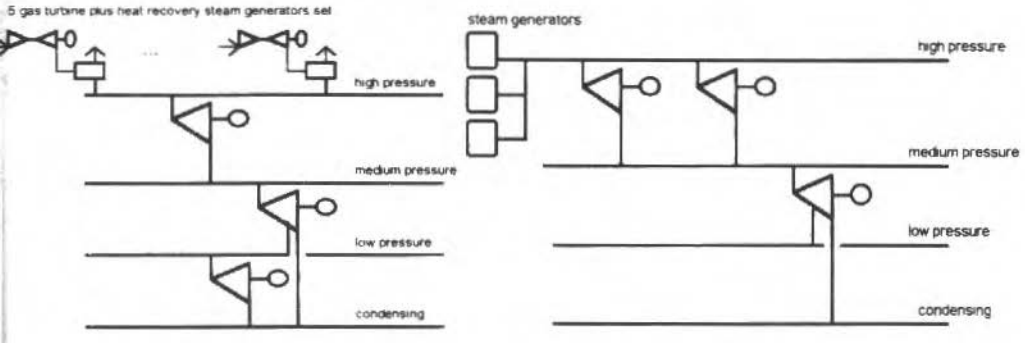

(R) Maximum Reliability Scheme (B) Maximum Net Benefit Scheme

Fig. 3 Optimum Proposed Schemes

In the feasible region S it can be seen that only solutions placed on RB segment have a relationship of gain and loss between reliability and net benefit: coming through RB segment from B to R reliability is decreasing but net benefit is increasing and vice-versa.

All solutions in RB segment are named efficient, non-dominated or Pareto's optimum and, from an efficient point, it is not possible to move feasibly to another in order to increase one of the objectives without necessarily decreasing at least one of the others.

In cogeneration system planning several objectives are considered subject to the same constraints and it is difficult to represent such variables as a surface, so a mathematical tool must be proposed to help decision-makers define the best scheme to a case-study by adequately weighting the goals according to his preference structure.

A multiobjective interactive model that helps to define thermal cycles in this first-step and the size, capacity and type of each equipment in its second-step is presented in the next section.

Multiobjective Approach

A multiobjective interactive programming model that considers in each iteration the decision-maker's preference structure for a set of objective functions was indicated to generate efficient solutions used in the evaluation of a specific case-study.

Interactive procedures generally conduct an exploration over the region of feasible alternatives for a satisfactory efficient solution. There are alternative steps where the computer leads to a solution in one phase, so the decision-maker inputs information and intervenes in the proposed solution in the other phase. This interaction between man and model enables the decision-maker to learn more about his problem and to have more insight to decide.

A two-step multiobjective model (TSMM) was formulated to permit a faster and more efficient search for solutions; initial phase defines the thermal cycle to be adopted, considering steam, gas and combined cycle as possible options. This step reduces the original problem by discarding the worst options.

Final phase uses this information to define, after proposing several solutions, the chosen scheme, type, capacity and quantity of each equipment as well as general techniques and economic data relevant to the cogeneration system planning - cost, reliability, pollutant emission levels, installed power, etc. (Balestieri, 1994).

A mathematical structure of a generalized network was indicated to solve the linear programming problem because of its advantage over the conventional Simplex method - computational efforts are reduced by about 50 times (Glover et al., 1978). Another important reason is that the network, defined in terms of nodes and arcs, can be well represented in those latter mathematical entities. Equipment's energy conversion efficiencies can be associated to the gain variable of each arc and this can mathematically express the physical phenomenon of converting certain flow rate of exhaust gases from a gas turbine in a fewer flow rate of steam in the heat recovery boiler.

The Geoffrion, Dyer and Feinberg procedure (Steuer, 1986) was chosen to be part of the search algorithm since it is compatible with network structure and don't impose new constraints to the original problem; optimal solution for each objective is provided according to the same set of constraint equations and net benefit optimal solution is taken to the position of the problem's initial solution.

The model presents a new solution an four intermediate solutions are generated by means of pairwise comparison questions. Decision-maker is then invited to express his preference by choosing a solution and deciding about re-start or finish iteration (Fig. 4).

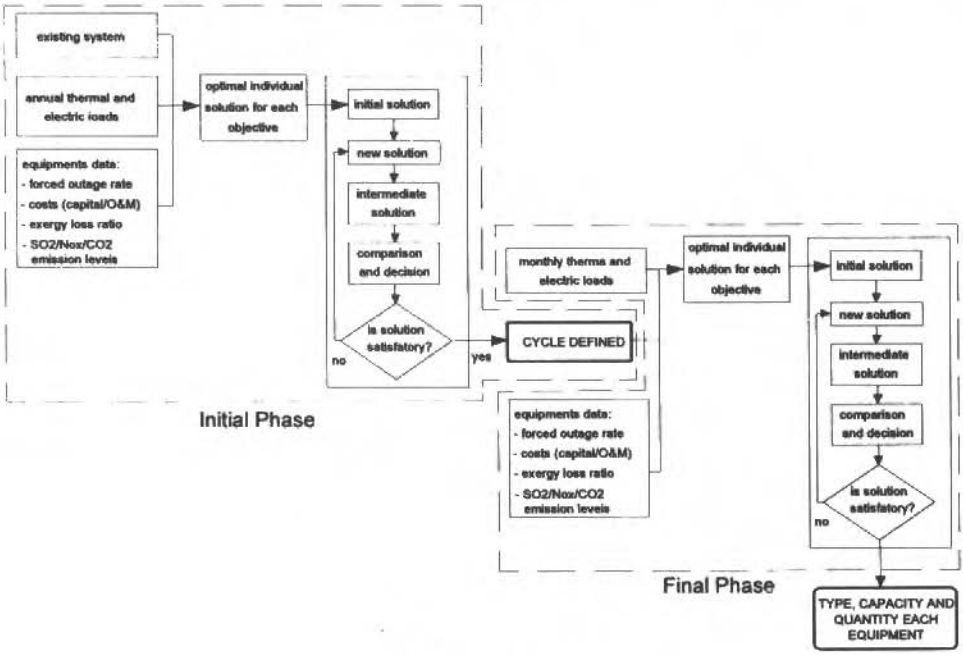

Fig. 4 TSMM Algorithm

Mathematical Modeling

The following mathematical functions describe the set of objective functions and constraints for the cogeneration system planning:

$$\text{Min} \sum_{i=1}^{nk} (x_i, \Delta H_i)\, m_i \tag{1}$$

$$\text{Min} \sum_{i=1}^{2,46} ECO_{2,i} m_i \tag{2}$$

$$\text{Min} \sum_{i=1}^{2,46} ESO_{2,i} m_i \tag{3}$$

$$\text{Min} \sum_{i=1}^{2,46} ENOx_i m_i \tag{4}$$

$$\text{Max} \sum_{i=1}^{nk} m_i \tag{5}$$

$$\text{Max} \sum_{i=1}^{nk} (pe_i m_i) - \sum_{i=3}^{5} (pu_i m_i) - \sum (FIX/F) - M \tag{6}$$

subject to: $\mathbf{m_i} \in S$

Objective function (1) aims to lead the solution to the scheme that has the machines with the least thermodynamic losses (measured according to the exergy loss factor χ_i) and, therefore, it is an energy conservation criterion.

Functions (2), (3) and (4) conduct the solution to a CO_2, SO_2 and NOx less pollutant schemes, respectively, reflecting the environmental question of the 1990's. Objective function (5) is related to the plant reliability and is stated considering that a scheme will be as highly reliable as the most electric generation machines are available in the cogeneration system (Sullivan, 1977). It is still an important way to calculate the LOLP (Loss of Load Probability) according to a recursive equation.

Objective function (6) express the net benefit obtained with the congeneration system operation; it has first term that aims of maximizing the revenues from electricity according to a certain buyback rate proposed to the model within the minimization of fuel consumption, capital and operational & maintenance costs on the other terms.

Problem constraints $\mathbf{m_i} \in S$ were stated considering that mass must be conserved in all nodes and that medium and low pressure process must be satisfied in its steam requirements all the time (thermal parity). In this study we considered that another alternative could be formulated, such as the electric parity.

A General Design Module (GDM) is represented in Fig. 5 for the final phase of TSMM; it contains all possible alternatives to be chosen as optimum schemes to every objective function and yet to every efficient solution proposed by TSMM (number 3 to 8 are convention steam generators, 9 to 13 are gas turbine coupled to heat recovery steam generators and 14 to 22 are back-pressure or condensing steam turbines, with or without extraction).

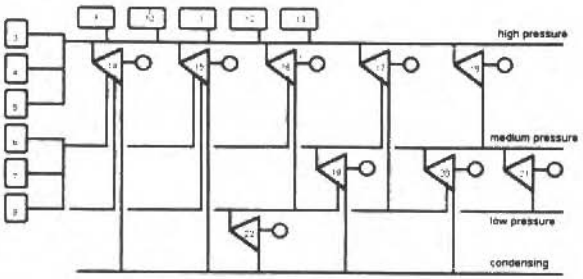

Fig. 5 General Design Module

Case-Study

A pulp and paper industry has an annual demand of medium pressure steam (1.3 MPa/275°C) of $1263x10^6$ kg/year and of low pressure steam (0.3 Mpa/170°C) of $1230x10^6$ kg/year supplied by a generation system that has pressure steam generators (4.0 MPa/350°C) burning fuel oil and a by a condensing turbine with two extractions. This unit is at the moment generating electricity with a little deficit that is supplied by the grid.

An analysis of process conditions showed that it is possible to condense $2500x10^6$ kg/year ; considering that it is necessary to have an installed capacity of 36 MW to satisfy the electrical needs of the process. TSMM is started by defining the optimal solution for each objective function individually. Table 1 presents information used to simulate TSMM

Table 1 General Assumptions for the Case-Study (Balestieri, 1984)

Emission Levels (kg pollutant/kg fuel)

Fuel	CO_2	SO_2	NOx
oil	3.156	0.018	0.00728
gas	2.683	0.001	0.00681
biomass	1.380	0.068	0.00010

Annualized Capital Costs of Energy Generation Systems

Equipment	Fixed Cost (10³ US$/year)	Variable Cost (US$/kg)
GT-HRSG	0.780	0.0002364
HP-boiler	0.232	0.0005857
Backpressure ST	0.185	0.0004186
Condensing ST	0.670	0.0034740

Based on these results, several alternative solutions can be proposed in the TSMM initial phase; in this step it was concluded that whichever alternative routes were possible to conduct mass flow except the expansion from medium and low pressure to condensing unit.

TSMM final phase was conducted according to these conditions for two different values of buyback rate. Figure 6 presents the scheme obtained via simulation by the TSMM model for a 35 US$/MWh buyback rate (table 2 presents technical and economical general data related to this scheme). The analysis of such scheme reveals that it is recommended, in this case, the medium pressure steam generation by black liquor burning and the use of steam turbines from high to medium pressure level and from medium pressure to condensing line.

In the second simulation exercise, a buyback rate of 95 US$/MWh indicated a new scheme with a high incentive to the power generation in a combined cycle, no more black liquor burning is recommended, so the disposal of this byproduct in the agricultural sector must be considered, as well as its use as an alternative fuel in the high pressure steam generations or in the gas turbine cycle by gasification process (Fig. 7 and Table 3).

In both analysis the decision-maker was expected to generate a solution that could satisfy steam needs of medium and low pressure process with a Loss of Load Probability of around 30% (that is equivalent to about 6000 hours/year of continuous operation, that is a reasonable value for this technology, according to Stambler, 1989) and the lowest payback as possible.

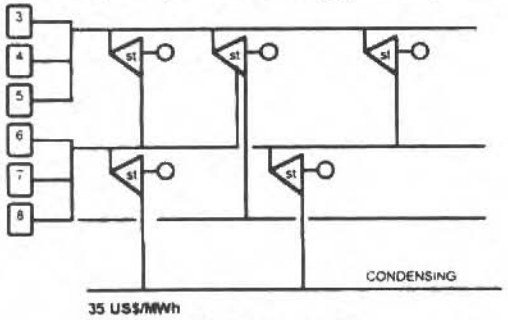

Fig. 6 Scheme 1

Table 2 Data of Scheme 1

Installed capacity	= 162.39	[MW]
Electric demand	= 36.00	[MW]
Electric surplus	= 126.39	[MW]
LOLP	= 2945.27	[h/year] = 33.62%
Power generated in each turbine:		
P[18]	= 5.52	[MW]
P[32]	= 5.32	[MW]
P[33]	= 3.56	[MW]
P[35]	= 8.56	[MW]
P[38]	= 93.59	[MW]
P[39]	= 1.82	[MW]
P[40]	=44.04	[MW]
CO_2 emission	= 1195.33	[kgCO_2/MWh]
SO_2 emission	= 0.57	[kgSO_2/MWh]
NOx emission	= 2.29	[kgNOx/MWh]
Capital costs	= 141.70	[10^6 US$]
Payback	= 1.55	[years]
Net benefit	= 91.42	[10^6 US$/year]

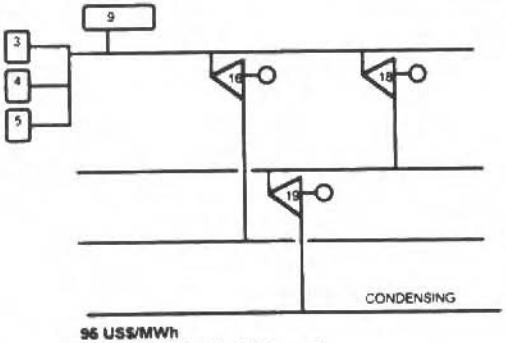

Fig. 7 Scheme 2

Table 3 Data of Scheme 2

Installed capacity	= 166.65	[MW]
Electric demand	= 36.00	[MW]
Electric surplus	= 130.65	[MW]
LOLP	= 2761.00	[h/year] = 31.52%
Power generated in each turbine:		
P[18]	= 18.80	[MW]
P[32]	= 10.22	[MW]
P[38]	= 137.63	[MW]
CO_2 emission	= 561.05	[kgCO_2/MWh]
SO_2 emission	= 0.65	[kgSO_2/MWh]
NOx emission	= 2.61	[kgNOx/MWh]
Capital costs	= 131.79	[10^6 US$]
Payback	= 0.60	[years]
Net benefit	= 246.73	[10^6 US$/year]

Conclusions

TSMM has been specially developed to help designers and decision-makers in the pre-feasibility and planning of a cogeneration system; its most relevant contribution is the wide range of solutions generated in a short time interval and the possibility of interacting with the model at any time to alter the preference structure designation of objective functions.

The use of generalized networks affords low computation times and a high accuracy of results. A multiobjective interactive structure leads to a conversational tool for defining several parameters of a cogeneration system design.

Some improvements in the auxiliary procedures must be done in the proposed model;; the cost functions developed to the thermal and electrical equipment are not well suiting the real values and must be reviewed. This fact is responsible for the high specific price (868 and 790 US$/kW, respectively, for the proposed schemes in Fig. 6 and 7), that is expected to be around 650 US$/kW for units higher than 150 MW.

References

Ahuja, R.K. et al., 1993, "Network flows", Prentice Hall, N. Jersey (USA).

Balestieri, J.A.P., 1994, "Planning Cogeneration Systems: a Multiobjective Approach" (in Portuguese), Ph.D. Thesis, State University of Campinas (UNICAMP), Campinas, SP, Brazil.

Balestieri, J.A.P. and Correia, P.B., 1994, "Planning Cogeneration Systems: a Multiobjective Expansion Analysis", Florence World Energy Research Symposium (FLOWERS), Proceedings, Florence, Italy, pp, 1025 - 1032.

Boehm, R.F., 1987, "Design Analysis of Thermal Systems", John Wiley, N.Y, USA.

Correia, P.B., 1989, "A Sectorial Model for Energy Supply Optimization" (in Portuguese). Ph. D. Thesis, State University of Campinas (UNICAMP), Campinas, SP, Brazil.

Ehmke, H.J., 1990, "Size Optimization for Cogeneration Units". Energy, Vol. 15, pp. 35-44.

Glover, F. et al., 1978, "Generalized Network: a Fundamental Computer-based Planning Tool". Manag. Sci., Vol. 24, pp. 1209-20.

Nath, R. et al., 1986, "Joint Optimization of Process Units and Utility System". Chem. Eng. Progress. Vol. 82, pp. 31-38.

Puttgen, H.B., MacGregor, P.R., 1989. "Optimum Scheduling Procedure for Cogeneration Small Power Producing facilities". IEEE Trans. PAS, Vol. 4, pp. 957-963.

Steuer, RF., 1996, "Multiple Criteria Optimization", John Wiley, Singapore.

Sullivan, R.L. 1977, "Power System Planning", McGraw-Hill, N.Y., USA.

Stambler, I., 1989, "EPRI Seeks Dramatic Gains in Maintenability and Reliability." Gas Turb. World, Vol. 19, pp. 15-20.

RBCM - J. of the Braz. Soc. Mechanical Sciences
Vol. XVIII - No.4 - 1996 - pp. 338-354

ISSN 0100-7386
Printed in Brazil

Recent Advances and Application of Turbulence Depth-Integrated Two-Equation Closure for Modeling Contaminant Discharges

Liren Yu
Antonio Marozzi Righeto
Universidade de São Paulo
Escola de Engenharia de São Carlos
Departamento de Engenharia Hidráulica e Sanitária C.P. 359
13560-970 São Carlos, SP Brasil

Abstract

This paper presents a brief review and up-to-date development of the depth-integrated turbulence two-equation closure, to be specific, the depth-integrated $\tilde{k} - \tilde{\varepsilon}$ model and $\tilde{k} - \tilde{w}$ model. A numerical simulation of the side discharge of waste heat into natural waters has been taken as an example of the practical application of the $\tilde{k} - \tilde{w}$ model. In addition, the authors also states the existing problems and further developments of the present depth-integrated turbulence two-equation models. The main objective of the paper is to integrate the research on the improvement and development of the present depth-integrated turbulence models with the practice of industrial, environmental and sanitary engineering.
Keywords: Turbulence, Depth-Integrated Two-Equation Closure, Contaminant Discharge Modeling.

Introduction

Almost all flows in natural waters are turbulent. Dealing with turbulent flow and contaminant transport in natural waters is indispensable for scientists and engineers. For example, turbulent transport associated with the discharge of pollutant and (or) waste heat into rivers and coastal regions is of great concern to civil and coastal engineers, and also to environmentalists because of their serious damaging effects on the ecology and ambient. It is very important to be able to correctly simulate and predict the corresponding changes of currents, temperature and concentrations of certain contaminants, as a consequence of the anthropic activity in the area.

Although the significance of timely simulating turbulent flow and contaminant transport within the accuracy of engineering is clear, the numerical simulation and prediction for natural waters is still at an unsophisticated level. This is mainly due to the inherent complexity of the problem. Any successful numerical computation and simulation for modeling flow and transport processes in natural waters depends sensitively upon correctly understanding the mechanics of turbulence and setting up an applicable higher-order turbulence closure model. Up to now two-equation closure models which are characterized by comparative rigorous theoretical fundamentals with reasonable physical background remain the only practicable approach to solve engineering turbulence problems. In order to obtain the necessary information of flow field with less labor in physical experiment, two-dimensional depth-integrated (or so called depth-averaged) mathematical models have been widely adopted in the last two decades. Because the vertical turbulent mixing evens out the vertical non-uniformity within a limited water column rather quickly and thus contaminants are distributed fairly uniformly over a water column, either finite difference methods or finite element methods can successfully simulate and predict flow and contaminant transport in shallow well-mixed flow regions with different time and length scales (Heaps, 1969; Kuipers and Vreugdenhil, 1973; Yu and Zhu, 1993). However, most of these mathematical models used in practical problems merely take the turbulent viscosity and diffusivity as constants or given by simple phenomenological algebraic expressions, which are in a great degree estimated in terms of numerical modeller's experiences. The turbulent viscosity and diffusivity are not fluid properties but really depend on the turbulence structure; they may vary strongly from one point in the flow to another and from one flow situation to another. In well-mixed regions the horizontal distributions of waste heat and contaminants are of great interest so that the depth-integrated turbulence models, especially the advanced two-equation closure models, are found to be accurate enough to satisfy the demands of engineering practice (Rodi et al., 1981). The results

Manuscript received: April 1995. Technical Editor Carlos Alberto Carrasco Altemani

given by the turbulence models, together with the depth-integrated continuity equation, Reynolds equation, and scalar transport equation can provide details for the horizontal velocity components, pressure (water-depth) field, temperature and (or) concentration field, and can also provide the distributions of the corresponding turbulent physical quantities in the domain with engineering scale.

Unfortunately, the 'standard' turbulence two-equation models cannot be applied directly to depth-integrated computation and simulation. The necessary approach is to characterize the local state of turbulence in the sense of depth integration by two turbulence parameters, and to relate the eddy viscosity and diffusivity at each point to these parameters. The landmark of depth-integrated turbulence two-equation closure models is depth-integrated $\bar{k}-\bar{\varepsilon}$ model ($\bar{k}$: depth-integrated turbulent kinetic energy parameter, $\bar{\varepsilon}$: depth integrated dissipation rate parameter of turbulent kinetic energy) established by Rastogi and Rodi (1978), which was stemmed from the 'standard' $k-\varepsilon$ model (k: turbulent kinetic energy, ε : dissipation rate of turbulent kinetic energy, Jones and Lander 1973). In 1988, Yu and Zhang provided another depth-integrated second-order closure model $\bar{k}-\tilde{w}$ ($\tilde{w}$: depth-integrated vorticity fluctuation parameter of turbulence) by adopting the revised version of k-w model (w: time-mean-square vorticity fluctuation of turbulence, see Ilegbusi and Spalding, 1982). The numerical investigation and application of $\bar{k}-\tilde{w}$ model as well as the possible improvement and development of depth-integrated two-equation closure models are presented in this paper.

Nomenclature

B = width of river or channel, jet width, grid point of control volume
b = source term in p´- eq.
C = empirical constants, Chezy coefficient
E = empirical constant
e = empirical constant
G = production of turbulent kinetic energy
g = gravitational acceleration
H = local water depth, jet penetration or eddy height
h = local tranquil water-depth or characteristic water-depth
J = flux
k = turbulent kinetic energy
L = eddy length or turbulence length scale
P = production due to bottom shear or additional source term
p = pressure
Q = flowrate
q = discharged flowrate
S = source term, constant part or coefficient of source term
T = temperature
U = velocity for one-dimensional situation
u = velocity in x- direction
v = velocity in y- direction
w = time-mean-square vorticity fluctuation of turbulence, vorticity fluctuation of turbulent
x = co-ordinate
y = co-ordinate, vertical distance between grid point and wall
Z = elevation
α = water-depth correction coefficient
Γ = turbulent eddy diffusivity
δ = grid span or Kronecker delta
ε = dissipation rate of turbulent kinetic energy
κ = kármán constant
μ = dynamic viscosity
ν = kinematic viscosity
ρ = density
σ = Prandtl number or Schmidt number
τ = shear stress
ϕ = scalar
φ = inclination of river bank
Ω = vorticity of mean movement

Subscripts:

B = submerged outlet
b = bottom or river bed
c = constant
e = jet inlet, east grid point
eff = effective
f = friction
i = eddy, co-ordinate position or index of tenser (i=1, 2, 3)
j = co-ordinate position or index of tensor (j=1, 2, 3)
k = turbulent kinetic energy
kv = additional source term in k-eq. due to effect of vertical velocity gradient
m = momentum, molecular
n = north grid point
p = first grid node near banks, first order term of source term
s = south grid point, water-surface
t = turbulence
w = wall, west grid point, time-mean-square vorticity fluctuation of turbulence
wv = additional source term in w-eq. due to effect of vertical velocity gradients
x = co-ordinate
y = co-ordinate
ε = dissipation rate of turbulent kinetic energy
εv = additional source term in k-eq. due to effect of vertical velocity gradients
ϕ = scalar
μ = dynamic viscosity
0 = inlet of channel or river
* = bottom friction

Superscripts:

* = empirical constant
~ = depth-average defined by eq. (8)
- = depth integration (depth average) defined by eq. (5)
, = correction

Model Formulation

The governing equations for steady and unsteady two-dimensional depth-integrated flows in natural waters can be expressed as

$$\frac{\partial H}{\partial t}+\frac{\partial H\bar{u}}{\partial x}+\frac{\partial H\bar{v}}{\partial y}=0 \tag{1}$$

$$\frac{\partial H\bar{u}}{\partial t}+\frac{\partial H\bar{u}^2}{\partial x}+\frac{\partial H\bar{v}\bar{u}}{\partial y}=-gH\frac{\partial \Delta h}{\partial x}+2\frac{\partial}{\partial x}\left[\frac{\tilde{\nu}_{eff}H}{Re}\frac{\partial \bar{u}}{\partial x}\right]+\frac{\partial}{\partial y}\left[\frac{\tilde{\nu}_{eff}H}{Re}\left(\frac{\partial \bar{u}}{\partial y}+\frac{\partial \bar{v}}{\partial x}\right)\right]$$
$$+\frac{\tau_{sx}}{\rho}-\frac{\tau_{bx}}{\rho}+\bar{S}_{mx}-2\tilde{\nu}_t\frac{\partial u_s}{\partial x}\frac{\partial H}{\partial x}-\tilde{\nu}_t\left(\frac{\partial u_s}{\partial y}+\frac{\partial v_s}{\partial x}\right)\frac{\partial H}{\partial y} \tag{2}$$

$$\frac{\partial H\bar{v}}{\partial t}+\frac{\partial H\bar{u}\bar{v}}{\partial x}+\frac{\partial H\bar{v}^2}{\partial y}=-gH\frac{\partial \Delta h}{\partial y}+2\frac{\partial}{\partial y}\left[\frac{\tilde{\nu}_{eff}H}{Re}\frac{\partial \bar{v}}{\partial y}\right]+\frac{\partial}{\partial x}\left[\frac{\tilde{\nu}_{eff}H}{Re}\left(\frac{\partial \bar{v}}{\partial x}+\frac{\partial \bar{u}}{\partial y}\right)\right]$$
$$+\frac{\tau_{sy}}{\rho}-\frac{\tau_{by}}{\rho}+\bar{S}_{my}-\tilde{\nu}_t\left(\frac{\partial v_s}{\partial x}+\frac{\partial u_s}{\partial y}\right)\frac{\partial H}{\partial x}-2\tilde{\nu}_t\frac{\partial v_s}{\partial y}\frac{\partial H}{\partial y} \tag{3}$$

where Δh stands for the variation of local tranquil water-depth h due to the motion of water, Re and ρrepresents the Reynolds number and density, τ_{sx}, τ_{sy} and τ_{bx}, τ_{by} are the shear stresses on the water-surface and the river bed respectively, $u_s$and $v_s$denotes the surface velocities in the x- and y-directions; $\tilde{\nu}_{eff}=\nu+\tilde{\nu}_t$ is a depth-integrated effective viscosity, with $\tilde{\nu}_t$ being the depth-integrated turbulent kinematic viscosity and ν being the kinematic viscosity of the fluid. Correspondingly, the temperature and concentration of pollutants are governed by the following scalar transport equation:

$$\frac{\partial H\bar{\phi}}{\partial t}+\frac{\partial H\bar{u}\phi}{\partial x}+\frac{\partial H\bar{v}\phi}{\partial y}=\frac{\partial}{\partial x}\left[\left(\frac{\nu}{\sigma_m}+\tilde{\Gamma}_\phi\right)\frac{H}{Re}\frac{\partial \bar{\phi}}{\partial x}\right]+\frac{\partial}{\partial y}\left[\left(\frac{\nu}{\sigma_m}+\tilde{\Gamma}_\phi\right)\frac{H}{Re}\frac{\partial \bar{\phi}}{\partial y}\right]+\bar{S}_\phi \tag{4}$$

where σ_m stands for the molecular Prandtl number for temperature transport or Schmidt number for concentration transport, $\tilde{\Gamma}_\phi$ represents depth-integrated turbulent diffusivity for temperature or concentration respectively. The symbol '-' denotes the depth integrated quantities, by which the depth-integrated velocity components $\bar{u}$, $\bar{v}$in x- and y- directions and the depth-integrated scalar $\bar{\phi}$ in Eqs. (2)-(4) can be defined by the following relations:

$$\bar{u}=\frac{1}{H}\int_{Z_b}^{Z_b+H}u\,dz \qquad \bar{v}=\frac{1}{H}\int_{Z_b}^{Z_b+H}v\,dz \qquad \bar{\phi}=\int_{Z_b}^{Z_b+H}\phi\,dz \tag{5}$$

where Z_b and Z_b+H stand for the bottom elevation and water-surface elevation respectively (see Fig. 1). The depth-averaged turbulent viscosity and diffusivity are not true depth-integrated quantities in the sense of strict mathematical definition by Eq. (5). When $\tilde{\nu}_t$ and $\tilde{\Gamma}_\phi$ are multiplied by the relevant gradient of the transported quantity, the expressions of the depth-integrated turbulence shear tress and mass flux will be satisfied respectively (see Eq. 8). A linearized assumption has been adopted in the numerical process to treat the source terms $\bar{S}_{mx}$, $\bar{S}_{mi}$and $\bar{S}_\phi$ in control volume, produced by submerged discharge:

$$\bar{S}=S_c+S_p\bar{\phi}_p \tag{6}$$

where S_c stands for the constant part of $\bar{S}$, S_p represents the coefficient of the first-order term of $\bar{S}$.

The expressions of $\bar{S}_{mx}$ and $\bar{S}_{my}$ and S_ϕ will be specified in the diffusion simulation section, further on the text.

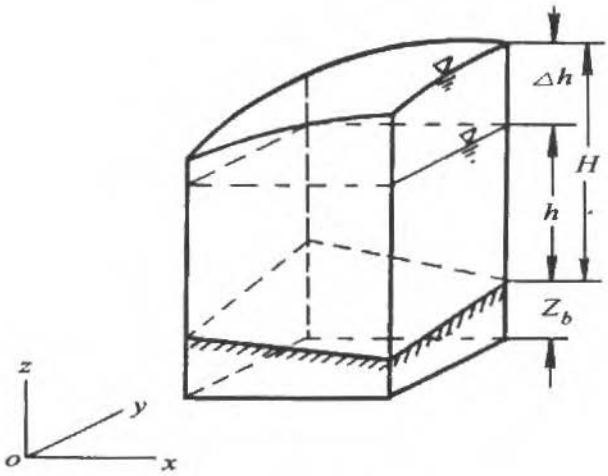

Fig. 1 Ilustration of a Basic Control Volume

Equations (1) to (4) were obtained by simply integrating the fundamental three-dimensional continuity equation and Reynolds equation from the bottom to the water-surface. One should note that the local water-depth H cannot be treated as a constant in the process of integration, since the surface elevation Z_b+H is usually function of the position, for steady flow, and of both the time and the position for unsteady flow (see Fig. 1). The last two terms on the right hand sides of equations (2) and (3) appeared because of the variation of bottom topography and surface elevation, which are referred as a kind of additional source terms produced by Leibniz's integration formula in each vertical water column, and will be analyzed in the Details and Skills of Numerical Computation section, later in the text. The variation of the bottom topography and surface elevation needs to be included in the model and dealt efficiently. This can be achieved by introducing water-depth correction coefficients into the discretized formulas (Yu, 1991). The surface stresses τ_{sx} and τ_{sy} can be determined by empirical expressions in the computational domain; with a spatial scale relatively small, their effect can be neglected. The terms τ_{bx} and τ_{by} stand for the bottom shear stresses in the x- and y- directions, respectively; they are calculated by relating them to the depth-integrated velocity components via

$$\frac{\tau_{bx}}{\rho} = C_f \bar{u}\sqrt{\bar{u}^2 + \bar{v}^2} \quad \text{and} \quad \frac{\tau_{by}}{\rho} = C_f \bar{v}\sqrt{\bar{u}^2 + \bar{v}^2} \tag{7}$$

After determining the depth-averaged turbulent kinematic viscosity $\tilde{\nu}_t$ the equations (1)-(4) form a set of closed partial differential equations that simulate and predict the depth-integrated turbulent flow and the corresponding transport field. In equation (7), C_f is an empirical friction factor which usually is equal to g/C^2 in rivers, where C is Chezy coefficient.

Depth-integrated $\tilde{k} - \tilde{\varepsilon}$ Model

The turbulence two-equation closure model that found widest application and was tested most extensively is the k-ε model, which characterized the local state of turbulence by two parameters: the turbulent kinetic energy k and the rate of its dissipation ε. Since 1978, the model has been developed to describe the depth-integrated open-channel flow (Rastogi and Rodi). In analogy to the original k-ε,

the local depth-integrated state of turbulence was assumed to be characterized by the turbulence energy $\tilde{k}$ and dissipation parameters $\tilde{\varepsilon}$ respectively, and the depth-integrated turbulent stresses $\tau_{i,j}$ and contaminant fluxes $J_{\phi i}$ can then be related to these parameters via

$$\frac{\bar{\tau}_{i,j}}{\rho} = \tilde{\nu}_t\left(\frac{\partial \bar{u}_i}{\partial x_j} + \frac{\partial \bar{u}_j}{\partial x_i}\right) - \frac{2}{3}\tilde{k}\delta_{i,j} \quad \text{and} \quad \frac{\bar{J}_{\phi i}}{\rho} = \tilde{\Gamma}_\phi \frac{\partial \bar{\phi}}{\partial x_i} \tag{8}$$

$$\text{with} \quad \tilde{\nu}_t = C_\mu \frac{\tilde{k}^2}{\tilde{\varepsilon}} \quad \text{and} \quad \tilde{\Gamma}_\phi = \frac{\tilde{\nu}_t}{\sigma_\phi} \tag{9}$$

where C_μ and σ_ϕ are empirical constants. Equation (8) includes the depth-averaged turbulent viscosity $\tilde{\nu}_t$ and diffusivity $\tilde{\Gamma}_\phi$. $\tilde{k}$ and its $\tilde{\varepsilon}$ dissipation can be calculated by two more differential equations:

$$\frac{\partial \bar{u}\tilde{k}}{\partial x} + \frac{\partial \bar{v}\tilde{k}}{\partial y} = \frac{\partial}{\partial x}\left(\frac{\tilde{\nu}_t}{\sigma_k}\frac{\partial \tilde{k}}{\partial x}\right) + \frac{\partial}{\partial y}\left(\frac{\tilde{\nu}_t}{\sigma_k}\frac{\partial \tilde{k}}{\partial y}\right) + G + P_{kv} - \tilde{\varepsilon} \tag{10}$$

and

$$\frac{\partial \bar{u}\tilde{\varepsilon}}{\partial x} + \frac{\partial \bar{v}\tilde{\varepsilon}}{\partial y} = \frac{\partial}{\partial x}\left(\frac{\tilde{\nu}_t}{\sigma_\varepsilon}\frac{\partial \tilde{\varepsilon}}{\partial x}\right) + \frac{\partial}{\partial y}\left(\frac{\tilde{\nu}_t}{\sigma_\varepsilon}\frac{\partial \tilde{\varepsilon}}{\partial y}\right) + C_1\frac{\tilde{\varepsilon}}{\tilde{k}}G + P_{\varepsilon v} - C_2\frac{\tilde{\varepsilon}^2}{\tilde{k}} \tag{11}$$

where G stands for the production of turbulent kinetic energy due to interactions of turbulent stresses with horizontal mean velocity gradients which can be expressed as follows

$$G = \tilde{\nu}_t\left[2\left(\frac{\partial \bar{u}}{\partial x}\right)^2 + 2\left(\frac{\partial \bar{v}}{\partial y}\right)^2 + \left(\frac{\partial \bar{u}}{\partial y} + \frac{\partial \bar{v}}{\partial x}\right)^2\right] \tag{12}$$

The coefficients C_1, C_2, σ_k and σ_ε in (10) and (11) are empirical constants. Equations (10) and (11) can be considered as depth-integrated forms of the three-dimensional k and ε equations, when a generation term P_{kv} has been added in the $\tilde{k}$-equation and $P_{\varepsilon v}$ in the $\tilde{\varepsilon}$-equation to account for turbulence generation due to the vertical velocity gradient, which occurs mainly near the bed. The generation G due to the horizontal velocity gradient is practically $\tilde{\nu}_t(\partial \bar{u}/\partial y)^2$ in the depth-averaged case. Since the additional generation term P_{kv} and $P_{\varepsilon v}$ depend strongly on the bottom friction, these terms are related to the bottom friction u_* in the following way (a detailed discussion is contained in Rastogi and Rodi, 1978):

$$P_{kv} = C_k\frac{u_*^3}{h} \quad \text{and} \quad P_{\varepsilon v} = C_\varepsilon\frac{u_*^4}{h^2} \tag{13}$$

where the local friction velocity $u_* = \sqrt{C_f\left(\bar{u}^2 + \bar{v}^2\right)}$. The empirical constants C_k and C_ε for channel flow determined by Rastogi and Rodi (1978), with the turbulent viscosity measured by Laufer in 1951 are:

$$C_k = \frac{1}{\sqrt{C_f}} \quad \text{and} \quad C_\varepsilon = 3,6\frac{1}{C_f^{3/4}}\sqrt{C_\mu}$$

The values of the empirical constants adopted are the ones of the 'standard' $k-\varepsilon$ model: C_μ=0.09, σ_ϕ=0.9, C_1=1.43, C_2=1.92, σ_k=1.0 and σ_ε=1.3.

This model has been applied to simulate the open channel flow (Rastogi and Rodi, 1978), the symmetric expansion flow (Chapman and Chin, 1982; Chapman, 1983) and the flow and pollutant diffusion in river (Rodi at al. , 1981).

Depth-integrated $\tilde{k} - \tilde{w}$ Model

At present, the depth-integrated mathematical models are very popularly used in water regions with large ratio of width to depth for engineering simulation and prediction (Heaps, 1969; Kuipers and Vreugdenhil, 1973; Yu and Zhu, 1993, and so on). However, most of these depth-integrated models only adopted low-order 0-equation turbulence models. Before 1988, users who intended to adopt the advanced two-equation closure for modeling their governing equations had no other choice, as there was only one depth-integrated turbulence two-equation model originated from 'standard' $k-\varepsilon$ model (the $\tilde{k}-\tilde{\varepsilon}$ model). On the other side, two-equation closure theory and corresponding models have made great progress; several effective models and their newly developed versions have been applied in different engineering areas. In 1988, the depth-integrated turbulence $\tilde{k}-\tilde{w}$ model was established by Yu and Zhang on the base of the new version of the k-w model, reported by Ilegbusi (1983, 1984). The revised k - w model demonstrated the same order of accuracy as the 'standard' $k-\varepsilon$ model, but better accuracy than the $k-\varepsilon$ model for some computational examples. This revised model can be expressed as follows (Ilegbusi and Spalding, 1982):

$$\rho\left(\frac{\partial k}{\partial t}+u_j\frac{\partial k}{\partial x_j}\right)=\frac{\partial}{\partial x_j}\left(\mu_{effk}\frac{\partial k}{\partial x_j}\right)+\rho P_k-C_\mu\rho k w^{1/2} \tag{15}$$

and

$$\rho\left(\frac{\partial w}{\partial t}+u_j\frac{\partial w}{\partial x_j}\right)=\frac{\partial}{\partial x_j}\left(\mu_{effw}\frac{\partial w}{\partial x_j}\right)+C_{1w}\mu_t(\text{grand}\Omega)^2 -C_{2w}\rho w^{3/2}\left(1+C'_{2w}\left(\frac{\partial L}{\partial x_j}\right)^2\right)+C_{3w}\rho\frac{w}{k}P_k \tag{16}$$

where Ω and L stand for the vorticity of mean movement and length scale of turbulence respectively, the effective diffusivities μ_{effk}, μ_{effw} in the k- and w- equations are:

$$\mu_{effk}=\mu+\mu_t/\sigma_k \qquad \mu_{effw}=\mu+\mu_t/\sigma_w \tag{17}$$

and the empirical constants for turbulence model C_μ, σ_k, σ_w, C_{1w}, C_{2w}, C'_{3w} and C_{3w} in Eqs. (15)-(17) are equal to 0.09, 1.0, 1.0, 3.5, 0.17, 17.47 and 1.12, respectively.

The local depth-integrated state of turbulence can be characterized by the following two turbulence parameters: the turbulence kinetic energy $\tilde{k}$ and the intensity of vorticity fluctuation $\tilde{w}$ in depth-averaged sense; the turbulent viscosity/diffusivity can be expressed as follows (Yu, 1988):

$$\tilde{\mu}_t=\rho\tilde{k}\tilde{w}^{-1/2} \qquad \tilde{\nu}_t=\tilde{k}\tilde{w}^{-1/2} \qquad \tilde{\Gamma}_t=\tilde{\nu}_t/\sigma_\phi \tag{18}$$

Here $\tilde{k}$ and $\tilde{w}$ are determined from following the two transport equations (Yu and Zhang, 1989):

$$\frac{\partial H\tilde{k}}{\partial t}+\frac{\partial H\tilde{u}\tilde{k}}{\partial x}+\frac{\partial H\tilde{v}\tilde{k}}{\partial y}=\frac{\partial}{\partial x}\left(\frac{\tilde{\nu}_t H}{\sigma_k}\frac{\partial\tilde{k}}{\partial x}\right)+\frac{\partial}{\partial y}\left(\frac{\tilde{\nu}_t H}{\sigma_k}\frac{\partial\tilde{k}}{\partial y}\right)+HP_k+HP_{kv}-C_\mu h\tilde{k}\tilde{w}^{-1/2} \tag{19}$$

$$\frac{\partial H\tilde{w}}{\partial t}+\frac{\partial H\bar{u}\tilde{w}}{\partial x}+\frac{\partial H\bar{v}\tilde{w}}{\partial y}=\frac{\partial}{\partial x}\left(\frac{\tilde{\nu}_t H}{\sigma_w}\frac{\partial \tilde{w}}{\partial x}\right)+\frac{\partial}{\partial y}\left(\frac{\tilde{\nu}_t H}{\sigma_w}\frac{\partial \tilde{w}}{\partial y}\right)$$
$$+C_{1w}\tilde{\nu}_t H\left|\frac{\partial}{\partial y}\left(\frac{\partial \bar{v}}{\partial x}-\frac{\partial \bar{u}}{\partial y}\right)\right|^2$$
$$-C_{2w}H\tilde{w}^{3/2}\left[1+C'_{2w}\left(\frac{\partial}{\partial x}\left(\frac{\tilde{k}}{\tilde{w}}\right)^{1/2}+\frac{\partial}{\partial y}\left(\frac{\tilde{k}}{\tilde{w}}\right)^{1/2}\right)^2\right] \qquad (20)$$
$$+C_{3w}H\frac{\tilde{w}}{\tilde{k}}P_k+HP_{wv}$$

The additional source terms P_{kv} and P_{wv} in Eqs. (19) and (20), produced mainly by the vertical velocity gradients near the bottom, can be expressed as follows (Yu, 1988):

$$P_{kv}=C_k u_*^3/H \qquad P_{wv}=C_w u_*^3/H^3 \qquad (21)$$

By using Laufer's open channel experiment result, i.e. $\tilde{\mu}_t=0.0765U*H$ to determine the empirical constants C_k and C_w, it can be obtained (Yu, 1988):

$$C_k=1/\sqrt{C_f} \qquad C_w=47.26C_{2w}/C_\mu^{3/2}C_f^{3/4} \qquad (22)$$

When Eqs. (19) and (20) are solved for modeling the submerged discharge, corresponding source terms S_k and S_w similar to S_{mx}, S_{my} and S_ϕ in Eqs. (2)-(3) should be added to express the effects of the local discharging outflow on the turbulence fields. Figure 2 shows a plane configuration for a waste heat discharged from one side into a rectangular water channel. The comparison of computational results with experimental data in different momentum flux ratios $V_e^2 B_e^2/U_0^2 B_0$ has been performed carefully (Yu and Zhang, 1989). The computational results by use of depth-integrated $\tilde{k}-\tilde{\varepsilon}$ and $\tilde{k}-\tilde{w}$ models configured the dimensionless eddy height H_i/B_0, re-attachment length Hi/Li of recirculation eddy and dimensionless jet width $(H_0-H_i)/Li$ (see Fig. 2). It has been found that when the outlet width or flowrate of discharge is relatively small, which is a situation frequently occurred in environmental engineering, the results computed by the $\tilde{k}-\tilde{w}$ model are closer to experimental data than those simulated by the $\tilde{k}-\tilde{\varepsilon}$ model. Because the jet width H_0-H_i can be regarded as a horizontal line source which produces the pollutant plume in the lower reach of the discharge outlet, to finely determine H_0-H_i has a significant and direct effect on the computational accuracy for simulating and predicting the spread and distribution of the plume. Figure 3 presents the computed velocity vector field, stream line, isotherm, water-depth contour, longitudinal velocity, depth-averaged turbulent parameters ($\tilde{k}$ and $\tilde{w}$) as well as depth-integrated turbulence viscosity $\tilde{\mu}_t$ for one of the computed nine cases

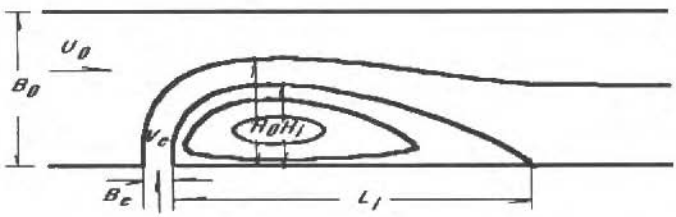

B_0 - channel width
B_e - jet width
U_0 - channel mean velocity
V_e - discharge mean velocity
H_0 - maximum jet penetration
H_i - eddy height
L_i - eddy length

Fig. 2 Flow Configuration

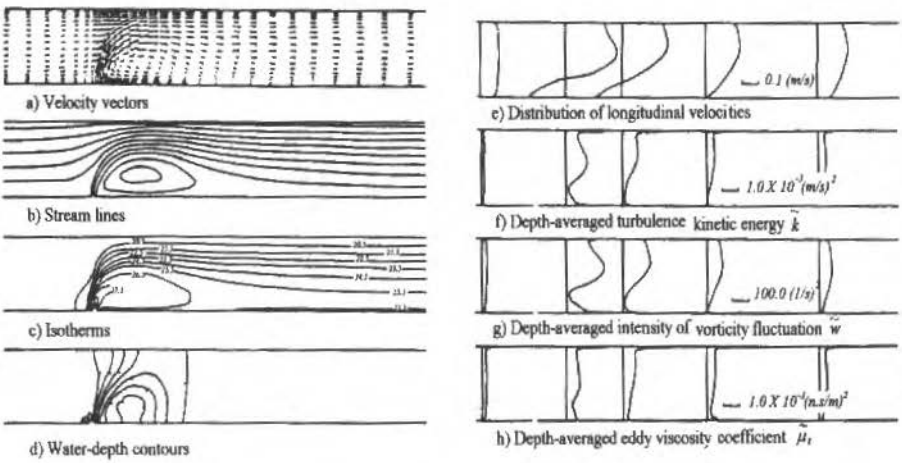

Fig. 3 Computed Results by Use of $\tilde{k} - \tilde{w}$ Model For One Discharge Case

Simulation For Flow and Thermal Diffusion in the Rhine River

General Description

Recently, the authors further investigated and applied the depth-integrated $\tilde{k} - \tilde{w}$ model to simulate the waste heat discharge for a practical problem in engineering: the cooling water was simultaneously discharged from three submerged outlets of an electric power plant into the Rhine River. The basic schematic diagram for the computation has been presented in Fig. 4. The fluvial dynamics parameters of the computational river which were obtained during the observation period are the following:

- The averaged flowrate $Q_0 = 1550\ m^3/s$;
- The average width $B_0 = 270\ m$;
- The average water-depth $\bar{h} = 4.85\ m$;
- The friction velocity $U_* = 0.068\ m/s$;
- The water temperature $T_0 = 7°C$, for this computation ϕ stands for the temperature T;
- The averaged side slop: about 1: 4.7;
- The flowrates and temperatures of thermal discharges from three outlets q_1, T_1, q_2, T_2 and q_3, T_3 are 4.0 m^3/s, 20°C, 1.75 m^3/s, 18.4°C and 6.0 m^3/s, 17.9°C respectively.

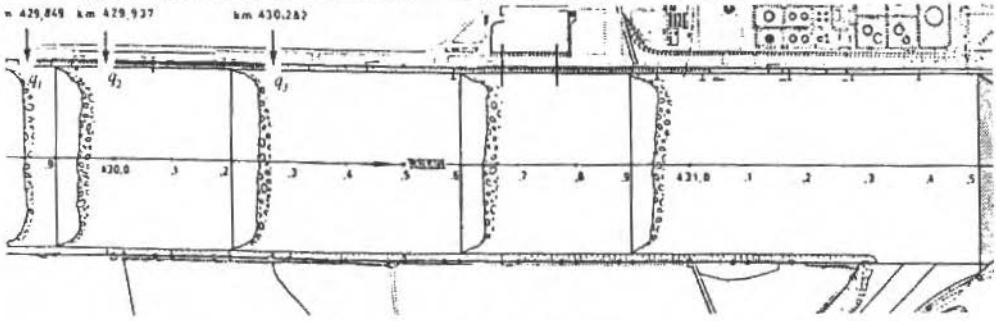

Fig. 4 Discharge Schematic Diagram

The number of nodes in the computational grid on a 1,217 m long segment is 256 along the river direction and 66 across the river direction, respectively. In the longitudinal direction (flow direction), the grid adopted piecewise uniform distribution and the grid lines near the three discharging outlets were denser than others; in the cross river direction, the grid spans near the two banks were finer than the ones in the center part of the river. The 'standard' or 'original' empirical constants of both $\tilde{k}-\tilde{\varepsilon}$ and $\tilde{k}-\tilde{w}$ models were adopted without any alteration, except the coefficients C_w and C_ε, which had to be calibrated in terms of the practical problem by the authors.

Boundary Conditions

The boundary conditions include those at the river inlet and outlet, those on the river banks and at the submerged outlets. At the river inlet, the velocity profile was taken to be the observational data, the temperature was set as the natural water temperature (70°C), the turbulent parameters for $\tilde{k}-\tilde{w}$ model were expressed by the empirical expressions $\tilde{k}=\sqrt{0.6U_0}U_*^2/C_\mu$ and $\tilde{w}=U_0U_*/0.6C_\mu H$, for the $\tilde{k}-\tilde{\varepsilon}$ model, $\tilde{\varepsilon}=U_0U_*^3/H$.

At the downstream section of the river, the zero gradient condition of all variables except $\bar{v}$ was imposed, i.e. $\frac{\partial\bar{u}}{\partial x}=\frac{\partial\bar{T}}{\partial x}=\frac{\partial\tilde{k}}{\partial x}=\frac{\partial\tilde{w}}{\partial x}=\frac{\partial\tilde{\varepsilon}}{\partial x}$, and it was assumed that there was no flow in the cross-river direction, i.e. $\bar{v}$. On the river banks, the impervious condition were imposed on the normal velocity, and the temperature $\bar{T}$ was assumed to satisfy the adiabatic condition. In addition, the longitudinal velocity $\bar{u}$ and turbulence parameters $\tilde{k}$, $\tilde{w}$ or $\tilde{\varepsilon}$ at the first grid node P near the banks satisfied the wall functions of the corresponding turbulence models (Ilegbusi, 1984, Yu and Zhang, 1989):

$$\frac{\bar{u}_p}{\sqrt{\tau_w/\rho}}=\frac{1}{\kappa}\ln\left|E\left(\frac{y_p\sqrt{\tau_p/\rho}}{\mu}\right)\right| \qquad \tilde{k}_p=\tau_p/\sqrt{C_\mu}\rho \tag{23}$$

$$\tilde{w}_p=\tilde{k}_p/\kappa^2y_p^2\sqrt{C_\mu} \qquad \tilde{\varepsilon}_p=C_\mu^{3/4}\tilde{k}_p^{3/2}/\kappa y_p \tag{24}$$

where $\kappa=0.4$, $E=0.9$ for smooth wall and $\tau_W\approx\tau_p$ in the simple flow situation. For the computation of practical engineering problems, E needs to be calibrated from site data.

Apart from the additional source terms P_{kv}, P_{wv} or $P_{\varepsilon v}$ resulting from the vertical integration, there are some extra source terms resulting from submerged outlets, such as the $\bar{S}_{mx}$ and $\bar{S}_{my}$ in the momentum equations, $\bar{S}_\phi$ in the transport equation and $\bar{S}_k$ and $\bar{S}_w$ or $\bar{S}_\varepsilon$ in the corresponding turbulence equations. These extra source terms can be dealt with as if they were part of the boundaries of a computational domain. In our computation, the submerged discharging outlet (see Fig. 5) was approximated by a vertical line source at the nodal point in the momentum equations, transport equations and the pressure-correction equation (p'- eq.) derived from the continuity equation and finite volume approach as shown in the literature (Patankar, 1980).

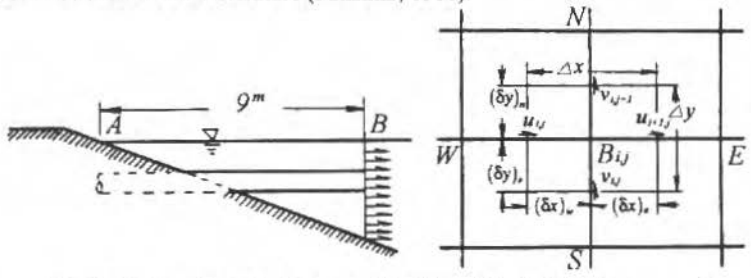

Fig. 5 Configuration of a Submerged Outlet and Nodal Grids Arrangement

Since these outlets were treated as part of the boundary for the computational domain when the discretization was carried out, the boundary conditions for submerged discharging, as the 'inner' boundary conditions, could be derived according to the conservation principle of various dependent variables at the control volume centered at a grid point B (Yu, 1988). For example, the pressure correction equation now contains a source term b, which is called 'mass source' in the literature (Patankar, 1980). For all cells, where no pollutant outlets are located, this source term is set to zero. On the other hand, if there is an outlet with flow rate q_B in the control volume B, this source term is then set to be equal to q_B. In the discretized form of the depth-integrated mathematical model, the additional source term appeared as $S_c\Delta x\Delta yH + S_p\Delta x\Delta yH\phi$ (Yu, 1988). With Δx and Δy being x- and y- direction widths of the control volume respectively, in the pressure correction equation, the steady discharge of the vertical linear source at nodal point B should not produce the pressure correction p'. Therefore, we set the pressure correction $\phi = p' = 0$, the 'source term' at nodal point B is only $q_B = S_c\Delta x\Delta yH$ and the linearized coefficient S_c of constant term should be equal to $q_B/\Delta x\Delta yH$ (see Fig. 5). The derivations for the 'source terms' in other equations are similar (see Yu, 1988 for detailed derivation) and are listed below without further derivation:

$\bar{u}-$eq. $$S_{p_{i,j}} = -\frac{1}{2}\frac{q_B}{H}\frac{1}{\Delta y(\delta x)_w} \qquad S_{p_{i+1,j}} = -\frac{1}{2}\frac{q_B}{H}\frac{1}{\Delta y(\delta x)_e} \tag{25}$$

$\bar{v}-$eq. $$S_{c_{i,j}} = -\frac{1}{2}\frac{q_B}{H}\frac{\bar{v}_B}{\Delta x(\delta y)_s} \qquad S_{c_{i,j+1}} = -\frac{1}{2}\frac{q_B}{H}\frac{\bar{v}_B}{\Delta x(\delta y)_n} \tag{26}$$

$$S_{p_{i,j}} = -\frac{1}{2}\frac{q_B}{H}\frac{1}{\Delta x(\delta y)_s} \qquad S_{p_{i,j+1}} = -\frac{1}{2}\frac{q_B}{H}\frac{1}{\Delta x(\delta y)_n} \tag{27}$$

$p'-$eq. $$S_{c_{i,j}} = \frac{q_B}{H}\frac{1}{\Delta x\Delta y} \tag{28}$$

$\bar{\phi}-$eq. $$S_{c_{i,j}} = \frac{q_B\bar{\phi}_B}{H\Delta x\Delta y} \tag{29}$$

$\tilde{k}-$eq. $$S_{c_{i,j}} = \frac{q_B\tilde{k}_B}{H\Delta x\Delta y} \qquad S_{c_{i,j}} = -\frac{q_B}{H\Delta x\Delta y} \tag{30}$$

$\tilde{\varepsilon}-$eq. $$S_{c_{i,j}} = \frac{q_B\tilde{\varepsilon}_B}{H\Delta x\Delta y} \qquad S_{c_{i,j}} = -\frac{q_B}{H\Delta x\Delta y} \tag{31}$$

$\tilde{w}-$eq. $$S_{c_{i,j}} = \frac{q_B\tilde{w}_B}{H\Delta x\Delta y} \qquad S_{c_{i,j}} = -\frac{q_B}{H\Delta x\Delta y} \tag{32}$$

where q_B stands for the discharge strength of the vertical line source at point B; $(\delta x)_e$, $(\delta x)_w$ express the x-direction spans between B and the east and west control volume faces; $(\delta y)_n$, $(\delta y)_s$ are the y-direction spans between B and the north and south control volume faces respectively (see Fig. 5). The equations (25)-(29) have been successfully taken as the outflow boundary conditions for simulating

several immersed outlets discharging waste heat and contaminants into the south estuary of the Yangtze River (Yu and Zhu, 1993), while an simple algebraic formula was used to express the turbulent viscosity and diffusivity of tidal currents. The Eqs. (30)-(32) were then firstly published, where $\tilde{k}_B$, $\tilde{\varepsilon}_B$ and $\tilde{w}_B$ could be determined by the empirical expressions used in the river inlet.

Details and Skills of Numerical Computation

Choice of turbulent diffusion coefficient

The given constant values of the coefficients C_ε and C_w in Eqs. (14) and (22) were determined by using Laufer's experimental result in small water channel. In order to obtain the usable values adaptable to model natural river, the dimensionless diffusivity $e^* = \tilde{\nu}_t / (U_* h \sigma_\phi)$ in the center part of the river reach was adopted, where the flow was assumed to be uniform. Fisher et al., (1979) reported that the value of the coefficient e^* was in the range of $0.4 \sim 0.9$ for a number of different rivers. Rodi at al (1981) adopted $e^* = 0.6$ to simulate the Rhine River and obtained a fair good agreement with the field measurements. In our computation, $e^* = 0.6$ was also adopted.

Computation of Bed-Shear Stress

The two components of bed-shear stresses in momentum Eqs. (2) and (3) should be computed by use of the quadratic friction law considering the effect of the bank slope (Rodi et al., 1981)

$$\tau_{bx} = \rho C_f \bar{u}\sqrt{\bar{u}^2 + \bar{v}^2} / \cos\varphi \qquad \tau_{by} = \rho C_f \bar{v}\sqrt{\bar{u}^2 + \bar{v}^2} / \cos\varphi \tag{33}$$

where φ stands for the inclination defined in Figure 6 and the friction coefficient C_f is not equal to a constant value similar to the situation in the rectangular channel. The C_f increases towards the edge of the shallow water regions. The variation of C_f can be evaluated by using Rodi's proposition presented in 1981.

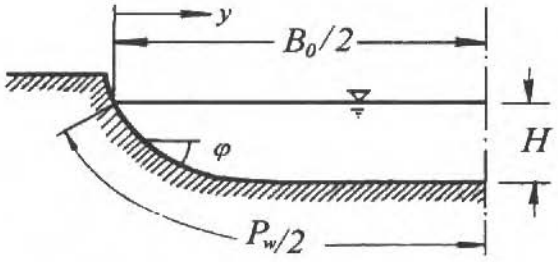

Fig. 6 The Cross-section of a Typical River Bank

Treatment of Additional Source Terms Produced by Vertical Integration

Since the variation of bottom topography and (or) water-surface are unavoidable, the terms produced by using Leibniz formula to integrate the three-dimensional governing equations should be analyzed carefully, as the effects of these terms could not be neglected at all. Our numerical investigation has shown that the produced terms which have a direct effect on computational results are (Yu, 1988):

$$\text{in u- equation} \quad S_x = -2\tilde{\mu}_t \frac{\partial u_s}{\partial x}\frac{\partial H}{\partial x} - \tilde{\mu}_t\left(\frac{\partial u_s}{\partial y} + \frac{\partial v_s}{\partial x}\right)\frac{\partial H}{\partial y} \tag{34}$$

$$\text{in v- equation} \quad S_y = -\tilde{\mu}_t\left(\frac{\partial v_s}{\partial x}+\frac{\partial u_s}{\partial y}\right)\frac{\partial H}{\partial x}-2\tilde{\mu}_t\frac{\partial v_s}{\partial y}\frac{\partial H}{\partial y} \tag{35}$$

where u_s and v_s stand for the surface velocity components in x- and y- directions, respectively. In the long and straight river reach with trapezoidal cross-section, while the variation of water-depth mainly occurred along the transversal direction, if the variation of water-surface elevation relatively to the water-depth is small enough, Eqs. (34) and (35) can then be expressed approximately in terms of following suggestions (Yu, 1988):

- The gradients of depth-integrated velocity components with respect to the x- and y- directions can be substituted for surface velocity components and
- The tranquil water-depth h can substitute the dynamic water-depth H.

In this case, Eqs. (34) and (35) can be simplified as follows:

$$\text{in u- equation} \quad S_x \cong -\tilde{\mu}_t\left(\frac{\partial \bar{u}}{\partial y}+\frac{\partial \bar{v}}{\partial x}\right)\frac{\partial h}{\partial y} \tag{36}$$

$$\text{in v- equation} \quad S_y = -2\tilde{\mu}_t\frac{\partial \bar{v}}{\partial y}\frac{\partial h}{\partial y} \tag{37}$$

After we approximated the depth-integrated velocities $\bar{u}$ and $\bar{v}$ to the surface velocities in Eqs. (2) and (3) and calculated the turbulence viscosity $\tilde{\nu}_t$ and diffusivity $\tilde{\Gamma}_\phi$ by Eq. (18), the equation system (1)-(4), (19), (20) or (11) became closed. These equations formed a set of two-dimensional non-linear partial differential equations with elliptical situation in the spatial scope. However, as the unknown variables $\bar{u}$, $\bar{v}$, H, $\tilde{k}$, $\tilde{w}$ or $\tilde{\varepsilon}$ and the effective viscosity $\tilde{\nu}_{eff}$ as well as the diffusivity $\tilde{\Gamma}_\phi$ are all coupled in a highly non-linear fashion, an adequate numerical solution must be sought for these equations.

In our computation, the SIMPLE-c (*Semi-Implicit Method for Pressure-Linked Equation-consistent*, Doormaal and Raithby, 1982) algorithm for iteratively solving all momentum and transport equations as well as pressure-correction equation has been adopted. Figures 7 and 8 clearly show the comparisons of variation of 'mass source', in which the 'mass source' excluding the two terms (36), (37) and including these terms on the right sides of the momentum Eqs. (2) and (3) has been recorded, respectively. If these two terms were neglected in the governing equations, the iteration process would show that larger fluctuation of 'mass source' appeared in the initial iteration stage and conversely, the iteration rapidly tended to be convergent only in limited 45 iteration steps

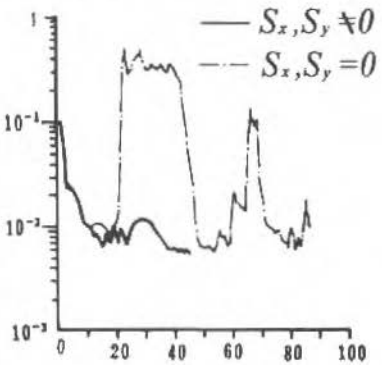

Fig. 7 Maximum Mass Source In Control Volume

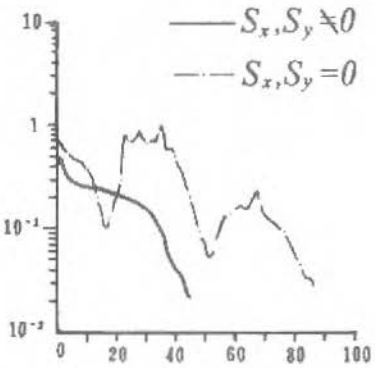

Fig. 8 Mass Source In All the Computational Domain

Water-Depth Correction Coefficients

Since the variations of bottom topography and (or) water-surface are generally quite large, the variations of bottom topography and (or) surface elevation should be included into the mathematical model. This can be achieved by introducing the water-depth correction coefficients, which were defined by Yu in 1991 as:

$$\alpha_{ij} = H_{ij} / \bar{h} = (h_{ij} + \Delta h_{ij}) / \bar{h}, \tag{38}$$

where $H_{i,j}$, $h_{i,j}$ and $\Delta h_{i,j}$ stand for the local dynamic water-depth, the local tranquil water-depth and the variation of $H_{i,j}$ respectively; $\bar{h}$ represents a characteristic water-depth, usually equal to the average tranquil water-depth of the main channel for a river reach. The water-depth correction coefficients are functions of space, and also of time for unsteady flow. The variation of $\alpha_{i,j}$ provides a consistent means to deal with the variation of water-depth and boundary geometry, for example, $\alpha_{i,j} = 0$ corresponds to land or islands and non-zero $\alpha_{i,j}$ represents a region occupied by water. The water-depth correction coefficient technique has been adopted to treat the variations of bottom topography and water-surface for modeling the tidal currents in the estuary of the Yangtze River (Yu and Zhu, 1993). By using finite volume approach, the water-depth correction coefficients can be classified according to two possible locations of a grid point within a control volume. Those associated with the center point of a control volume, the values of which approximately represent the fraction of volume occupied by fluid in the control volume, and those associated with the center points of control faces of a control volume, the values of which approximately represent the void fractions of corresponding control faces.

Computational Results

All the unknown variables were discretized with spatially staggered grids. The depth-integrated velocities $\bar{u}$ and $\bar{v}$ are computed at the faces of each main control volume, whereas the water-depth H, the temperature $\bar{T}$ and the turbulence parameters $\bar{k}$, $\bar{w}$, or $\bar{\varepsilon}$ are computed at the center of each cell. The SIMPLE-c algorithm (Doormaal and Raithby, 1982) was adopted to couple the vectorial quantities $\bar{u}$, $\bar{v}$ and the scalar quantities H, $\bar{T}$, $\bar{k}$, $\bar{w}$, or $\bar{\varepsilon}$. With the power-law scheme (Patankar, 1980) having lower numerical dissipation and higher numerical accuracy being used for the convective and diffusion terms, Eqs. (1)-(4), (19) and (20) or (11) are discretized with the finite volume approach. Iterations were performed at each solving step with an initial guess solution of the pressure (water-depth) field. The velocity components $\bar{u}$ and $\bar{v}$ corresponding to the guessed pressure field are solved from the momentum Eqs. (2) and (3) by using the so-called line-by-line method (Patankar, 1980)

associated with the wall functions. The pressure (water-depth) values are corrected with the line-by-line method again, from the pressure correction equation. In our model the used pressure correction equation and two velocity-correction equations, which calculated the corrected velocities, are similar to those in the literature (Patankar, 1980) and, therefore, have not been included. By using the corrected velocities and wall functions, the temperature transport equation and turbulence parameter equations could be solved, and the turbulent viscosity and diffusivity needed to be renewed at the end of each iteration. After that, the corrected pressure (water depth) is taken as a new guessed pressure (water-depth) and the iteration repeats itself until a pre-specified convergence is achieved. Due to the tedious process of the discretization of the governing equations and their low relevance to the theme of this paper, the detailed numerical procedures have not been included.

The computational results from $\tilde{k}-\tilde{w}$ model were compared with the observed depth-integrated longitudinal velocity and temperature distribution, and also compared with the corresponding numerical results from constant coefficient viscosity and diffusivity model and $\tilde{k}-\tilde{\varepsilon}$ model, respectively. These computations were performed by adopting a general-purpose computational program for elliptic situation involving the water-depth correction coefficients (Yu, 1994) under the same convergence indicators, which are the sum of the absolute values of the 'mass source' in the whole computational domain and the maximum mass source of one cell within the domain. The computations were finished when these indicators became smaller than 2.5% for solving the pressure correction equation. The maximum residue for solving temperature transport equation between two adjacent iteration cycles was less than $1x10^{6}$. The single block correction technique (Prakash and Patankar, 1981; Patankar, 1981) was adopted for accelerating the convergence of these computations. In order to investigate the newly developed turbulence $\tilde{k}-\tilde{w}$ model, different turbulence models such as constant coefficient viscosity and diffusivity model and $\tilde{k}-\tilde{\varepsilon}$ model were adopted in different side wall situations (vertical side and sloping bank). Figure 9 presents the computed local flow field near the three submerged outlets, in which reasonable flowing situations and details in the river have been shown clearly. The distributions of computed longitudinal velocities and temperature compared with the field data have been shown in the Figs. 10 and 11, respectively. For convenience, the x- and y- coordinates in these two figures represent the lower reach direction and cross-river direction of the river. In terms of the results from the temperature equation, the isotherms have been presented in Fig. 12, which clearly illustrates the development of pollutant plume in the areas both near the three submerged outlets and of lower reaches of these outlets. From the objective analysis and comparison, the following conclusions have been obtained (Yu, 1990; Yu, 1993)

- Without considering the effect of bottom topography on velocity and temperature distributions, for example, only adopting the simple and rough flat-bottomed approximation, the thermal plume will concentrate on the river bank, the computational result does not coincide with the measurements;
- By using depth-integrated $\tilde{k}-\tilde{w}$ and $\tilde{k}-\tilde{\varepsilon}$ models, the computed temperature distribution is different; the results computed by the newly developed $\tilde{k}-\tilde{w}$ model are better than the ones computed by the $\tilde{k}-\tilde{\varepsilon}$ model and
- The temperature distribution using the model with constant coefficient diffusivity has a relatively larger error in comparison with field data; this is very evident even at the lower reaches far from the discharging outlet.

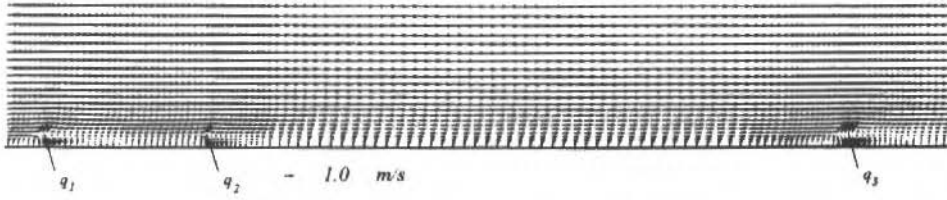

Fig. 9 Local Flow Field Near Three Submerged Outlets

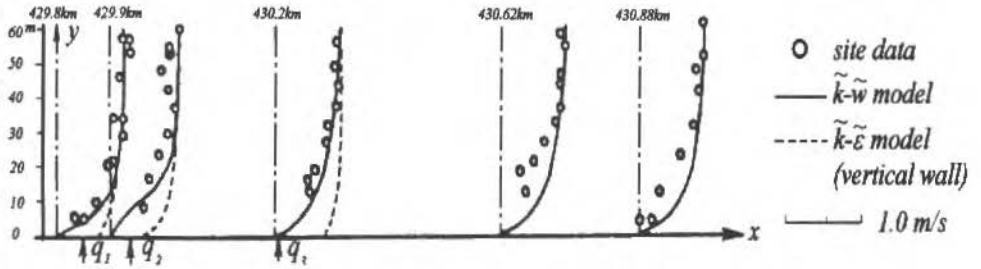

Fig. 10 Distribution of Longitudinal Velocities

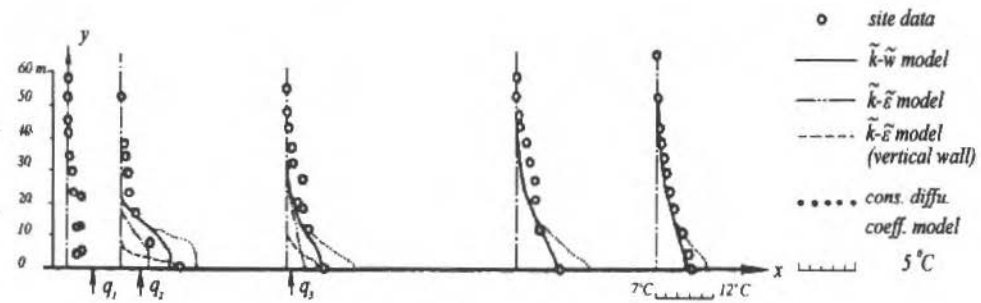

Fig. 11 Distribution of Temperature

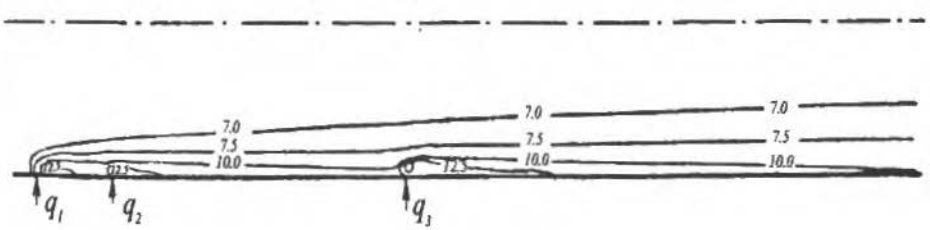

Fig. 12 Isotherms

Because of the poor information about constructions near the banks and on the bottom topography, such as the locations and sizes of docks, obstacles and pipeline systems in the lower reach of outlets, and also lack of detailed data about the side slopes, which in our computations had to be simplified as an averaged single value, there exist rather large differences between the computed velocity profiles and site data in the near bank regions at the sections located at 430.62 km and 430.88 km, respectively.

Discussion

It is recognized that up to the present, the advanced and practicable method for illustrating turbulent mean behavior in two-dimensional depth-integrated simulation and prediction is to adopt two-equation turbulence closure models. The newly developed depth-integrated turbulence two-equation closure $\tilde{k}-\tilde{w}$ model is available to be used to compute turbulent mean behavior in engineering. The authors' computational results have shown that the temperature fields using depth-

integrated $\tilde{k}-\tilde{w}$ and $\tilde{k}-\tilde{\varepsilon}$ models have some important differences, that is, in the case of narrower widths of jet outlet or smaller jet flowrate, the results computed by the $\tilde{k}-\tilde{w}$ model are better than the ones computed by the $\tilde{k}-\tilde{\varepsilon}$ model. In the presented computational example of practical engineering significance, the widths and flowrates of the three outlets of cooling water discharge are smaller relatively to the width and global flowrate of the river. Hence, it can be concluded that the jet widths simulated by the $\tilde{k}-\tilde{w}$ model should be more correct than the widths computed by the $\tilde{k}-\tilde{\varepsilon}$ model and the pollutant plume in the lower reach simulated by the $\tilde{k}-\tilde{w}$ model, including the position and temperature distribution, would have a reasonably higher accuracy.

Possible Improvement and Development

In the past 18 years while modellers tried to adopt turbulence two-equation model to simulate and predict flow and pollutant transport in engineering, the development and application of depth-integrated two-equation closure models was not satisfactory indeed. Recently, Booij (1989) pointed out that in Rodi's depth-integrated $\tilde{k}-\tilde{\varepsilon}$ model the turbulence production due to horizontal velocity gradients and the production due to the presence of the bottom were not weighed correctly; this had led to a much exaggerated bottom influence. A modified model suggested by Booij (1989) was shown to yield better results for modeling mixing layer between a river and a harbor in a scale model, in which a man-made weighing to regulate these two parts of turbulence production has been used. In fact, it is still doubtful that the artificial weighing of the turbulence productions due to horizontal and vertical velocity gradients is in lack of sufficient theoretical basis. For the $\tilde{k}-\tilde{w}$ model developed by the authors, further numerical and experimental investigations are also needed. Moreover, the applicability of a few well-behaved, valuable versions of turbulence two-equation models in the depth-integrated sense has not been investigated sufficiently, even after the utilization of some of these models has become quite popular in various industrial departments. On the other hand, engineers still tend to adopt the traditional constant viscosity and diffusivity with those coefficients being roughly estimated empirically. Such questionable estimation combined with obsolete models doubtless led to large differences between numerically simulated results and observed ones. The severe gap between the theoretical research in turbulence modeling and its practical developments has further retarded improvement of the highly-accurate depth-integrated turbulence two-equation models and their application to natural waters. The failure of the theory to meet practical demands should be rectified as soon as possible. It is expected that further research, investigation and application of advanced turbulence two-equation closure models will become very popular among researchers and engineers in the area of depth-integrated modeling. At present, it is possible to develop some new depth-integrated turbulence two-equation closure models based on some newly developed versions, which have corrected some shortages of the 'standard' $k-\varepsilon$ model. The authors expect that the newly developing features for the existent $\tilde{k}-\tilde{\varepsilon}$ and $\tilde{k}-\tilde{w}$ models can set up a higher standard for numerically modeling turbulent flows and pollutant transport phenomena in terms of computational efficiency, algorithm extensibility and universality, as well as model robustness.

Acknowledgment

The support of CNPq (Brazilian National Council for Scientific and Technological Development) through Process No. 301089/94-9(NV) is gratefully acknowledged. The authors also thank Prof. Marcius F. Giorgetti of the School of Engineering at São Carlos - USP for his useful assistance in the preparation of this paper.

References

Boo, R., 1989, Depth-Averaged $k-\varepsilon$ Modeling, In: Proceedings of IAHR XXIII Congress, Technical Section A, Turbulence in Hydraulics A, 199-206, Ottawa, Canada, 21-25, August.

Chapman, R.S. and Kuo, Y. C., 1982, "A Numerical Simulation of Two-Dimensional Separated Flow in a Symmetric Open-Channel Expansion Using the Depth-Integrated Two-Equation ($k-\varepsilon$) Turbulence Closure Model", Dept. of Civil Engineering, Virginia Polytechnic Institute and State University.

Chapman, R.S., 1983, "Two-Equation Depth-Averaged Turbulence Closure for Modeling Geometry-Dominated Flows", Environmental Laboratory U.S. Army Engineer Waterways Experiment Station.

Fisher, H.B. el al., 1979, "Mixing in Inland and Coastal", Academic Press.

Heaps, N.S., 1969, "A Two-dimensional Numerical Sea Model", Phil. Trans., Roy. Soc., A265, pp.93-137.

Ilegbusi J.O. and Spalding, D.B., 1982, "Application of a New Version of the $k-w$ Model of Turbulence to a Boundary Layer with Mass Transfer", CFD/82/15.

Ilegbusi, J.O., 1983, "Revised Two-Equation Model of Turbulence", Imperial College of Science and Technology, Rep. CFD/83/5.

Ilegbusi, J.O., 1984, "Proposal for Wall Function for Friction and Mass Transfer", CFD/84/12.

Jones, W.P. and Lander, B.E., 1973, "The Calculation of Low Reynolds Number Phenomena With a Two-Equation Model of Turbulence", Int. J. Heat Mass Transfer. Vol. 16, pp. 1114-1130.

Kuipers, J. and Vreugdenhil, C.B., 1973, "Calculations of Two-Dimensional Horizontal Flow", Delft Hydraulics Laboratory Rep. S163, Part I.

Laufer, J., 1951, "Investigation of Turbulent Flow in a Two-Dimensional Channel", NACA Report 1053.

Patankar, S.V., 1980, "Numerical Heat Transfer and Fluid Flow", Hemisphere Publishing Corporation and McGraw Hill Book Company.

Patankar, S.V., 1981, "A Calculation Procedure for Two-Dimensional Elliptic Situations", Numerical Heat Transfer, Vol. 4, pp. 409-425.

Prakash, C. and Patankar, S.V., 1981, "Combined Free and Forced Convection in Vertical Tubes with Radial Internal Fines", ASME J. Heat Transfer, Vol. 103, pp. 566-572.

Rastogi A.K. and Rodi, W.A., 1978, "Prediction of Heat and Mass Transfer in Open Channels", J of the Hydraulics Division, ASCE, no. Hy3.

Rodi, W.A. et al., 1981, "Prediction of Flow and Pollutant Spreading in Rivers", Transport Models for Inland and Coastal Waters, Proceedings of a Symposium on Predictive Ability, Academic Press, pp. 63-111.

Van Doormaal, J.P. and Raithby, G.D., 1982, "Enhancement of the SIMPLE Method for Predicting Incompressible Fluid Flows", Numerical Heat Transfer, Vol. 7, no. 2, pp. 147-152.

Yu, L. and Zhang, S., 1988, "A New Depth-Averaged Two-Equation ($\bar{k}-\tilde{w}$) Turbulent Closure Model", Proceedings of the Third Inter. Symp. on Refined Flow Modeling and Turbulence Measurements, Tokyo, Japan, July 26-28 or J. of Hydrodynamics, Vol. 1, no. 3, pp. 47-54 (1989).

Yu, L., 1988, "The Turbulent Model and Numerical Research for The Turbulent Transport of The Contaminants in Water Environment" (in Chinese), Ph.D. Dissertation, Hohai.

Yu, L., 1990, "Application of New Depth-Averaged Two-Equation ($\bar{k}-\tilde{w}$) Turbulent Closure Model to Numerical Simulation for a River", Proceedings of the 7th Congress of APD-IAHR, Vol. 3, Beijing, China, Nov. pp. 157-162.

Yu, L., 1991, "Two-Dimensional Variable Water-Depth Mathematical Model for Tidal Flows and Numerical Computation for Discharges of Waste Heat and Contaminate in South Estuary of the Yangtze River", Proceedings of International Symposium on Environmental Hydraulics, Oct. Hong Kong.

Yu, L., 1993, "Establishment, Numerical Investigation and Application of Depth-Averaged Two-Equation Turbulent Closure Model ($\bar{k}-\tilde{w}$)", Proceedings of Annual Conference of Australian Mathematical Society, Wollongong, Australia, July.

Yu, L. and Zhu, S., 1993, "Numerical Simulation of Discharged Waste Heat and Contaminants into the South Estuary of the Yangtze River", Mathl. Comput. Modeling Vol. 18, pp. 107-123.

Yu, L, 1994, "Elements of Numerical Computation and Simulation of Flow and Contaminants Transport", A Lecture Course, Dept. of Hydraulics and Sanitary Engineering, São Carlos School of Engineering, University of São Paulo, Brazil, March-July.

RBCM - J. of the Braz. Soc. Mechanical Sciences
Vol. XVIII - No.4 - 1996 - pp. 355-373

ISSN 0100-7386
Printed in Brazil

Added Mass and Damping on Bottom-Mounted Rectangular Cylinders

Paulo de Tarso T. Esperança
Sergio Hamilton Sphaier
Universidade Federal do Rio de Janeiro
Departamento de Engenharia Naval e
COPPE - Programa de Engenharia Oceânica
21945 Rio de Janeiro, RJ Brasil

Abstract

Looking for a major comprehension from the reason of the strong variations in the hydrodynamic coefficients of added mass and damping when a two-dimensional body oscillates vertical close to the free surface in finite depth we analyze this problem using eigenfunction expansions. It can make evident the parameters involved on resonances and the behavior for low and high frequencies. Introducing separation of variables the boundary value problem is transformed in an eigenvalue problem of Sturm-Liouville kind. This procedure was used by Yeung (1981) to determine the hydrodynamic coefficients for a truncated vertical cylinder with circular section piercing the free surface oscillating in water of finite depth, Yeung and Sphaier (1989) to consider the interference of vertical walls of a canal in the hydrodynamic coefficients, McIver and Evans (1984) in the problem of a submerged vertical cylinder oscillating near the free surface and Esperança (1993) for the two-dimensional case.

In the present paper we confirm the occurrence of negative added mass when the body oscillates close to the free surface, and obtain finite values of the added mass and damping coefficient in dimensional form for the zero frequency limit as expected. The negative values of the added mass are related to two kind of resonant wave modes occurring close to values of the frequency parameter, wave number times half rectangle width, $m_0^! a$, is equal to $n\pi$ and $n\pi/2$. For these frequencies the damping coefficient is equal to zero or achieves a local maximum value, and stationary waves characterize the internal flow. Negative added mass for the frequency parameter going to zero is obtained for shallow water, when the emergence of the rectangle is larger than 1/3 of the water depth. A shallow water approach is also presented, allowing us to describe the wave motion for small water depth and clearance. The results derived from the shallow-water solution is in good agreement with the one of the complete solution. Further we present the solution for the case of rectangular cylinder heaving on the free surface and compare the results with results presented by Bai and Yeung (1974), Bai (1977) and by Drimer, Agnon and Stiassnie (1992).

Keywords: Motion of Floating Bodies, Waves, Ship Design, Added Mass and Damping, Botton - Mounted Rectangular Cylinder.

Introduction

In the design of modern ships their motion behavior in waves plays an important role. In the case of ship, the viscous effect can be neglected, the fluid considered incompressible, the body forces be derived from a potential function and the flow assumed irrotational. Further, we can assume that the wave length are of the same order as the ship width (high frequencies), the wave amplitude small and the body considered slender. Under these condition the problem can be linearized and a strip theory developed: the body is subdivided in many sections along the length; two-dimensional problems are solved for the motion of these sections and the hydrodynamic reaction forces on the body under action of incoming waves can be calculated. Incorporating the buoyancy and gravity forces, the motion of the floating body can be determined according to the strip theory.

The hydrodynamic forces are subdivided in two groups: excitation forces, resulting from the action of the incoming waves and their diffraction, considered the body fixed; and radiation forces, resulting from the oscillatory motion of the body in calm waters.

In the linearized theory of oscillatory motion of a body close or on the free surface the hydrodynamic reaction is split up in two different components: one in phase with the acceleration and the other in phase with the velocity. The coefficient of proportionality force in phase with acceleration is called added mass and the relation of the force in phase with velocity and velocity is called damping coefficient.

Manuscript received: January 1995. Technical Editor: Carlos Alberto Carrasco Altemani

The added mass for a body in finite domain has a constant positive value. When the body oscillates on the free surface in depends on the frequency, on the local depth and whether we have a two- or three- dimensional problem. In the case of a two-dimensional body oscillating on the free surface in finite depth in the low frequency limit the added mass goes to infinity, while for the case of finite depth it goes to a finite value. The damping coefficient is related to the energy flux in the outgoing waves and necessarily is always positive. For high frequency it must goes to zero.

The determination of the added mass and the damping coefficient for a two-dimensional cylinder has motivated research over the last decades. Ursell in 1949 solved the problem of a heaving circular cylinder on the surface in deep water. He used a multipole series and a wave source potential, Havelock source, the represent the fluid flow motion. Later on he developed solutions for the sway and roll motions. In 1953 Grim presented a solution for the heaving problem using also a multipole expansion. After that Tasai (1959) used conformal mapping to extend the solution to non-circular sections. The use of a there parameter Lewis transform cause some restrictions in the method. To avoid the conformal mapping Frank (1967) discretized the body contour and used sources distribution with constant intensity to represent the velocity potential.

Extending the approach used by Ursell (1949), Yu and Ursell (1961) developed a solution for the case of finite depth. In evaluating the added mass for low frequency their results showed a tendency of growth to infinity.

Bai and Yeung (1974) using two numerical procedures, one based on a variational method (finite-element and eigenfunction expansion) and another using the Green's second identity with a logarithmic fundamental solution, obtained finite limit for added mass in low frequency too. Bai (1997) confirmed these results using also a numerical procedure. Yeung (1975) developed a hybrid model combining integral equation and eigenfunction expansion and determined the hydrodynamic forces for two-dimensional bodies near or in the free surface. This behavior was obtained analytically by Ursell (1976) reviewing the earlier paper with Yu. For the low frequency problem the boundary conditions are of the Neumann kind, that is, the boundary conditions contain only derivative of the potential and, consequently, the potential has a unknown constant, which was the center of a long polemic about the problem.

Continuing the investigation Sayer and Ursell (1976) determined the behavior of the derivative of the added mass in relation to the wave number times the radius of the cylinder. In the discussion of the paper Yeung and Newman (1976) presented a procedure based on the method of matched asymptotic expansions to determine the constant and then the value of the added mass for low frequency. They proved that the constant does not depend on the section form and confirm that is value is the same obtained by Ursell (1976) for a circle. Similar results were obtained by Keil (1974), extending the multipole expansion used by Grim (1953).

McIver an Linton (1991) following a procedure similar to the one used by Yeung (1976) analyzed the differences in the added masses for a bottom mounted cylinder and a floating cylinder for low frequencies. Since the boundary value problems are the same, the difference in added mass corresponds to differences in the constants.

For a horizontal circular submerged cylinder close to the free surface Ogilvie (1963) concluded that the added mass assumes negative values for some frequencies. This was supported by experimental results obtained by Chung (1997). Newman, Sortland and Vinje (1984) used the matched asymptotic expansion method to calculate the added mass and damping coefficient for a submerged two-dimensional vertically infinite rectangle executing heave motion.

Yeung (1981) solved the problem of a vertical truncated circular cylinder in finite depth using an eigenfunction series solution. This procedure allows us to take into account more precisely the behaviour of the added mass for low frequencies. Yeung and Sphaier (1989) showed that this limit is finite when the cylinder oscillates in a channel. McIver and Evans (1984) used the eigenfunction method for the case of a bottom mounted vertical circular cylinder and determine negative values for the added mass in some frequency range.

In the present work we apply the same procedure used by Yeung (1981) and Yeung and Sphaier (1989) to study the hydrodynamic properties for a bottom-mounted two-dimensional rectangular cylinder using series of eigenfunction to represent the velocity potential. A complete linear solution is

obtained and the behavior of added mass and damping is presented. Further an asymptotic solution for high frequencies and a shallow-water solution for low frequency are developed. For small clearance, between the of the cylinder and the calm water level, we determined the range of frequency for negative added mass. We also have applied this methodology for the case of a floating rectangle and evaluated the added mass and damping. We obtained good agreement with the results presented by Bai (1977) and Bai and Yeung (1974), and presented by Drimer, Agnon and Stiassnie (1992), which used a simplified model based on the eigenfunction expansion to analyze the behavior of a rectangular breakwater.

The Boundary Value Problem

The water depth is defined as h_e, the width of the bottom-mounted rectangle is equal to 2a an the clearance between the top of the rectangle and the free surface at the rest position is h_i. The rectangle height is $d = h_e - h_i$. To describe the fluid flow we use a cartesian system of coordinates Oxz. The origin is located on the mid point of the top of rectangle and the axis Oz points vertically upwards.

We assume that the viscous effect can be neglected, the fluid considered incompressible, the body forces derived from a potential function and the flow is irrotational. Under these assumptions, the velocity can be derived from a potential $v = \nabla\Psi$, and the potential function satisfies Laplace equation, $\nabla^2\Psi = 0$. Function Ψ is e0xpressed in the form:

$$\psi(x, z, t) = \Re\left[-i\sigma\xi\Phi(x, z)\exp(-i\sigma t)\right] \tag{1}$$

where σ represents the frequency of the oscillation, ξ the complex amplitude of the vertical motion $\xi = \bar{\xi}\exp(i\delta)$, $\bar{\xi}$ the module of the amplitude, δ the please angle and $i = \sqrt{-1} \cdot \Re$ means the real part.

Function Φ must satisfy the Laplace equation over the fluid domain

$$\nabla^2\Phi = 0 \tag{2}$$

and the following boundary conditions:

$$\frac{\partial\Phi(x, z)}{\partial z} = \frac{\sigma^2\Phi(x, z)}{g} \qquad z = h_i \tag{3}$$

$$\frac{\partial\Phi(x, z)}{\partial z} = 1 \qquad z = 0; |x| \le a \tag{4}$$

$$\frac{\partial\Phi(x, z)}{\partial z} = 1 \qquad z = -d; |x| \ge a \tag{5}$$

$$\frac{\partial\Phi(x, z)}{\partial x} = 0 \qquad -d \le z \le 0; |x| = a \tag{6}$$

$$\frac{\partial\Phi(x, z)}{\partial x} \mp im_0^e\Phi(x, z) \to 0 \qquad m_0^e x \to \pm\infty \tag{7}$$

Internal and External Boundary Value Problems

The fluid domain is divided in two parts, an internal and an external region as showed in Fig. 1. The internal domain is a fluid rectangle located over the top of the cylinder with the same width as the body, 2a, and height equal to h_i, $\{-a \le x \le a;\ 0 \le z \le h_i\}$. The external domain is located at the side of the body and the internal domain so that $\{x \ge a;\ -d \le z \le h_i\}$. We introduce the potential functions Φ^i and Φ^e, so that $\Phi = \Phi^i$ in the internal region and $\Phi = \Phi^e$ in the external region.

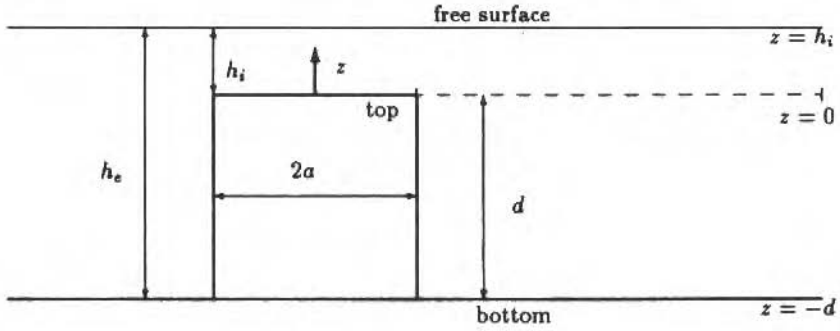

Fig. 1 Bottom-mounted Rectangular Section

Φ^i satisfies equation (2), the boundary conditions (3) and (4). Further, the fluid motion is symmetric about the Oz axis, then we can study the fluid flow in a half part of the domain and impose $\partial\Phi^i(x, z)/\partial x = 0$ for $0 \le z \le h_i$; $x = 0$.

Φ^e satisfies equation (2), the boundary conditions (3), (5), (6) and (7).

Both boundary value problem can not uniquely determined, since we did not defined boundary conditions for $0 \le z \le h_i$, $|x| = a$ We introduce complementary boundary condition representing the compatibility between the two potential given by the continuity on the pressure:

$$\Phi^i(x, z) = \Phi^e(x, z) \quad 0 \le z \le h_i \quad x = a \tag{8}$$

and continuity of the horizontal velocities:

$$\partial\Phi^e(x, z)/\partial x = \begin{cases} 0 & \text{for } -d \le z \le 0 \quad x = a \\ \partial\Phi^i(x, z)/\partial x & \text{for } 0 \le z \le h_i \quad x = a \end{cases} \tag{9}$$

Eigenfunction Expansions

The internal solution, satisfying (2), (3), (4) and the symmetry condition, can be written as the sum of a particular Φ_p^i and a homogeneous solution Φ_h^i :

$$\Phi^i = \Phi_p^i + \Phi_h^i = z - h_i + g/\sigma^2 + \frac{h_i b_0 \cos(m_0^i x) Z_0^i(z)}{\cos(m_0^i a)} + \sum_{n=1}^{\infty} \frac{h_i b_n \cosh(m_n^i x) Z_n^i(z)}{\cosh(m_n^i a)} \tag{10}$$

where b_n are unknown complex coefficients, $b_n = b_n^R + i b_n^I$, Z_n^i the eigenfunctions, m_0^i and m_n^i are the eigenvalues. m_0^i is the first eigenvalue, the solution of the dispersion equation $\sigma^2/g - m\tanh(mh_i) = 0$. m_n^i are the others eigenvalues, solutions of $\sigma^2/g + m\tanh(mh_i) = 0$. The eigenfunctions are:

$$Z_0^i(z) = \frac{\cosh(m_0^i z)}{\sqrt{N_0^i}} \quad \text{and} \quad Z_n^i(z) = \frac{\cos(m_n^i z)}{\sqrt{N_n^i}} \quad \text{for } n \ge 1 \tag{11}$$

with

$$N_0^i = \frac{1}{2}\left[1 + \frac{\sinh(2m_0^i h_i)}{2m_0^i h_i}\right] \quad \text{and} \quad N_n^i = \frac{1}{2}\left[1 + \frac{\sin(2m_n^i h_i)}{2m_n^i h_i}\right] \text{ for } n \geq 1 \qquad (12)$$

Similarly, the external solution is given by:

$$\Phi^e(x, z) = \frac{d_0 \exp(im_0^e x) Z_0^e(z)}{m_0^{e2} \exp(im_0^e a)} + \sum_{l=1}^{\infty} \frac{d_l \exp(-m_l^e x) Z_l^e(z)}{m_l^{e2} \exp(-m_l^e a)} \qquad (13)$$

where d_n are unknown complex coefficients, $d_n = d_n^R + id_n^I$, Z_n^e the eigenfunctions, m_0^e and m_n^e are the eigenvalues. m_0 is the first eigenvalue, the solution of the dispersion equation $\sigma^2/g - m\tanh(mh_e) = 0$. m_n are the other eigenvalues, solutions of $\sigma^2/g + m\tan(mh_e) = 0$. The eigenfunctions are:

$$Z_0^e(z) = \frac{\cosh\left[m_0^e (z + d)\right]}{\sqrt{N_0^e}} \quad \text{and} \quad Z_l^e(z) = \frac{\cos\left[m_l^e (z + d)\right]}{\sqrt{N_l^e}} \quad \text{for } l \geq 1 \qquad (14)$$

with

$$N_0^e = \frac{1}{2}\left[1 + \frac{\sinh(2m_0^e h_e)}{2m_0^e h_e}\right] \text{ and } N_l^e = \frac{1}{2}\left[1 + \frac{\sin(2m_l^e h_e)}{2m_l^e h_e}\right] \quad \text{for } l \geq 1 \qquad (15)$$

The eigenvalues m_0^i and m_0^e, related to the dispersion equation, indicate the presence of progressive waves in the internal and external domains.

Determination of the Coefficients

The determination of the coefficients of the internal and the external solutions can be accomplished by applying the compatibility conditions (8) and (9) and utilizing the orthogonality property of the Z_l^i and Z_l^e functions. Let us define the operators:

$$\zeta_k^j = \frac{1}{h_2 - h_1} \int_{h_1}^{h_2} g(x, z) Z_k^j(z)\, dz \qquad (16)$$

where the superscript j is equal to i or e and the superior limit the integral h_2 is equal to h_i and the inferior limit is 0 or -d depending on whether we are dealing with the internal or the external eigenfunction Z_l^i or Z_l^e respectively.

Applying ζ_k^i and ζ_k^e respectively to equations (8) and (9) and using (10) and (13) we obtain:

$$f_k + b_k = \sum_{l=0}^{\infty} C_{kl}^i d_l \qquad (17)$$

and

$$q_j d_j = \sum_{m=0}^{\infty} C_{jm}^e b_m \qquad (18)$$

where f_k, C_{kl}^i, q_j and C_{jm}^e are the results of the application of ζ_k^i and ζ_k^e to the potential functions Φ^e, Φ_p^i and Φ_h^i. Substituting (17) in (18) we can solve the system for **b** and the recover **d**.

Hydrodynamic Coefficients and Wave Profile

The hydrodynamic force acting on the body is given by the integral of the hydrodynamic pressure $p = -q\partial\Psi^i/\partial t$ obtained from the linearized Euler's integral on the top of the rectangle:

$$F(t) = \int_s p\frac{\partial\Psi^i}{\partial t}ds = -\mu\dot{U}(t) - \lambda U(t) = -\left(\mu + i\frac{\lambda}{\sigma}\right)\dot{U}(t) \tag{19}$$

where the body vertical velocity is given by $U(t) = \Re\left[-i\sigma\bar{\xi}\exp(i\delta - i\sigma t)\right] = \sigma\bar{\xi}\sin(\delta - \sigma t)$, $\dot{U}$ is the acceleration and μ and λ are the added mass and the damping coefficient respectively. Introducing equation (10) in (19) a straightforward integration leads to the following expressions for the hydrodynamic complex coefficient:

$$\mu + i\frac{\lambda}{\sigma} = 2\rho h_i a\left[\frac{b_0 \tan(m_0^i a) Z_0^i(0)}{m_0^i a} - \sum_{n=1}^{\infty}\frac{b_n \tanh(m_n^i a) Z_n^i(0)}{m_n^i a} + \left(1 - \frac{g}{\sigma^2 h_i}\right)\right] \tag{20}$$

The free surface elevation $\eta(x, t)$ is also obtained from the linearized Euler's integral:

$$\eta^j(x,t) = \Re\left\{-\frac{1}{g}\frac{\partial\Psi^j(x, h_i, t)}{\partial t}\right\} = \frac{\sigma^2\bar{\xi}}{g}\left[\Phi_R^j(x, h_i)\cos(\delta - \sigma t) - \Phi_I^j(x, h_i)\sin(\delta - \sigma t)\right] \tag{21}$$

where Φ_R^j and Φ_I^j the real and imaginary parts of the complex potential $\Phi^j = \Phi_R^j + i\Phi_I^j$ and the superscript j depends on whether we are considering the internal domain, j = i and $|x| \le a$ or the external domain, j = e and $|x| \ge a$. The real and the imaginary potential in these domains are given by:

$$\Phi_R^i = z - h_i + g/\sigma^2 + \frac{h_i b_0^R \cos(m_0^i x) Z_0^i(z)}{\cos(m_0^i a)} + \sum_{n=1}^{\infty}\frac{h_i b_n^R \cosh(m_n^i x) Z_n^i(z)}{\cosh(m_n^i a)} \tag{22}$$

$$\Phi_I^i = \frac{h_i b_0^I \cos(m_0^i x) Z_0^i(z)}{\cos(m_0^i a)} + \sum_{n=1}^{\infty}\frac{h_i b_n^I \cosh(m_n^i x) Z_n^i(z)}{\cosh(m_n^i a)} \tag{23}$$

$$\Phi_R^e = \frac{\left\{d_0^R \cos\left[m_0^e(x-a)\right] - d_0^I \sin\left[m_0^e(x-a)\right]\right\} Z_0^e(z)}{(m_0^e)^2} + \sum_{l=1}^{\infty}\frac{d_l^R \exp(-m_l^e x) Z_l^e(z)}{(m_l^e)^2 \exp(-m_l^e a)} \tag{24}$$

$$\Phi_I^e = \frac{\left\{d_0^I \cos\left(\left[m_0^e(x-a)\right] + d_0^R \sin\left[m_0^e(x-a)\right]\right)\right\} Z_0^e(z)}{(m_0^e)^2} + \sum_{l=1}^{\infty}\frac{d_l^I \exp(-m_l^e x) Z_l^e(z)}{(m_l^e)^2 \exp(-m_l^e a)} \tag{25}$$

Behavior in Shallow Waters

To analyze the behavior for small clearances and water depths we use the shallow-water approach. The mean potential function $\bar{\Phi}(x)$ is defined as:

$$\bar{\Phi}^j(x) = \frac{1}{h_2 - h_1}\int_{h_1}^{h_2} \tilde{\Phi}^j(x, z)\, dz \tag{26}$$

where the index j means internal or external domain, the inferior limit in the integral h_1 is 0 or -d, the superior limit is h_i e h_e respectively and $\tilde{\Phi}^j(x)$ is the potential in shallow waters.

Integration of Laplace equation in the vertical coordinate, application of the boundary conditions and use of the approximation $\tilde{\Phi}^j(x, h_i) \approx \bar{\Phi}^j(x)$ yields to

$$\frac{\partial^2 \bar{\Phi}^j(x)}{\partial x^2} + \frac{\sigma^2 \bar{\Phi}^j(x)}{g h_j} = \text{r. s. v.} \tag{27}$$

where r.s.v. means the right side value depending on index j. For j = i the equation refers to the internal domain and r.s.v. is equal to $1/h_i$, while for j = e the domain is the external and r.s.v. is equal to 0.

From the dispersion equation we obtain for shallow water

$$(\tilde{m}_0^e)^2 h_e = (\tilde{m}_0^i)^2 = \sigma^2/g \tag{28}$$

Equation (27) conducts to the solutions:

$$\bar{\Phi}^i(x) = b_0 \cos(\tilde{m}_0^i x) + g/\sigma^2 \tag{29}$$

$$\bar{\Phi}^e(x) = d_0 \exp(i\tilde{m}_0^e x) \tag{30}$$

In the internal region we have a stationary wave $b_0 \cos(\tilde{m}_0^i x)$, the homogeneous solution. The particular solution is a constant representing the motion of the fluid as a rigid body. For the external domain we have a progressive wave. The complex coefficients b_0 and d_0 are to be determined using equations (8) and (9)

$$b_0 = \frac{-i\tilde{m}_0^e h_e g/\sigma^2}{i\tilde{m}_0^e h_e \cos(\tilde{m}_0^i a) + \tilde{m}_0^i h_i \sin(\tilde{m}_0^i a)} \quad \text{and} \quad d_0 = \frac{\tilde{m}_0^i h_i \sin(\tilde{m}_0^i a) \exp(-i\tilde{m}_0^e a)\, g/\sigma^2}{i\tilde{m}_0^e h_e \cos(\tilde{m}_0^i a) + \tilde{m}_0^i h_i \sin(\tilde{m}_0^i a)} \tag{31}$$

According to the shallow-water approximation the vertical force $\tilde{F}(t)$ acting on the body is given by

$$F(t) = -\rho\sigma^2 \Re\{2\xi \exp(-i\sigma t) \int_0^a \bar{\Phi}^i(x)\, dx\} \tag{32}$$

Introducing the solution for the internal potential in shallow waters, equation (29), we obtain for the hydrodynamic coefficients:

$$\tilde{\mu} = \frac{\rho g (\tilde{m}_0^e h_e)^2 \sin(2\tilde{m}_0^i a)}{\tilde{m}_0^i \sigma^2 \left\{ \left[\tilde{m}_0^i h_i \sin(\tilde{m}_0^i a)\right]^2 + \left[\tilde{m}_0^e h_e \cos(\tilde{m}_0^i a)\right]^2 \right\}} - \frac{2\rho g a}{\sigma^2} \tag{33}$$

$$\tilde{\lambda} = \frac{2\rho g\,(\tilde{m}_0^{\,e} h_e)\,(\tilde{m}_0^{\,i} h_e)\sin^2(\tilde{m}_0^{\,i} a)}{\tilde{m}_0^{\,i}\,\sigma\,\{[\tilde{m}_0^{\,i} h_i \sin(\tilde{m}_0^{\,i} a)]^2 + [\tilde{m}_0^{\,e} h_e \cos(\tilde{m}_0^{\,i} a)]^2\}} \tag{34}$$

with the limit values for $\tilde{m}_0^{\,e}\, a \to 0$

$$\tilde{u} = \frac{2}{3}\frac{a}{he}\left(\frac{h_e}{h_i} - 3\right) \qquad \tilde{\lambda} = 2\sqrt{\frac{a}{h_e}} \tag{35}$$

where $\varepsilon = \tilde{m}_0^{\,e}/\tilde{m}_0^{\,i} = (h_i/h_e)^{1/2}$ in (33) and (34) is the "clearanceness" parameter.

Introducing (29) in (21) we obtain the expression of the free surface elevation in the internal domain:

$$\bar{\eta}^{\,i}(x,t) = \frac{\sigma^2 \xi \cos(m_0^i x)}{g}\,[b_R \cos(\delta - \sigma t) - b_I \sin(\delta - \sigma t)] + \xi \cos(\delta - \sigma t) \tag{36}$$

We observe that for $\tilde{m}_0^{\,i}\, a = n\pi$, with $n \geq 1$ the imaginary part of the coefficients b_0 and d_0 vanish,

$$b_0 = b_R = -\frac{g}{\sigma^2}\frac{1}{\cos(\tilde{m}_0^{\,i} a)} = -\frac{g}{\sigma^2}\frac{1}{(-1)^n} \tag{37}$$

and the wave contribuition of the added mass and the damping coefficient are zero. The added mass is negative and given just by the motion of the fluid as a rigid body $\mu = -2\rho g a/\sigma^2$. All the properties depending on the esternal potential vanish, which means that the fluid in the external domain is at rest. On the other hand a stationary oscillation is present in the internal domain with potential, horizontal velocity and wave profile given by:

$$\bar{\Phi}^{\,i}(x) = g/\sigma^2\left[1 + (-1)^{n+1}\cos(\tilde{m}_0^{\,i} x)\right] \tag{38}$$

$$\frac{\partial \bar{\Phi}^{\,i}(x)}{\partial x} = -\tilde{m}_0^{\,i}\, b_R \sin(\tilde{m}_0^{\,i} x) \tag{39}$$

$$\bar{\eta}^{\,i}(x,t) = \bar{\xi}\cos(\delta - \sigma t)\left[1 + (-1)^{n+1}\cos(\tilde{m}_0^{\,i} x)\right] \tag{40}$$

The wave elevation has a behavior similar to a resonant mode: there is a standing wave in the internal domain, while outside there is no motion. For x = a the horizontal flux and the elevation of the free surface are always zero. At this point the standing wave has a vertical motion (crest/through) but the surface elevation remains equal zero since the fluid motion as a rigid body compensate the wave component and the wave lengh $\tilde{L}_i \equiv 2\pi/\tilde{m}_0^{\,i} = 2a/n$, is a fraction of the rectangle width, since $\tilde{m}_0^{\,i}\, a = n\pi$ where n is an integer ≥ 1.

Now we observe the behavior when $\tilde{m}_0^{\,i}\, a = (2n-1)\pi/2$ with $n \geq 1$. We can identify another resonant mode for this case. The internal and the external potential functions and the horizontal fluid velocities are:

$$\bar{\Phi}^{\,i}(x) = \frac{g}{\sigma^2}\left[1 + i(-1)^n \cos(\tilde{m}_0^{\,i} x/\varepsilon)\right]; \quad \frac{\partial \bar{\Phi}^{\,i}(x)}{\partial x} = \frac{ig\tilde{m}_o^{\,i}}{(\varepsilon\sigma^2)}\left[(-1)^{n+1}\sin\left(\tilde{m}_0^{\,i} x\right)\right]; \tag{41}$$

and

$$\bar{\Phi}^e(x) = \frac{g}{\sigma^2}\{\cos[\tilde{m}_0^e(x-a)] + i\sin[\tilde{m}_0^e(x-a)]\}$$
$$\frac{\partial\bar{\Phi}^e(x)}{\partial x} = \frac{\tilde{m}_o^e g}{\sigma^2}\{-\sin[\tilde{m}_o^e(x-a)] + i\cos[\tilde{m}_o^e(x-a)]\} \quad (42)$$

For x = a

$$\bar{\Phi}^i(a) = \bar{\Phi}^e(a) = g/\sigma^2 \text{ and } \frac{\partial\bar{\Phi}^i(a)}{\partial x} = ig\tilde{m}_o^i/(\varepsilon\sigma^2) = \frac{\partial\bar{\Phi}^e(a)}{\partial x} = ig\tilde{m}_o^e/\sigma^2 \quad (43)$$

Now the wave profile in the internal domain is given by

$$\bar{\eta}^i(x,t) = (-1)^{n+1}\frac{\bar{\xi}}{\varepsilon}\cos(m_0^i x)\sin(\delta-\sigma t) + \bar{\xi}\cos(\delta-\sigma t) \quad (44)$$

and the wave length $\tilde{L}_i = 2a[(2n-1)/2]$ with $n \geq 1$, that rectangle width is equal an integer number of wave lengths plus half wave length with wave nodes located at $|x| = a$. The nodes move vertically because of the fluid motion as a rigid body. There is a time oscillatory flux under the nodes. Reduction of the clearance, for a constant water depth, implies in an increase of the wave amplitude. For these frequencies the wave component of the added mass also vanishes, but the damping is different from zero. Writing the damping coefficient, Eq. (34), as a function of the product $\tilde{m}_0^i a$ is:

$$\tilde{\lambda}(\tilde{m}_0^i a) = \frac{2\rho g a\varepsilon h_i h_e \tilde{m}_0^i a \sin^2(\tilde{m}_0^i a)}{\sigma\{[\tilde{m}_0^i a h_i \sin(\tilde{m}_0^i a)]^2 + [\tilde{m}_0^i a\sqrt{h_i h_e}\cos(\tilde{m}_0^i a)]^2\}} \quad (45)$$

The analysis of its derivative with respect to $\tilde{m}_0^i a$ indicates that $\tilde{\lambda}$ assume local maximum values at this points.

The High Frequency Problem

Introduction of the high frequency assumption in boundary condition on the free surface (3) yields to

$$\Phi^i(x,z) = 0 \qquad \text{for } z = h_i \quad (46)$$

and consequently a modification in the radiation condition, not prescribing the presence of diverging waves.

The procedure to obtain the asymptotic solution of the problem is the same used to reach the complete solution

The potential in the internal domain is given by:

$$\Phi_\infty^i(x,z) = \sum_{n=0}^{\infty}\frac{h_i b_n \cosh(m_n^i x) Z_n^i(z)}{\cosh(m_n^i a)} + (z-h_i) \quad (47)$$

where the eigenfunctions, the normalizing factors and the eigenvalues are given by:

$$Z_n^i(z) = \frac{\cos(m_n^i z)}{\sqrt{N_n^i}};\ N_n^i = 1/2;\ m_n^i = \frac{(2n+1)\pi}{2h_i} \text{ with } 0 \leq n \leq \infty \quad (48)$$

In the external domain the eigenfunction expansion is given by:

$$\Phi^e_\infty(x,z) = -\sum_{k=0}^{\infty} \frac{d_k Z^e_k(z)\ \exp(-m^e_k\, x)}{m^{e\,2}_k \exp(-m^e_k\, a)} \tag{49}$$

where the eigenfunctions, the normalizing factors and the eigenvalues are given by:

$$Z^e_k(z) = \frac{\cos(m^e_k\, z + d)}{\sqrt{N^e_k}};\ N^e_k = 1/2;\ m^e_k = \frac{(2k+1)\pi}{2h_e} \quad \text{with} \quad 0 \le n \le \infty \tag{50}$$

Two differences from the complete solutions (10) and (13) are to be noted. First, the particular solution is modified, and the progressive mode does not appear. Consequently, the damping coefficient is zero.

Solving the problem and evaluating the hydrodynamic force we obtain the expression of the nondimensional added mass:

$$\mu_\infty = -2\rho h_i \sum_{n=0}^{\infty} \frac{b^R_n \tanh(m^i_n\, a)\sqrt{2}}{m^i_n} + 2\rho a h_i \tag{51}$$

Rectangular Cylinder Piercing the Free Surface

We consider now the case of the section heaving on the free surface. The x-axis coincides with the free surface at rest position. $h_i = 0$ and d is the rectangle draft. The solution is given by

$$\Phi^i = \Phi^i_p + \Phi^i_h = \frac{z^2 + 2h_e z - x^2}{2(h_e - d)} + \sum_{n=0}^{\infty} b_n \frac{\cosh(p_n x)\, Z^i_n(z)}{\cosh(p_n a)} \tag{52}$$

where b_n are unknown coefficients of the homogenous solution, Z^i_n the eigenfunctions and p_n are the eigenvalues. Applying a similar procedure as presented above we obtain the added mass and damping coefficient:

$$\mu + i\frac{\lambda}{\sigma} = 2\rho\left(b_0 a + \sum_{k=1}^{\infty} \sqrt{2b_k}\,(-1)^k \frac{\tanh(p_k a)}{p_k}\right) + 2\rho\left(\frac{d^2 - 2h_e d}{2(h_e - d)}a - \frac{a^3}{6(h_e - d)}\right) \tag{53}$$

Results and Conclusion

Using the methodology developed here we determined the added mass and damping coefficient for a bottom mounted rectangular cylinder. For all calculations we used 20 internal terms of the eigenfunction expansion and 60 external terms. First we observe the effect of the clearance on the hydrodynamic coefficients for fixed rectangle width. Figures 2 to 5 present nondimensional added mass ($\mu/\rho a^2$) and damping coefficient ($\lambda/\rho a^2 (g/a)^{1/2}$) as functions of the nondimensional parameter $m^i_0\, a$ the internal wave number times half width. The relation half width to water depth is given by $a/h_e = 0.10$ and 0.20. Results are presented for values of the relation clearance to water depth $h_i/h_e = 0.05$, 0.10, and 0.50, using the complete solution and the solution for high frequency. From these results we can say that: 1) the added mass and the dimensional damping coefficient assume finite values for low frequency; 2) for large clearance, small values of a/h_i, the added mass is positive for all frequencies. Negative values appear for small clearance, large values of a/h_i. The frequency range of negative added mass increases by increasing a/h_i; 3) results for the added mass from the complete solution converge to the asymptotic solution for high frequency (see also Table 1).

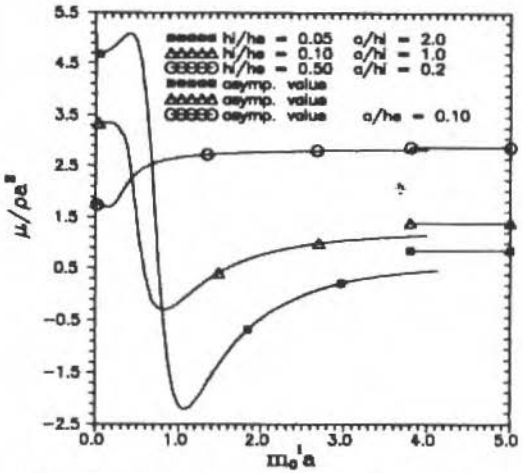

Fig. 2 Nondimensional Added Mass Versus Internal Wave Numbe

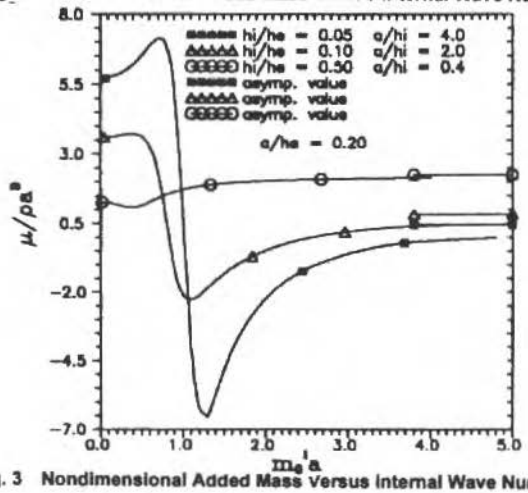

Fig. 3 Nondimensional Added Mass Versus Internal Wave Number

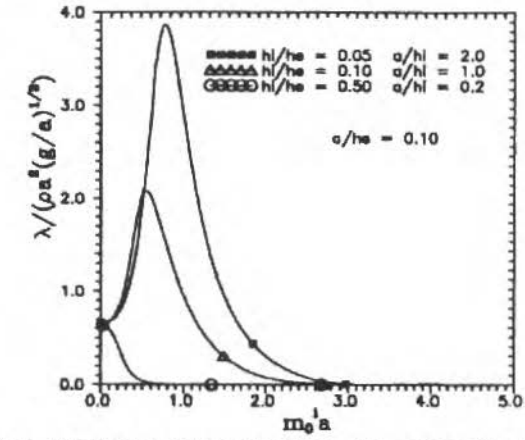

Fig. 4 Nondimensional Damping Versus Internal Wave Number

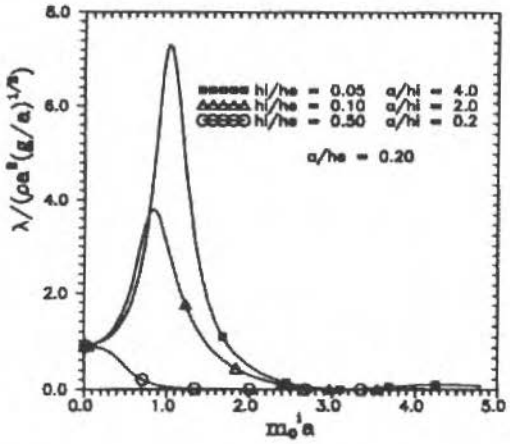

Fig. 5 Nondimensional Damping Versus Internal Wavw Number

Figures 6 and 7 show results of added mass and damping coefficient for a case with a much smaller clearance, $h_i/h_e = 0.01$ and $a/h_e = 0.10$. We also present results obtained with Newman, Sortland and Vinje (1984) solution for a rectangular cylinder with the same width and infinite depth, and calculation using Frank's close-fit method for a submerged square cylinder in finite water depth. The frequency parameter and the non-dimensional forms are the same used by Newman, Sortland and Vinje. Using the eigenfunction expansion and Newman, Sortland and Vinje solutions the hydrodynamic coefficients are determined by integrating the pressure only on the top of the cylinder while in Frank's method bottom and top side are considered. Discrepancies appear for low frequencies due to the different approaches. It is to note that an infinite limit for the added mass is expected in the solution presented by Newman et al.

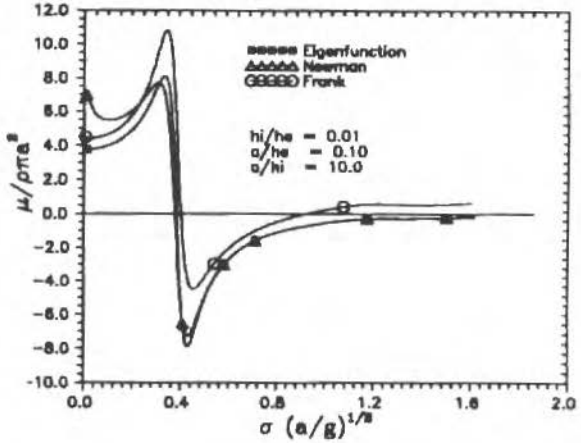

Fig. 6 Nondimensional Added Mass Versus Frequency

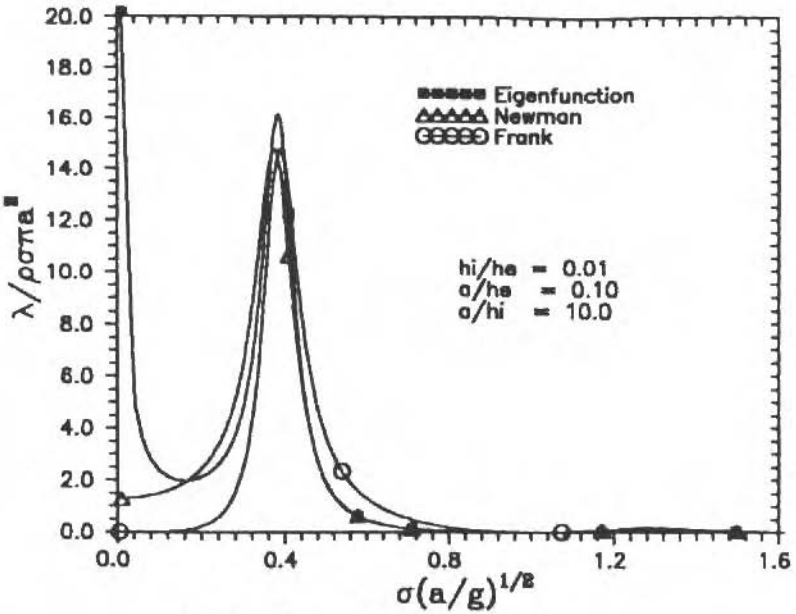

Fig. 7 Nondimensional Damping Versus Frequency

In Figures 8 and 9 we present the influence of the rectangle width in the hydrodynamic coefficients for a fixed clearance. The clearance is 5% of the water depth $h_i/h_e = 0.05$, and the values for the relation width to water depth are $a/h_e = 0.01$, 0.5, 1.0 and 2.0 corresponding to width to clearance $a/h_i = 0.20$, 10.0, 20.0 and 40.0. These leads to the same conclusions presented above.

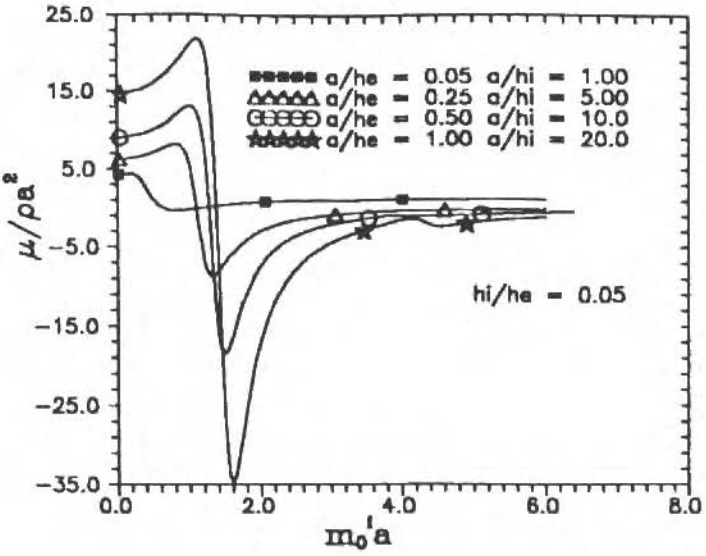

Fig. 8 Nondimensional Added Mass Versus Internal Wave Number

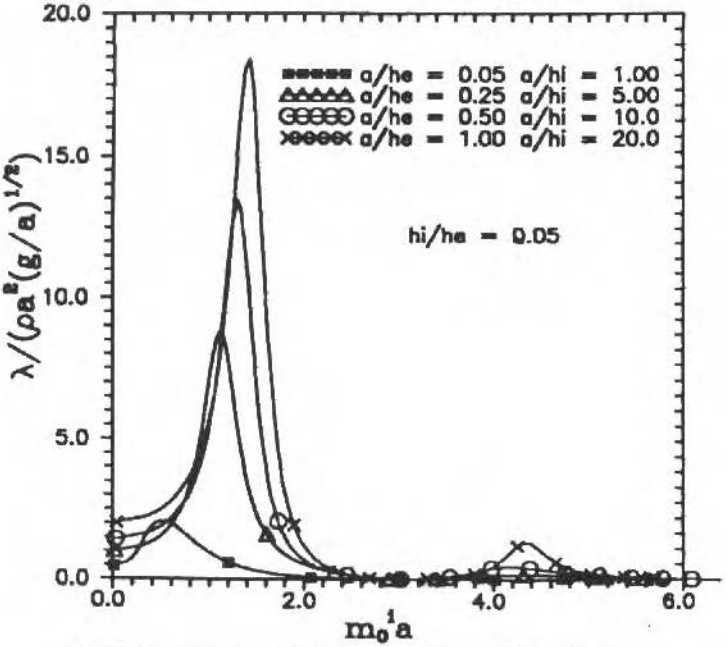

Fig. 9 Nondimensional Damping Versus Internal Wave Number

In Figures 10 and 11 we compare the complete and the shallow-water solutions. In this case h_i/h_e = 0.5 and a/h_e = 5.0 corresponding to a/h_i = 100.0, a very small clearance case. The agreement is very good for all frequencies.

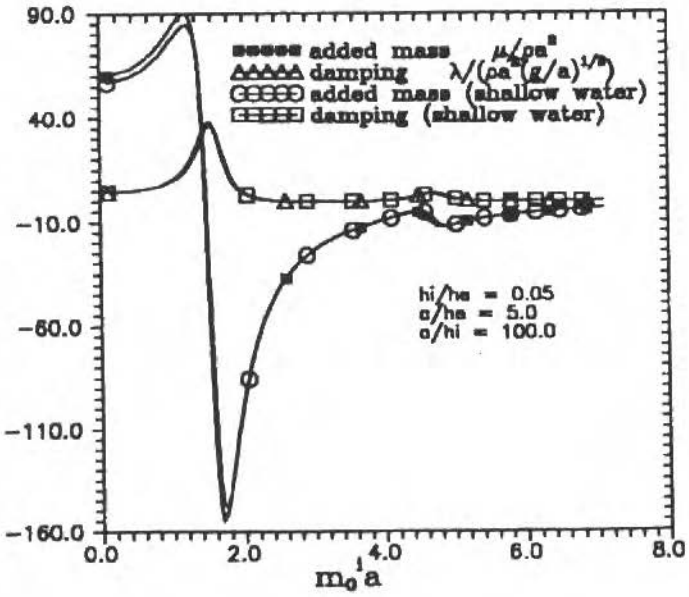

Fig. 10 Nondimensional Hidrodynamic Coefficients

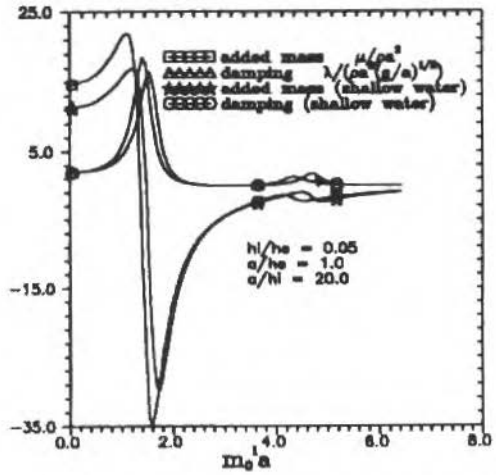

Fig. 11 Nondimensional Hidrodynamic Coefficients

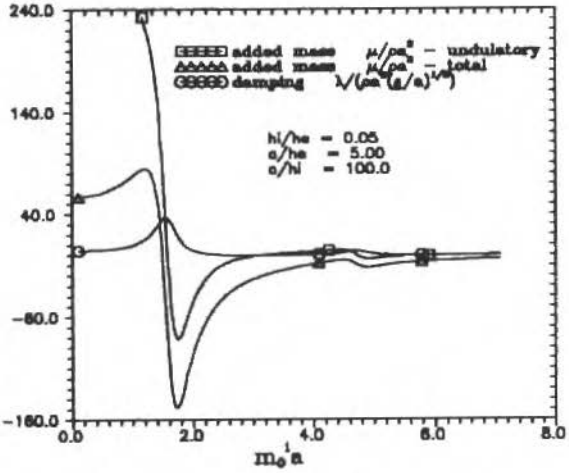

Fig. 12 Nondimensional Hidrodynamic Coefficients in Shallow Water

Two contributions determine the added mass (20). One part due to the fluid motion as a rigid body in the upper part of the rectangle. The other part has an undulatory character due to the waves. In Fig. 12 the total added mass, the contribution of the undulatory term to the added mass and the damping coefficient are plotted in nondimensional form as function of the frequency parameter $m_0^i a$ for shallow water. The contribution due to the wave motion is zero when the frequency parameter is equal to $\pi/2$, and simultaneously the damping coefficient is maximum. This corresponds to the second kind of resonance presented in the behavior in shallow water section. A standing wave appears over the rectangle with length equal to two times the rectangle width. The modes are located on $x = \pm a$, originating an oscillatory flux from the internal to the external regions. A second mode can be observed for $m_0^i a = 3\pi/2$. In this case the wave length is equal to 4a/3.

Values of added mass for different parameters h_i/h_e and a/h_e obtained from the complete solution (EIGEN) were compared with values for the high frequency approach (HASYMP), and values published by McIver and Linton (1991) for low frequency limit (LINTON) . Table 1 contains these results. By comparison the agreement can be considered very good.

Table 1 Added Mass for High and Low Frequencies

a/d	h_i/h_e	a/h_e	μ_f Linton	μ Eigen	μ_∞ Hasymp	μ Eigen
0,5	0,333	0,333	1,398	1,403	1,398	1,389
0,5	0,500	0,250	1,102	1,109	2,049	2,045
0,5	0,666	0,167	1,294	1,296	2,732	2,727
1,0	0,500	0,500	0,626	0,629	1,406	1,397
1,0	0,666	0,333	0,704	0,710	2,083	2,078
1,0	0,875	0,125	1,722	1,739	3,452	3,448
2,0	0,333	1,333	1,080	1,085	0,460	0,457
2,0	0,500	1,000	0,084	0,085	0,844	0,830
2,0	0,875	0,250	1,030	1,035	2,750	2,743

For a fixed relation a/d we observe from Table 1 that the added mass for $m_0^i\, a \to 0$ decreases and then increases for increasing h_i/h_e. Further the limit value of the added mass for the shallow-water solution assumes negative values when $h_i > h_e/3$ (Eq. 35). This limit does not means necessarily shallow waters in the internal domain since we are dealing with three parameters: $m_0^i\, a$, $m_0^i\, h_i$ and $m_0^e\, h_e$ .Since the external domain is infinite shallowness is defined by small $m_0^e\, h_e$. In the domain it does not depend only on $m_0^i\, h_i$ but also on how large a/h_i is. Figure 13 presents results of the nondimensional added mass and damping coefficient for a very small value of $m_0^i\, a$ as function of h_i/h_e and a/h_i, using the complete solution. Since the values of a/h_i are small, the results for added mass do not agree with the limit value obtained in section on behavior in shallow waters. But we have a exact agreement for the damping coefficient. Table 2 presents results for added mass obtained from (20) and (33). For large values of a/h_i = 10, 100 and 1000, the differences are about 50, 5 and .5% respectively, confirming what was expected.

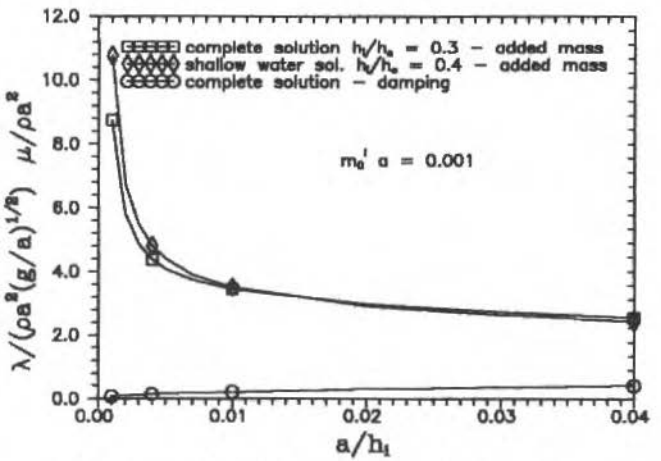

Fig. 13 Nondimensional added mass as function of a/h_i

Table 2 Added Mass for Shallow Waters for $m_0^i a = 0.001$

h_r/h_e	.3	.3	.4	.4
a/h_i	Compl.	Shallow	Compl.	Shallow
0.001	8.74	0.00022	10.75	-0.00033
0.01	3.43	0.0022	3.49	-00033
0.1	2.05	0.022	3.49	-0.0033
1.0	1.45	0.22	0.61	-0.33
10	3.32	2.22	-2.57	-3.33
100	23.30	22.22	-32.59	-33.33
1000	223.3	222.22	-332.59	-333.33

In Figures 14 and 15 we present results for added mass $\mu = \mu/(\rho 2ad)$ and damping coefficient $\lambda = \lambda/(\rho\sigma 2ad)$ for a rectangular cylinder, with half width to draft = 1.0 and water depth / draft = 1.5, 2.0, 3.0, 4.0 and 5.0, heaving on the free surface. Results for these cases are presented by Bai and Yeung (1974) and Bai (1977). Although we do not plot their results here, we can say the agreement is very good except for some differences for low frequencies.

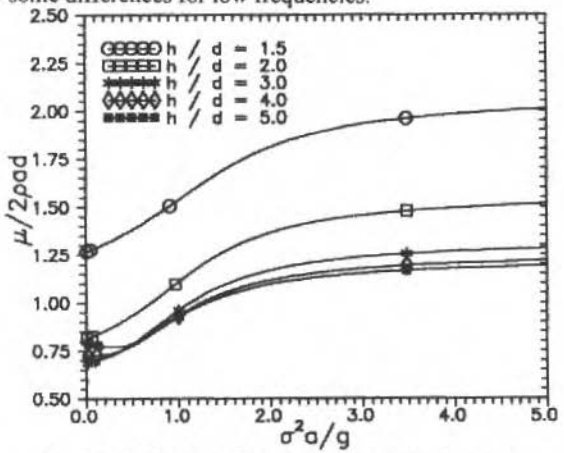

Fig. 14 Added Mass for a Rectangle on the Free Surface

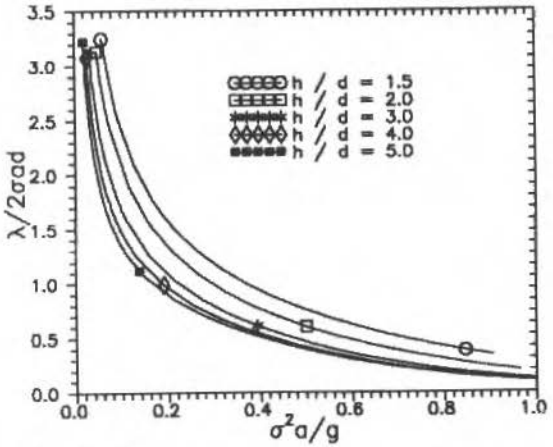

Fig. 15 Damping Coefficient for a Rectangle on the Free Surface

Yeung, R. W., 1981, "Added Mass and Damping of a Vertical Cylinder in Finite-depth Waters". Applied Ocean Research, 3:119-133.

Yeung, R. W. and Newman, J. N., 1976, "In the Discusion of Ursell (1976)". In 11th Symp. on Naval Hydrodynamics.

Yeung, R. W. and Sphaier, S. H., 1989, "Wave-interference Effects on a Truncated Cylinder in a Channel". Journal of Engineering Mathematics, 23:95-117.

Yu, Y. S. and Ursell, F., 1961, "Surface Waves Generated by an Oscillating Circular Cylinder on Water of Finite Depth: Theory and Experiment". J. Fluid Mech., 11:529-551.

Drimer, Agnon and Stiassnie (1992) used a simplified model based on the eigenfunction expansion to analyze the behavior of a rectangular breakwater. In Fig. 16 we present the added mass $\bar{\mu} = \mu h_e^2 / \rho$ and the damping coefficient $\bar{\lambda} = \lambda h_e^2 \sqrt{h/g} / \rho$ for half width to draft = 1.0 and water depth / draft = 0.7, in the same dimensional form of Drimer, Agnon and Stiassnie to be easily comparable. The results are in good agreement; in much better agreement with the numerical results showed in their paper.

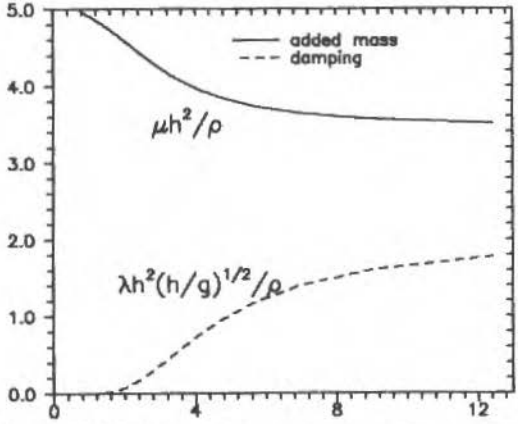

Fig. 16 Added Mass and Damping Coefficient for a Breakwater

References

Bai, K. J., 1977, "The Added Mass of Two-dimensional Cylinders Heaving in Water of Finite Depth". J. Fluid Mech., 81:85-105.

Bai, K. J. and Yeung, R. W., 1974, "Numerical Solutions to Free Surface Flow Problems". In Tenth Symposium on Naval Hydrodynamics, Cambridge, Mass..

Chung, J. S., 1977, "Forces on Submerged Cylinders Oscillating Near a Free Surface". J. Hydronautics, 2:100-105.

Drimer, N., Agnon, Y. and Stiassnie, M., 1992, "A Simplified Analytical Model for a Floating Breakwater in Water of Finite Depth". Applied Ocean Research, 14:33-41.

Esperança, P. T. T., 1993, "Sobre o Comportamento Hidrodinâmico de Corpos Proximos à Superfície Livre". PhD thesis, Programa de Eng. Oceânica/Coppe, Universidade Federal do Rio de Janeiro.

Frank, W., 1967, "On the Oscillation of Cylinders in or Below the Free Surface of Deep Fluids". Report 2375, Naval Ship Res. & Dev. Center, Bethesda, MD.

Grim, 0., 1953, "Berechnung Der Durch Schwingungen Eines Schiffskörpers Erzeugten Hydrodynamischen Kräfte". Jb. Schiffbautech. Ges., 47:277-296.

Keil H., 1974, "On the Oscillation of Cylinders in or Below the Free Surface of Deep Fluids". Report 305, Institut fiir Schiffibau Hamburg, Hamburg, Germany.

Mclver, P. and Evans, D. V., 1984, "The Ocurrence of Negative Added Mass in Free Surface Problems Involving Submerged Oscillating Bodies". J. Eng. Math., 18:7-22.

Mclver, P. and Linton, C. M., 1991, "The Added Mass of Bodies Heaving at Low Frequency in Water of Finite Depth". Applied Ocean Research, 13:12-17.

Newman, J. N., Sortland, B. and Vinje, T., 1984, "Added Mass and Damping of Rectangular Bodies Close to the Free Surface". J. Ship Res., 28:219-225.

Ogilvie, T. F., 1963, "First- and Second-order Forces on a Cylinder Submerged Under a Free Surface". J. Fluid Mech., 16:451-472.

Sayer, P. and Ursell, F., 1976, "On the Virtual Mass, at Long Wavelengths, of a Half-immersed Circular Cylinder Heaving on Water of Finite Depths". In 11th Symposium on Naval Hydrodynamics, London, England.

Tasai, F., 1959, "On the Damping Force and Added Mass of Ships Heaving and Pitching". J. Zosen Kiokai, 105:47-56.

Ursell, F., 1949, "On the Heaving Motion of a Circular Cylinder on the Surface of a Fluid". Quart. Journ. Mech. and Applied Math., 2:218-231.

Ursell, F., 1976, "On the Virtual-mass and Damping Coefficients for Long-waves in Water of Finite Depth". Fluid Mech., 76:17-28.

Yeung, R. W., 1975, "A Hibrid Integral-equation Method for Time-harmonic Free Surface Flows". In Ist International Conference on Numerical Ship Hydrodynamics.

RBCM - J. of the Braz. Soc. Mechanical Sciences
Vol. XVIII - No.4 - 1996 - pp. 374-382

ISSN 0100-7386
Printed in Brazil

Vibration Analysis of Structures Subjected to Boundary Condition Modifications Using Experimental Data

Domingos Alves Rade
Universidade Federal de Uberlândia
Depto. de Ciências Físicas - C.P. 593
38400-902 Uberlândia, MG Brasil

Gérard Lallement
Université de Franche-Comté
Laboratoire de Mécanique Appliquée R. Chaléat
25030 Besançon, France

Abstract

This paper addresses the Analysis of Modified Structures by using experimental data. In particular, modifications of the boundary conditions of the structure by grounding of one or several of its degrees of freedom are considered. Three methods are proposed, which are conceived to obtain the eigenvalues and eigenvectors of more constrained configurations, given the experimental Frequency Response Functions measured on a less constrained configuration. The formulations of the three methods are first presented and their performances are then evaluated through applications to an automotive structure tested in laboratory.
Keywords: Structural Modifications, Modal Analysis, Antiresonances

Introduction

The fundamental problem of the Analysis of Modified Structures (AMS) consists in, given the dynamic characteristics of a structure in a reference configuration, named herein the initial configuration (IC), to determine the dynamic behavior of the so called modified configurations (MCs), which are obtained by introducing in the IC, known modifications of its physical properties, i.e., mass and/or stiffness and/or damping.

Several techniques of AMS, based either on the use of theoretical models, like finite element models, or on the use of experimental data, were developed and became wide spread the last two decades (Snyder, 1986). The latter class of techniques presents, with respect to the former, the advantage of being applicable to complex structures for which an accurate finite element model is difficult to be obtained.

In the present paper, some techniques of AMS, based on the exploitation of experimentally measured frequency response functions (FRFs) are examined. The structural modifications considered are those representing modifications of the boundary conditions of the IC by grounding of one or several of its degrees of freedom (DOFs).

The study reported herein was mainly motivated by the fact that physical grounding of DOFs is, as a rule, one of the major drawbacks arising when performing vibration tests, since the mechanical devices designed to inhibit the motion are never ideally rigid for large frequency bands. This fact can entail serious difficulties. As an example, if the experimental data are to be used for the adjustment of theoretical models, the true flexibilities of the grounding devices, which are in general difficult to estimate, may become additional unknowns of the identification problem.

In this paper, three methods are presented, which enable the real eigensolutions, namely, natural frequencies and normal modes of more constrained, undamped, MCs to be obtained indirectly from the FRFs measured on a less constrained, damped, IC. Since the structural modifications are numerically introduced, ideal groundings of DOFs can be achieved. This way, the difficulties mentioned above can be overcome.

The methods focused in this paper have proved to be very useful in the context of a strategy of enrichment of experimental data, based on the simultaneous exploitation of different boundary condition configurations. This strategy has been associated with some techniques for the adjustment of finite element models and for the identification of structural faults using the dynamic responses (Rade et al., 1994a and Rade, 1994b).

Presented the 13th ABCM Mechanical Enginering Conference - COBEM 95, Belo Horizonte, December 12-15, 1995.
Technical Editorship: COBEM Editorial Committee

Formulations of the Methods

First Method

The first method examined, which is applicable to the case of grounding of a single DOF, exploits the equivalence between the eigensolutions of the MCs and the zeros of the FRFs of the IC. This equivalence is stated by the following assertion (Miu, 1991):

"For undamped structures, the eigensolutions of the MC obtained by grounding the i-th DOF of the IC are equivalent to the antiresonance eigensolutions associated with the zeros of the FRF $H_{ii}(\omega)$ of the IC."

The demonstration that the zeros of point and transfer FRFs are, respectively, the solutions of symmetric and non-symmetric eigenvalue problems, is given by Flannely (1971).

According to the statement above, the natural frequencies of the MC, obtained by grounding the i-th DOF of the IC, denoted herein as ${}^{ii}\omega_v$, $v = {}_{ii}1, 2, \ldots$, are given by the zeros of the FRF $H_{ii}(\omega)$ and the corresponding eigenvectors of the MC, $\{{}^{ii}y_v\}$, $v = {}_{ii}1, 2, \ldots$,are collinear to the i-th column of the dynamic flexibility matrix of the IC, evaluated for each ${}^{ii}\omega_v$. Symbolically:

$$H_{ii}({}^{ii}\omega_v) = 0; \qquad {}^{ii}y_v = [H({}^{ii}\omega_v)]\,\{I_i\},\ v = 1,2,\ldots$$

where $\{I_i\}$ denotes the i-th column of the identity matrix.

Considering the case of lightly damped ICs, it was demonstrated, by using a first order perturbation-type technique (Rade, 1994b), that any FRF of the IC, $H_{ij}^{(d)}(\omega)$, is related to the corresponding FRF of the undamped IC through the expression (in the reminder, superscripts $^{(d)}$ indicate the quantities pertaining to the damped structures)

$$H_{ij}^{(d)}(\omega) = H_{ij}(\omega) + j\,\mathrm{Im}\,[H_{ij}^{(d)}(\omega)], \tag{1}$$

where $\mathrm{Im}\,[H_{ij}^{(d)}(\omega)]$ is of the same order as the arbitrarily small perturbation parameter ε, defined in the sense of the perturbation method. This result allows to obtain a first order approximation for the real eigensolutions of the undamped MC, through the application of the previous statement, by simply operating on the real part of the FRFs of the IC. So, the eigenfrequencies of the undamped MC, defined by grounding of the i-th DOF, are given by the frequency values between two successive eigenfrequencies of the IC which satisfy:

$$\mathrm{Re}\,[H_{ii}^{(d)}({}^{ii}\omega_v)] = 0 \quad ; \quad v = 1, 2, \ldots \tag{2}$$

Alternatively, the eigenfrequencies of the undamped MC can be obtained from the phase of the FRF $H_{ii}^{(d)}(\omega)$ according to:

$$\phi\,[H_{ii}^{(d)}({}^{ii}\omega_v)] = \tan^{-1}\frac{\mathrm{Im}\,[H_{ii}^{(d)}({}^{ii}\omega_v)]}{\mathrm{Re}\,[H_{ii}^{(d)}({}^{ii}\omega_v)]} = \pm\frac{\pi}{2} \tag{3}$$

The corresponding real, non normalized eigenvectors are calculated according to:

$$\{{}^{ii}y_v\} = [\mathrm{Re}\,(H_{ii}^{(d)}({}^{ii}\omega_v)) \ldots \mathrm{Re}\,(H_{ci}^{(d)}({}^{ii}\omega_v))]^T, \quad v = 1, 2, \ldots, \tag{4}$$

where c is the number of instrumented DOFs for which the experimental FRFs of the IC are available.

The practical procedure for calculating the eigensolutions of MCs using this method is given in detail by Rade (1994b).

Second Method

This method can be used for the simultaneous grounding of any number of DOFs. To simplify the presentation, its formulation is presented here for the case of grounding of two DOFs, its extension to the case of grounding of any other number of DOFs being straightforward. The case of undamped structures will be first examined.

Assuming that a submatrix of dynamic flexibilities, measured on a number c of instrumented DOFs is at disposal, two control forces f_i and f_j, are applied on DOFs i and j, respectively, leading the harmonic responses on both these DOFs to vanish. The forcing frequencies and the corresponding displacement shapes which satisfy these conditions are defined respectively as the eigenfrequencies and the eigenvectors of the MC obtained by simultaneously grounding the DOFs i and j.

The pertaining dynamic flexibility relations are written:

$$\begin{bmatrix} [H_{j1}(\omega)] & H_{ji}(\omega) & H_{jj}(\omega) \\ [H_{i1}(\omega)] & H_{ii}(\omega) & H_{ij}(\omega) \\ [H_{l1}(\omega)] & \{H_{li}(\omega)\} & \{H_{lj}(\omega)\} \end{bmatrix} \begin{Bmatrix} \{0\} \\ f_i \\ f_j \end{Bmatrix} = \begin{Bmatrix} Y_j = 0 \\ Y_i = 0 \\ \{y_l(\omega)\} \end{Bmatrix}$$

The partitioning indicated in the equation above leads to the relations:

$$\begin{bmatrix} H_{ji}(\omega) & H_{jj}(\omega) \\ H_{ii}(\omega) & H_{ij}(\omega) \end{bmatrix} \begin{Bmatrix} f_i \\ f_j \end{Bmatrix} = \begin{Bmatrix} 0 \\ 0 \end{Bmatrix} \tag{5}$$

$$\{y_l(\omega)\} = f_i \{H_{li}(\omega)\} + f_j \{H_{lj}(\omega)\} \tag{6}$$

Equations (5) and (6) form an eigenvalue problem. Developing (5), the following frequency equation is obtained:

$$^{ij}D(\omega) = H_{ji}(\omega)^2 - H_{ii}(\omega) H_{jj}(\omega) = 0 \tag{7}$$

The real solutions of (7), noted $^{ij}\omega_\nu$, $\nu = 1, 2, \ldots$ are the eigenfrequencies of the MC. The introduction of the $^{ij}\omega_\nu$ into (5) leads to the following expressions for the ratios between the control forces:

$$\left(\frac{f_j}{f_i}\right)_\nu = -\frac{H_{ji}\left(^{ij}\omega_\nu\right)}{H_{jj}\left(^{ij}\omega_\nu\right)} = \frac{H_{ii}\left(^{ij}\omega_\nu\right)}{H_{ij}\left(^{ij}\omega_\nu\right)} \tag{8}$$

Introducing (8) into (6), the following expression for non-normalized eigenvectors of the MC is obtained:

$$\{{}^{ij}y_v\} = \{H_{li}({}^{ij}\omega_v)\} + \left(\frac{f_j}{f_i}\right)_v \{H_{ij}({}^{ij}\omega_v)\} \tag{9}$$

Consider now the case of lightly damped structures. Taking into account relation (1), the perturbation method, in first order approximation, leads to:

$${}^{ij}D^{(d)}(\omega) = {}^{ij}D(\omega) + j\,\mathrm{Im}\left[{}^{ij}D^{(d)}(\omega)\right], \tag{10}$$

where the imaginary part is again of the same order as the arbitrarily small perturbation parameter ε, defined in the sense of the perturbation method. The eigenfrequencies of the undamped MC satisfy the following relations, which can be considered as homologous to (2) and (3):

$$\mathrm{Re}\left[{}^{ij}D^{(d)}({}^{ij}\omega_v)\right] = 0; \qquad v = 1, 2, \ldots \tag{11}$$

$$\phi\left[{}^{ij}D^{(d)}\left({}^{ii}\omega_v\right)\right] = \tan^{-1}\frac{\mathrm{Im}\left[{}^{ij}D^{(d)}\left({}^{ii}\omega_v\right)\right]}{\mathrm{Re}\left[{}^{ij}D^{(d)}\left({}^{ii}\omega_v\right)\right]} = \pm\frac{\pi}{2}; \qquad v = 1, 2, \ldots \tag{12}$$

The ratios between the control forces and the corresponding real eigenvectors of the undamped MC are given by the expressions:

$$\left(\frac{f_j}{f_i}\right)_v = -\frac{\mathrm{Re}\left[H_{ji}({}^{ij}\omega_v)\right]}{\mathrm{Re}\left[H_{jj}({}^{ij}\omega_v)\right]} = -\frac{\mathrm{Re}\left[H_{ii}({}^{ij}\omega_v)\right]}{\mathrm{Re}\left[H_{ij}({}^{ij}\omega_v)\right]} \tag{13}$$

$$\{{}^{ij}y_v\} = \mathrm{Re}\left(\{H_{li}({}^{ij}\omega_v)\}\right) + \left(\frac{f_j}{f_i}\right)_v \mathrm{Re}\left(\{H_{ij}({}^{ij}\omega_v)\}\right) \tag{14}$$

The practical procedure for calculating the eigensolutions of the MC by using this method is presented in detail by Rade (1994b).

Third Method

The method comprises two steps:

1st) calculation of the FRFs of the MC, from the FRFs of the IC;

2nd) application of a modal identification algorithm to the calculated FRFs of the MC to obtain its eigensolutions.

The formulation of the method is presented here for the case of grounding of a single DOF. Its extension to case of grounding of a larger number of DOFs is immediate. It should be mentioned that analogous formulations have been used by Crowley et al. (1984) and Ewins (1989).

Let:

- i be the DOF for which the harmonic response is to vanish and where the control f_i force is applied;
- k be the DOF where the excitation force f_k is applied.

The harmonic responses at these two DOFs are given by the following flexibility relations:

$$y_i^{(d)}(\omega) = H_{ii}^{(d)}(\omega) f_i + H_{ik}^{(d)}(\omega) f_k = 0 \tag{15}$$

$$y_k^{(d)}(\omega) = H_{ki}^{(d)}(\omega) f_i + H_{kk}^{(d)}(\omega) f_k \tag{16}$$

From equation (15), the ratio between the forces f_i and f_k is written:

$$f_i = -H_{ii}^{(d)^{-1}}(\omega) H_{ik}^{(d)}(\omega) f_k \tag{17}$$

Introducing (17) into (16), the following relation is obtained:

$$\begin{bmatrix} y_k^{(d)}(w) \\ \{y_1^{(d)}(w)\} \end{bmatrix} = \left[\left(-H_{ii}^{(d)}(w) \right)^{-1} H_{ik}^{(d)}(w) \begin{bmatrix} H_{ki}^{(d)}(w) \\ \{H_{1i}^{(d)}(w)\} \end{bmatrix} + \begin{bmatrix} H_{kk}^{(d)}(w) \\ \{H_{1k}^{(d)}(w)\} \end{bmatrix} \right] f_k$$

This last equation is re-written under the form:

$$\{\hat{y}^{(d)}(\omega)\} = \{\hat{H}^{(d)}(\omega)\} f_k \tag{18}$$

Vector $\{\hat{H}^{(d)}(\omega)\}$ contains the FRFs of the MC. The application of a modal identification algorithm to these FRFs leads to the complex eigensolutions of the damped MC, ${}^{1)}\omega_\nu^{(d)}$, $\{{}^{1)}y_\nu^{(d)}\}$; $\nu = 1, 2, \ldots$ When damping is small and the eigenfrequencies are not too close one to the others, fairly accurate approximations to the real eigensolutions of the MC can be obtained by simply taking the real parts of the corresponding complex eigensolutions. In case these requirements are not fulfilled, the real eigensolutions can be either directly identified from the FRFs of the MCs by using special modal identification algorithms (Otte et al., 1993), or be calculated a posteriori from the identified complex eigensolutions by using techniques such those suggested by Zhang and Lallement (1985).

Numerical Applications

In the sequence, the results obtained by applying the three methods to a full-scale muffler of an automotive exhaust line (see Fig. 1), tested in laboratory, are presented.

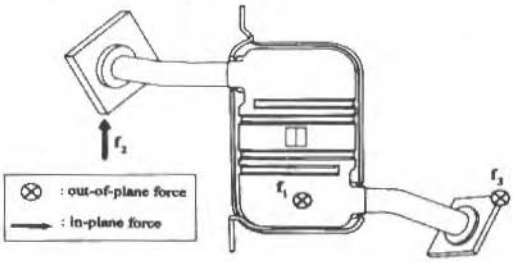

Fig. 1 Scheme of the Test Structure.

The main characteristics of the test procedure are:

- free-free boundary conditions provided by a flexible suspension;
- instrumentation with 36 piezoelectric accelerometers;
- 3 single point random excitations, f_1, f_2 and f_3 applied successively and independently in the locations indicated in Fig. 1;
- acquisition of 507 frequency points in the frequency range [320 Hz; 520 Hz];
- the final values of amplitudes and phases of the FRFs were obtained by calculating the mean values over 150 samples, for each value of the frequency.

Grounding of 1 DOF

The results presented in the following were obtained by using the first and the third methods to calculate the eigensolutions of the MC defined by grounding the DOF where the excitation force f_2 is applied.

Figure 2 shows the FRF $H_{22}(\omega)$ of the IC, superimposed to some FRFs of the MC, which were calculated in the first step of the third method. It can be clearly seen that the antiresonance frequencies of $H_{22}(\omega)$ coincide with the eigenfrequencies of the MC.

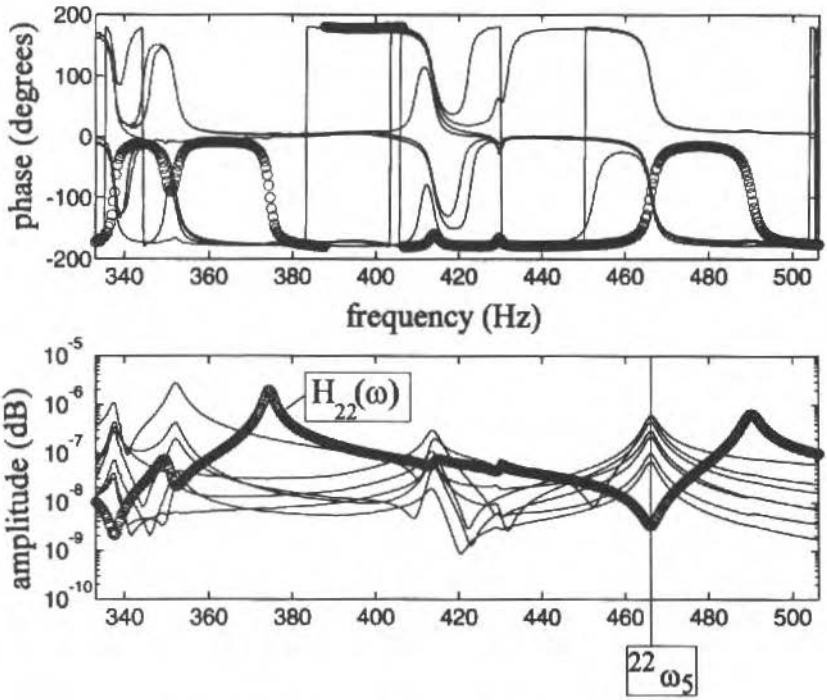

Fig. 2 FRF $H_{22}(\omega)$ of the IC and some FRFs of the MC

Figure 3 allows the comparison of the eigensolutions corresponding to the antiresonance frequency designated in Fig. 2 as ${}^{22}\omega_5$, obtained by using the first and the third methods. A good agreement can be observed between the results provided by both methods. It should be noted that, since the structure is lightly damped and the natural frequencies of the IC are well separated, the real eigenvectors of the associate conservative MC, resulting from the application of the third method, were obtained by taking the real part of the complex eigenvectors identified in the experimental modal analysis procedure. The eigenvectors were normalized so as to render the magnitude of their largest components equal to one.

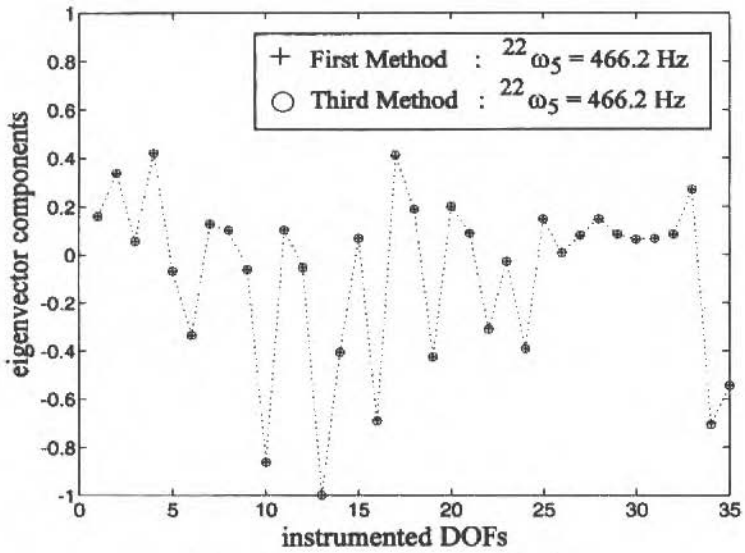

Fig. 3 Eigensolutions Associated with $^{22}\omega_5$

Simultaneous grounding of two DOFs

The second and the third methods were used to calculate the eigensolutions of the MC obtained by simultaneously grounding the DOFs where the excitation forces f_2 and f_3 are applied.

Figure 4 shows the Bode diagram for the frequency equation, defined in Equation (7).

In Figure 5 the eigensolutions corresponding to the frequency $^{23}\omega_4$, indicated in Figure 4, can be compared. Once more, a good agreement between the results provided by both methods is observed.

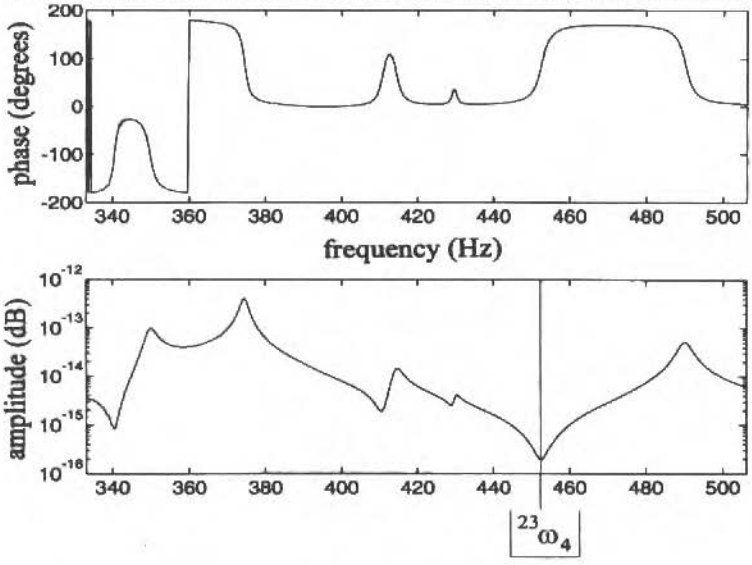

Fig. 4 Bode Diagram for $^{23}D^{(d)}(\omega)$

Acknowledgments

The first author wishes to express his gratitude to the agency CAPES of the Brazilian Ministry of Education and Sports, for the financial support which has enabled him to develop his Ph.D. program in France.

References

Aitrimouch, H., 1993, "Analyse de Structures Mécaniques Modifiées", Thèse de Doctorat, Université de Franche-Comté, UFRST, Besançon, France.

Cogan, S., 1990, "Réanalyse de Structures à Partir de Données Expérimentales : Rigidification et Substitution", Thèse de Doctorat, Université de Franche-Comté, UFRST, Besançon, France.

Crowley, J.R. et al., 1994, "Direct Structural Modification Using Frequency Response Functions", Proceedings of the 2nd International Modal Analysis Conference, pp. 58-65.

Ewins, D.J., 1987, "Vibration Analysis of Modified or Coupled Structures Using F.R.F. Data", Internal Repport, Imperial College of Sciences and Technology, London.

Flannelly, W. G., 1971, "Natural Antiresonances in Structural Dynamics", Internal Report, Kaman Aerospace Corporation, Bloomfield, Connecticut.

Miu, D. K., 1991, "Physical Interpretation of Transfer Function Zeros for Simple Control Systems with Mechanical Flexibilities", Journal of Dynamic Systems, Measurement and Control, Vol. 113, pp. 419-424.

Otte, D. et al., 1993, "Enhaced Force Vector Appropriation Methods for Normal Mode Testing", Proceedings of the 11th International Modal Analysis Conference, pp. 1310-1316.

Rade, D.A., Lallement, G., Cogan, S., 1994a, "Improvement of Structural Change Assessment by Using Multiple Boundary Condition Configurations", Proceedings of the 19th International Seminar on Modal Analysis, Leuven, Belgium.

Rade, D.A., 1994b, "Correction Paramétrique de Modèles Élements Finis - Élargissement de l'Espace de Connaissance", Thèse de Doctorat, Université de Franche-Comté, UFRST, Besançon, France.

Snyder, V. W., 1986, "Structural Modification and Modal Analysis - a Survey", International Journal of Analytical and Experimental Modal Analysis, Vol. 1, n° 1, pp. 45-52.

Zhang, Q., Lallement, G., 1985, "New Method of Determining the Eigensolutions of the Associate Conservative Structures from the Identified Eigensolutions", Proceedings of the 3rd International Modal Analysis Conference, pp. 322-328.

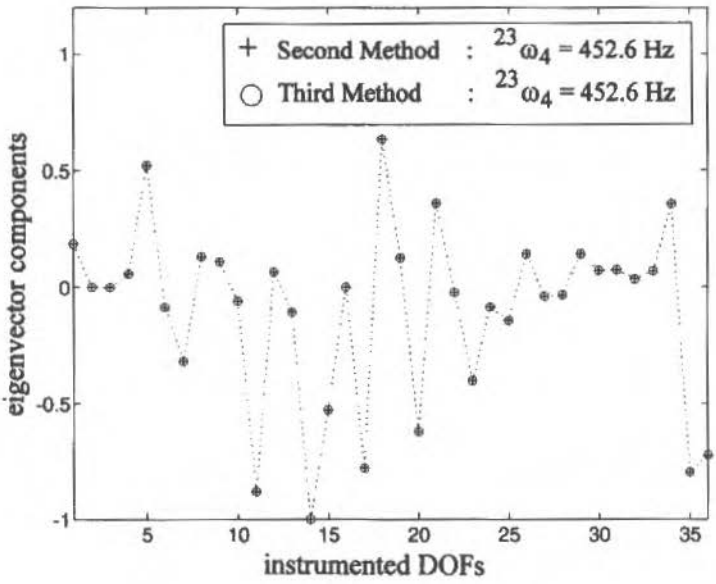

Fig. 5 Eigensolutions Associated with $^{23}\omega_4$

Discussion and Conclusions

The various numerical applications performed have shown that the three methods studied are well adapted to the Analysis of Modified Structures based on the use of experimentally measured FRFs. The accuracy of the results obviously depends upon the quality of those FRFs. Applications performed to numerically simulated structures – for which the exact eigensolutions of the MC are known – have shown that an acceptable accuracy can be achieved even for relatively high levels of simulated experimental noise contaminating the FRFs of the IC (Rade, 1994b).

The good correlation observed between the eigensolutions provided by the different methods does not assure the accuracy of these eigensolutions. Nevertheless, it reveals that, as expected, the different methods perform in an equivalent way, despite the fact that each of them follows clearly distinct calculation procedures. Furthermore, the coherence between the results can be seen, at least, as a necessary condition for their accuracy.

Several authors (Ewins, 1989, and Aitrimouch, 1993) have perceived, when using AMS techniques similar to the third method presented in this paper, the appearance of spurious poles in FRFs of the MCs, which nearly coincide with the eigenfrequencies of the IC. These authors ascribe this phenomenon to: i) the incoherences affecting the measured FRFs, caused by experimental noise and measurement erros, and ii) the numerical ill conditioning of the submatrix of dynamic flexibilities, which has to be inverted in Equation (17), in the case of simultaneous grounding of several DOFs. Contrarily to the reports of the mentioned authors, such spurious poles have not been observed for the experimental test structure examined in this paper. It is believed that this is due to the excellent quality of the FRFs of the IC, for which the values of amplitude and phase were obtained by calculating the mean values over a large number of samples, for each frequency line.

Some aspects concerning the practical application of the methods focused in this paper deserve further investigation and are currently being examined, such as : i) the performance of the second and third methods in the case of simultaneous grounding a larger number of DOFs, and ii) the evaluation of the accuracy of the eigensolutions of the MC calculated from experimentally measured FRFs.

RBCM - J. of the Braz. Soc. Mechanical Sciences
Vol. XVIII - No. 4 - 1996 - pp. 383-394

ISSN 0100-7386
Printed in Brazil

Gerando o Caminho de Corte de Reentrâncias Utilizando Diagramas de Voronoi

Use of Voronoi Diagram for Defining the Cutting Path

Marcos S. G. Tsuzuki
Lucas Antonio Moscato
Universidade de São Paulo
Escola Politécnica
Departamento de Engenharia Mecânica/Mecatrônica
Av. Prof. Mello Moraes, 2231
05508-900 São Paulo, SP Brasil

Abstract

In this work the use of Voronoi Diagram for defining the cutting path is discussed. In this fashion the cutting path is determined in two steps: first, the Voronoi Diagram is created, and second, the cutting path is calculated based on the Voronoi Diagram. A possible implementation for both steps is presented. The main purpose of this algorithm is to facilitate the comprehension of the evolved concepts. Results obtained from a prototype are presented.
Keywords: Pocket Milling, Cutting Path, Voronoi Diagram

Resumo

Neste trabalho realizamos uma rápida introdução, onde destacamos a importância das pesquisas na área de usinagem 2½D. Em seguida apresentamos uma rápida revisão bibliográfica do assunto. Detalhamos a proposta de definir o caminho de corte com base nos diagramas de Voronoi. Assim, a definição do caminho de corte passa a ser feita em duas etapas: primeira, definir o diagrama de Voronoi e, a segunda, definir o caminho de corte propriamente dito. Apresentamos um algoritmo para cada uma das etapas. Estes algoritmos foram desenvolvidos com o principal objetivo de facilitar a compreensão dos conceitos envolvidos. Finalmente, apresentamos alguns resultados obtidos com o protótipo desenvolvido e tiramos algumas conclusões.
Palavras chave: Caminho de Corte, Diagrama de Voronoi, Usinagem de Reentrâncias

Introdução

Os principais tipos de usinagem por comando numérico geralmente são classificados de acordo com o número de eixos controláveis simultaneamente e independentemente um do outro:

- Usinagem 2D: permite o controle de dois eixos translacionais. Logo, a usinagem 2D suporta apenas aplicações planares,
- Usinagem 3D: permite a interpolação linear utilizando todos os três eixos translacionais simultaneamente. Interpolações circulares podem ocorrer apenas em um plano de coordenadas (planos -xy, -yz ou -xz),
- Usinagem 5D: adicionalmente às características da usinagem 3D, dois eixos adicionais de rotação são controláveis.

A maior dificuldade em usinagens 5D e 3D (este último em menor escala) é a necessidade de dados de controle precisos para o controle simultâneo dos vários eixos de movimento. Estes mesmos problemas estão presentes no campo da robótica. Detetar e evitar colisão entre a ferramenta e o "mounting", de um lado, e a peça e o fixador, de outro lado, são problemas matematicamente e algoritmicamente complexos. Devido a estes problemas, a usinagem 5D é utilizada apenas quando não existe nenhuma outra solução possível. Entretanto, usinagem 2D sofre uma série de restrições drásticas que a eliminam de ser uma alternativa prática para usinagem 5D. Este vazio entre os requisitos práticos, de um lado, e as deficiências de programação, de outro, é sanado por uma forma híbrida entre usinagem 2D e usinagem 3D: usinagem 2½D. Em princípio é possível realizar usinagem 3D, utilizando usinagem 2½D. A Figura 1 ilustra os vários tipos de usinagem apresentados.

Manuscript received: October 1995. Technical Editor: Agenor de Toledo Fleury

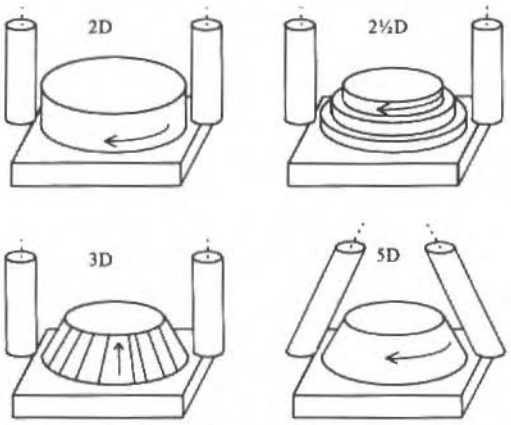

Fig. 1 Os Principais Tipos de Usinagem: 2D, 2½D, 3D e 5D.

A grande maioria dos processos de usinagem industrial pode ser realizada utilizando usinagem 2½D, segundo Held Keppler (1989) mais de 80% de todas as peças mecânicas podem ser usinadas segundo o conceito de usinagem 2½D, ele explica esta afirmação pelos dois aspectos seguintes:

- Surpreendentemente, um grande número de peças mecânicas possui a forma de curvas de nível em terraços, i.e. suas faces de contorno são simultaneamente paralelas ao plano-xy ou constantemente normais ao plano-xy. Por convenção, estes objetos são denominados como 2½ dimensionais.
- Objetos mais complexos - como cavidades com contornos definidos por superfícies esculpidas - são produzidos usualmente por um desbaste 2½D e um acabamento 3D ou 5D.

Desta maneira, concluímos que o domínio de técnicas de usinagem 2½D é de fundamental importância

Revisão Bibliográfica

As técnicas conhecidas para usinagem de reentrâncias podem ser classificadas de acordo com a estratégia de usinagem e pela maneira que o caminho de corte é definido. Apesar do caminho de corte variar de algoritmo para algoritmo existem apenas dois tipos de estratégias de usinagem - vide Fig. 2:

- Usinagem paralela ao contorno, e
- Usinagem paralela a uma direção (zigue zague[1])

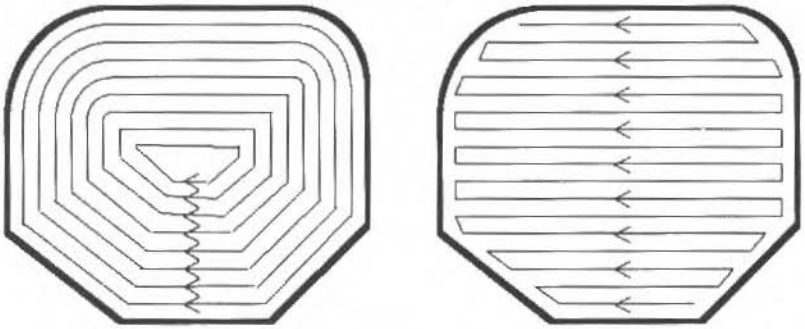

Fig. 2 A Usinagem Paralela ao Contorno e a Usinagem Paralela a uma Direção.

1 Existe uma variação da usinagem zigue-zague chamada de usinagem zigue-zague, onde a usinagem ocorre em apenas um sentido, de modo que a usinagem não ocorra na direção oposta à da árvore da máquina de comando numérico ("spindle").

A estratégia de usinagem paralela ao contorno utiliza o conceito de deslocar elementos do contorno paralelamente para definir o caminho de corte. Isto significa que a área é usinada segundo a forma de uma espiral. A idéia básica da estratégia de usinagem paralela a uma direção é aparentemente simples: após selecionarmos uma linha de referência inicial a usinagem ocorre utilizando segmentos paralelos a esta linha de referência. A principal desvantagem desta estratégia é a necessidade de realizarmos um ciclo de usinagem.

Podemos dividir as estratégias de usinagem paralela ao contorno em duas técnicas principais:

- Definindo o "offset" do contorno a partir do contorno das reentrâncias,
- Definindo o "offset" do contorno a partir de diagramas de voronoi.

Os algoritmos que implementam a primeira técnica estão concentrados na definição de "offsets" sucessivos a partir do contorno original. Este processo é executado segundo os três passos seguintes - vide Fig. 3:

- Para cada elemento do contorno um elemento de "offset" elementar é construído;
- Espaços entre elementos de "offset" consecutivos são preenchidos por arcos de conexão, isto pode resultar em curvas fechadas e, em alguns casos, auto-intersectantes;
- As auto-intersecções das curvas são eliminadas e partes da curva são eliminadas determinando a curva de "offset" final.

O problema principal nesta técnica é a necessidade de determinarmos todas as auto-intersecções. Até o momento, as várias propostas conhecidas não eliminaram a necessidade de interseccionar todos os pares de elementos de "offset" entre si, além de apresentarem complexos algoritmos para eliminar as autointersecções (Suh e Lee, 1990). Vários artigos sobre o assunto já foram publicados, inclusive no Brasil. Ferreira (1993)propõe uma técnica que denominou por "shrinking" que é baseada na teoria de grafos. Cota et al. (1993) propõe uma técnica baseada em subcontornos que são deslocados paralelamente ao contorno original.

Fig. 3 Definindo o "Offset" do Contorno Diretamente a Partir do Contorno da Reentrância, Caso com Várias Auto-Intersecções.

Seguindo uma linha complementar de pesquisadores, Tsuzuki e Miyagi [1991] apresentaram uma técnica para definir o caminho de corte baseando-se em técnicas de reconhecimento de "Form Features" diretamente a partir do Modelo Sólido. As técnicas de reconhecimento de "Form Features" baseiam-se no conceito de que é possível associar um conjunto de comandos de usinagem a uma forma geométrica simples, e é possível interpretar uma forma geométrica complexa como sendo a composição de formas geométricas simples. Este último é um problema que ainda permanece aberto. Toledo et. al. (1993) propuseram uma técnica que fornece um conjunto de interpretações a uma forma geométrica complexa e ficaria a cargo do usuário decidir qual a interpretação mais adequada. Entretanto, o problema de múltipla interpretação de formas geométricas complexas ainda está longe de ser resolvido.

Diagramas de Voronoi

Person, (1978) propôs uma nova e eficiente técnica baseada em duas etapas. Inicialmente, toda a reentrância é dividida em sub-áreas independentes e, em seguida, o caminho de corte é criado diretamente a partir das sub-áreas. Person apresentou em seu artigo a seguinte idéia: selecione um ponto final p entre dois segmentos de caminho de corte consecutivos, e uma observação óbvia, mas importante, é que este ponto possui a mesma distância mínima de dois elementos de contorno e está a uma distância maior de qualquer outro elemento de contorno

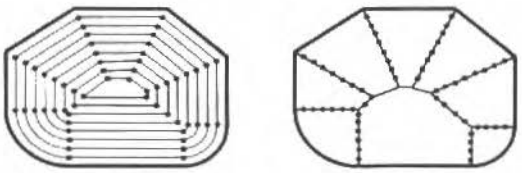

Fig. 4 Propriedade elementar dos pontos finais entre dois segmentos de caminho de corte consecutivos e o respectivo diagrama de Voronoi.

Considerando o conjunto de pontos que possuem esta propriedade obteremos um grafo muito conhecido na geometria computacional como diagramas de Voronoi. Apenas para auxiliar a intuição, consideremos um valor de "offset" inicial que aumentará continuamente até que a curva de "offset" degenere tornando-se um ponto. O conjunto dos pontos p definidos segundo as curvas definidas com os vários valores de "offset" d definem o diagrama de Voronoi. A Figura 4 ilustra este conceito.

Qual será a vantagem em considerar diagramas de Voronoi? A disponibilidade dos diagramas de Voronoi facilita consideravelmente a criação das curvas de "offset". Bastaria definir um algoritmo que defina os pontos extremos de uma curva de "offset" elementar:

- Construa um segmento de "offset" elementar a partir do elemento de contorno, e
- Interseccione o segmento de "offset" elementar com os bissetores que delimitam a área de Voronoi associada ao segmento de "offset".

Se o diagrama de Voronoi for representado de maneira conveniente então este algoritmo poderá ser executado de maneira muito eficiente. Em particular, a idéia originalmente proposta por Person foi que os bissetores devem ser expressados por funções cujos parâmetros representam a distância mínima do bissetor ao contorno da reentrância, ou simplesmente, distância de "offset". Desta maneira, a determinação das intersecções do passo 2 do algoritmo será reduzida a simples avaliação das fórmulas parametrizadas dos bissetores. Segundo Held [1991], ele foi o primeiro a publicar e implementar esta idéia, originalmente proposta por Person, segundo um conceito mais amplo para reentrâncias com contornos complexos.

Determinando Diagramas de Voronoi

As seguintes suposições foram realizadas:

- É comum que os contornos das reentrâncias possuam casos matematicamente problemáticos, como segmentos de linha paralelos, arcos concêntricos, entre outros. Desta maneira, todos estes casos devem ser previstos.
- O contorno da reentrância é definido pela composição de segmentos de linha e arcos de circunferência.

A maioria das máquinas de comando numérico permitem que realizemos apenas interpolações lineares e interpolações circulares. Desta maneira, a segunda suposição está dentro de nossas necessidades do momento.

Parametrização dos Bissetores

Uma vez que a distância de "offset" é muito utilizada durante todo o sistema, tanto no que diz respeito à construção do diagrama de Voronoi como na determinação do caminho de corte, decidimos expressar os bissetores como funções de seu "offset" em relação aos elementos de contorno. Um problema porém surge nesta representação: um bissetor b pode possuir dois pontos P1 e P2 com o mesmo "offset" em relação aos elementos de contorno - vide Fig. 5.

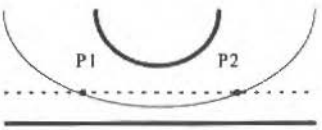

Fig. 5 Pontos P1 e P2 Possuem o Mesmo "Offset".

A solução adotada em nosso sistema foi proposta por Held [1991], ela consiste em dividir os bissetores em dois tipos: bissetores geométricos (as arestas de um diagrama de Voronoi) e bissetores analíticos (bissetores geométricos se dividem nos pontos de extrema distância de "offset" - mínima ou máxima distância).

Como é possível parametrizar um bissetor analítico? Inicialmente, não distinguimos entre um segmento de linha limitado e sua reta suporte, ou entre um arco circular e o círculo que contém o arco. As linhas e círculos são representados pelas sua equações implícitas, e desta maneira é muito fácil representar as curvas de "offset". Para um círculo temos:

$$(x - xc)^2 + (y - yc)^2 = r^2$$

onde o "offset" do círculo - com "offset" t, é fornecido por:

$$(x(t) - xc)^2 + (y(t) - yc)^2 = (r + k.t)^2$$

em que (xc, yc) representam o centro do círculo e r representa o raio do círculo. Por analogia, para a reta:

$$a.x + b.x + c = 0$$

onde $a^2 + b^2 = 0$. O"offset" da reta é fornecido por:

$$a.x(t) + b.y(t) + c + k.t = 0$$

onde a, b e c são os coeficientes normalizados da reta. Em ambas as fórmulas a direção de escorregamento é dada por k. O caso em que k é positivo pode ser interpretado como um engrandecimento do círculo, e opostamente, o caso em que k é negativo significa uma diminuição do círculo. Para a reta, o parâmetro k indica se o "offset" da reta está situado à direita ou à esquerda da reta.

As fórmulas de parametrização para os bissetores (utilizando o "offset" t como parâmetro) pode ser obtida pela solução das equações de intersecção dos elementos de "offset" apresentados. As fórmulas finais já foram apresentadas por Person [1978] e constam do Apêndice 1. Observe que estas fórmulas são válidas apenas para retas que não são paralelas e para círculos que não são concêntricos.

Representando o Diagrama de Voronoi

É necessário definir uma representação adequada para os diagramas de Voronoi. Como o diagrama de Voronoi é um grafo planar conexo, é natural que analisemos representações de grafos conhecidas. As mais apropriadas são: estrutura "winged-edge", proposta por Baumgart [1975] e descrita em detalhes por Mäntylä [1988]; e a estrutura "doubly-connected edge list" (DCEL) proposta por Preparata e Shamos (1988).

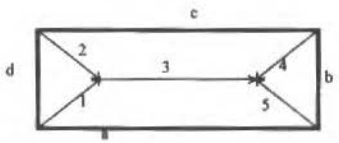

Aresta	ant_2	ant_1	prox_2	prox_1	Face_esq	Face_dir
1	/	/	3	2	d	a
2	/	/	1	3	c	d
3	2	1	5	4	c	a
4	/	/	3	5	b	c
5	/	/	4	3	a	b

Fig 6 Um Diagrama de Voronoi e sua Respectiva Representação. Os ponteiros ant_1, ant_2, prox_1 e prox_2 Representam Arestas que Incidem na Presente Aresta e Face_esq e Face_dir são Ponteiros para Arestas do Contorno que Definem a Presente Aresta

O principal componente de ambas as estruturas de dados é a aresta. Em nossa aplicação uma aresta possui associada a si as seguintes informações: quatro ponteiros para as arestas que incidem na presente aresta e dois ponteiros para os objetos que definem a presente aresta. Desta maneira, cada bissetor está associado ao contorno da reentrância. A Figura 6 ilustra um diagrama de Voronoi e sua respectiva representação.

Cone de Influência

O cone de influência é definido para os elementos de contorno da reentrância. Para um arco de circunferência menor que 180° , o cone de influência é a região delimitada pelo par de raios originários do centro do arco e que passam pelas extremidades do arco sendo a parte hachurada da Fig. 7.a. Para um segmento de reta, o cone de influência é a região delimitada pelas retas normais ao segmento que passam pelas suas extremidades, como ilustrado na Fig. 7.b.

Determinando as Intersecções dos Bissetores

Determinar a intersecção de dois bissetores analíticos b_1 e b_2, com parametrização de coordenadas (x_1, y_1) e (x_2, y_2), significa solucionar um conjunto de equações lineares para t_1 e t_2:

$$x_1(t_1) = x_2(t_2)$$

$$y_1(t_1) = y_2(t_2)$$

Como em nosso algoritmo, t_1 e t_2 devem ser iguais, porque ambos os parâmetros constituem o "offset" do mesmo ponto, determinar a intersecção do bissetor equivale a determinar o ponto equidistante de três objetos (ponto, reta ou círculo). Por exemplo, no caso de dois bissetores definidos por três arcos circulares devemos solucionar o seguinte sistema de equações:

$$(x(t) - xc_1)^2 + (y(t) - yc_1)^2 = (r_1 + k_1.t)^2$$

$$(x(t) - xc_2)^2 + (y(t) - yc_2)^2 = (r_2 + k_2.t)^2$$

$$(x(t) - xc_3)^2 + (y(t) - yc_3)^2 = (r_3 + k_3.t)^2$$

No Apêndice 2 apresentamos os passos para determinar a solução dos vários casos. Como possuímos dois objetos possíveis, foram deduzidas quatro intersecções possíveis: três círculos, dois círculos e uma reta, um círculo e duas retas e, finalmente, três retas. Também foram estudados os casos em que dois círculos são concêntricos, ou, duas retas são paralelas. Geralmente, ao se resolver o sistema não linear, resultamos numa equação quadrática. Desta maneira, há a necessidade de verificarmos qual dos dois pontos realmente pertence ao diagrama de Voronoi. O ponto que pertence ao diagrama de Voronoi deve pertencer ao cone de influência dos três elementos de contorno que definem estes bissetores.

Algoritmo Proposto

Vários algorimos para a definição do diagrama de Voronoi já foram propostos [Held, 1991, Srinivasan e Nackman, 1987, e Preparate e Shamos, 1988]. Entretanto, para este projeto preocupamo-nos em definir um algoritmo de fácil compreensão e que apresentasse os conceitos propostos inicialmente por Person [1978]. A Figura 8 ilustra os vários passos do algoritmo de definição do diagrama de Voronoi, proposto neste trabalho.

O algoritmo é definido abaixo:

i. Todos os ângulos internos maiores que são transformados em arcos de circunferência de raio nulo.

ii. Os bissetores de todos os pares de arestas adjacentes são determinados

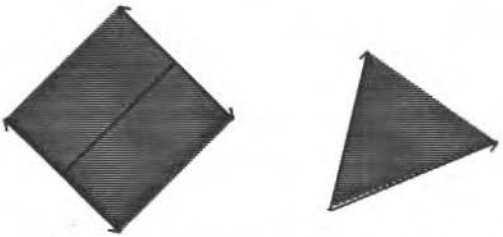

Fig. 7 Cone de Influência de um Arco de Circunferência e de um Segmento de Reta

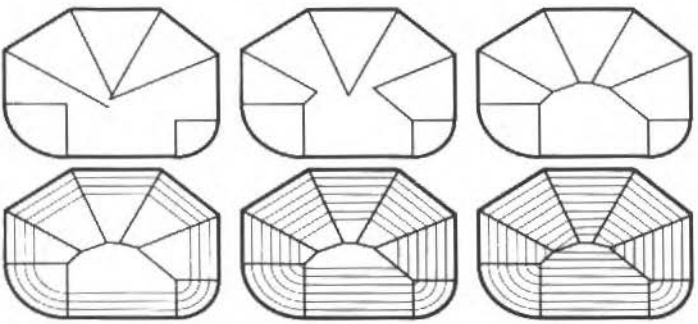

Fig. 8 Os Vários Passos na Definição dos Bissetores que Compõem o Diagrama de Voronoi.

iii. Determinamos a intersecção entre todos os bissetores que possuem uma aresta em comum, e selecionamos a aresta cujo ponto de intersecção possui o menor valor de "offset" t. Cada bissetor possui duas intersecções, uma com cada bissetor adjacente, assim devemos verificar qual o ponto de intersecção está mais próximo do ponto inicial do bissetor. Após esta verificação, o ponto mais próximo é selecionado. Esta verificação é necessária pois em certos casos (bissetor de segunda ordem), o bissetor está direcionado no sentido do maior para o menor "offset". Neste caso, se outro bissetor interseccionar o bissetor em análise entre seus pontos final e inicial, então devemos selecionar o ponto de intersecção mais próximo ao ponto inicial do bissetor. A Figura 9 ilustra um exemplo onde esta verificação se faz necessária

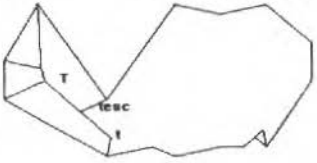

Fig. 9 Exemplo de Criação do Diagrama de Voronoi em que a Verificação Definida no Terceiro Passo 3 do Algoritmo se Faz Necessária. Possuímos tesc> t, mas o Ponto Definido por Tesc é mais Próximo de T que o Ponto Definido por t.

iv. Este lado é removido da lista auxiliar de arestas. Desta maneira, as arestas adjacentes a esta aresta removida, passam a se comportar como se fossem adjacentes.

v. Determinamos o bissetor associado ao novo par de arestas adjacentes que surgiu com a remoção da aresta do terceiro passo. E realizamos novamente este passo, até que possuamos apenas uma única aresta na lista auxiliar de arestas.

O conceito básico neste algorimo é definir o diagrama de Voronoi através da busca de pontos de intersecção entre bissetores com menor valor de "offset" para pontos de intersecção entre bissetores com maior valor de "offset".

Lista Auxiliar de Arestas do Contorno da Reentrância: As arestas do contorno da reentrância estão armazenadas em uma lista auxiliar. Esta lista permite determinarmos o estado atual do algoritmo. Após determinar que dois bissetores devem se interseccionar, removemos a aresta comum aos dois bissetores. Com a remoção da aresta, um novo par de arestas adjacentes surge e utilizamos esta informação para criar um novo bissetor associado a este novo par de arestas adjacentes. E, assim, procedemos continuamente.

Verificação do Funcionamento do Algoritmo: Também implementamos uma função que permite verificar se o algoritmo está caminhando corretamente. Esta função verifica se o ponto de intersecção entre dois bissetores obedece à propriedade abaixo:

$$d(P,L) = d(P,prox\_1) = d(P,prox\_2) < d(P,L)$$

onde L é a aresta comum aos dois bissetores, as arestas Lccw e Lcw são adjacentes à aresta L. O ponto P é o ponto de intersecção entre os dois bissetores e L' são todas as demais arestas do contorno da reentrância. Esta propriedade significa que o ponto de intersecção entre dois bissetores deve estar à mínima equidistância entre as arestas associadas a estes dois bissetores.

Resultados

Conforme apresentamos anteriormente, o diagrama de Voronoi, representado por funções cujos parâmetros representam a distância mínima do bissetor ao contorno da reentrância, permite definir um algoritmo de geração de caminho de corte simples, conforme ilustrado abaixo:

- O usuário especifica um raio de ferramenta qualquer, este raio é adotado como o "offset" inicial. Determinamos o ponto mais interno com o seu respectivo "offset", desta maneira é possível calcular o número de passadas da ferramenta. O contador de passadas é inicializado com 1.
- Através do raio da ferramenta e do número da passada atual, determinamos quais bissetores possuem "offset" inicial menor que o nível do "offset" atual e quais bissetores possuem "offset" final maior que o nível de "offset" atual.
- Monta-se uma lista contendo a aresta, os pontos final e inicial e o "offset" correspondente. Esta lista é ordenada segundo a ordem crescente de identificação da aresta. Desta maneira, o caminho de corte é traçado sempre no sentido anti-horário.

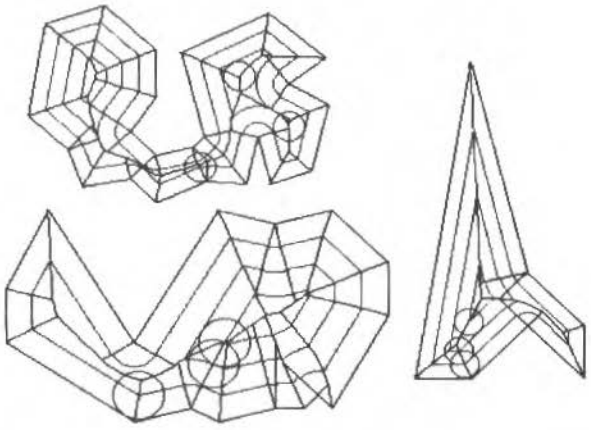

Fig. 10 Diagramas de Voronoi e Caminho de Corte Determinados por Nosso Protótipo.

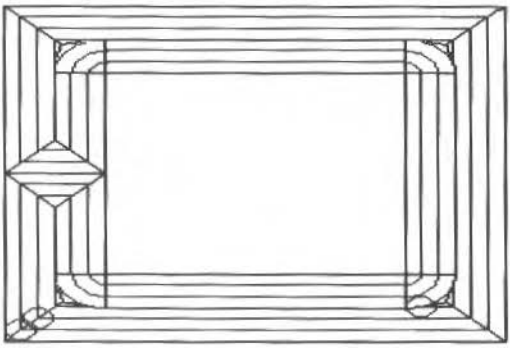

Fig.11 Exemplo do Processamento de Reentrância com Ilha.

O sistema criado a partir deste algoritmo foi testado em um grande número de reentrâncias dos mais diversos tipos que se enquadrassem nas limitações do projeto. Diversos resultados estão ilustrados na Fig. 10. No caso de ilhas, podemos unir o contorno externo da reentrância à ilha. A Fig. 11 ilustra um exemplo de reentrância com ilha.

Conclusões

Os maiores problemas encontrados para o cálculo do diagrama de Voronoi e do caminho de corte estavam relacionados com erros de arredondamento. Para as pessoas que estejam interessadas em desenvolver um sistema semelhante ao que apresentamos neste artigo, podemos fornecer alguns conselhos para solucionar este problema. Primeiro, defina uma tolerância para comparar números reais. E, segundo, defina tolerâncias geométricas para que retas sejam consideradas paralelas e para que circunferências sejam consideradas concêntricas.

Um fator muito positivo dos diagramas de Voronoi, é a definição do caminho de corte em dois passos. A definição do caminho de corte pode ser aprimorada de forma independente do algoritmo que determina o diagrama de Voronoi. Desta maneira, é possível acrescentar um algoritmo que defina a profundidade radial de avanço da ferramenta para que a vibração seja minimizada, conforme apresentado por Tsai et al. (1991).

Agradecimentos

Este projeto foi parcialmente suportado pelo CNPq. Agradecemos aos Engenheiros Cláudio J. F. Alves e Roberto K. Sato pela implementação do protótipo do sistema que gera os diagramas de Voronoi.

Referências

Baumgart, B.G., 1975, "A Polihedral Representation for Computer Vision", In Proc. National Computer Science Conference, pp. 44:589-596, AFIPS Press, Arlington, VA, USA.

Cota, F.E.; Queiroz, A.A.; Filho, E.V.G., 1993, "Usinagens de Cavidades em Formas Arbitrárias em Máquinas Ferramentas de Comando Numérico", Anais do XII Congresso Brasileiro de Engenharia Mecânica, vol. III, pp. 1599-1602, Brasília.

Ferreira, J.C.E.,1993, "An Algorithm for Generating the Tool Paths for Machining Complex 2½D Components", Anais do XII Congresso Brasileiro de Engenharia Mecânica, vol. III, pp. 1587-1590, Brasília.

Held, M., Keppler, J., 1989, "GEOPOCKET - A sophisticated computational geometry soluction of geometrical and technological problems arising from pocket machining", Computer Applications in Production and Engineering - CAPE89, Kimura, F., Rolstadäs, A. (editors), Elsevier Science Publishers B.V. (North Holland), IFIP.

Held, M., 1991, "On the Computational Geometry of Pocket Machining", Springer-Verlag.

Mäntylä, M., 1988, "An Introduction to Solid Modeling". Principles of Computer Science Series, Computer Science Press, Rockville, ML, USA.
Person, H., 1978, "NC machining of arbitrarily shaped pockets", Computer Aided Design, 10(3):169-174, May.
Preparata, F.P., Shamos, M.I., 1988, "Computational Geometry - An Introduction", Texts and Monographs in Computer Science, Springer- Verlag, second edition, October.
Srinivasan, V., Nackman, R., 1987, "Voronoi Diagram for Multiply Connected Polygonal Domains, I: Algorithm", IBM J. of Research and Development, 31(3):361-372, May.
Suh, Y.S., Lee, K.,June 1990, "NC milling tool path generation for arbitrary pockets defined by sculptured surfaces", Computer Aided Design, 22(5):273-284.
Toledo, C.F.M., Garcia, M.B., Tsuzuki, M.S.G., Miyagi, P.E., 1993, "CAPP Automático", Anais do XII Congresso Brasileiro de Engenharia Mecânica, vol. III, pp. 1767-1770, Brasília.
Tsuzuki, M.S.G., Miyagi, P.E., 1991, "Reconhecimento Automático de "Features" Baseado na Representação B-REP", XI Congresso Brasileiro de Engenharia Mecânica, vol. B, pp. 611-614, São Paulo.
Tsai, M.D., Takata, S.; Inui, M., Kimura, F.; Sata, T., 1991, "Operation Planning Based on Cutting Process Models", Annals of the CIRP, Vol 40/1, pp. 95-98.

Apêndice 1

As fórmulas de parametrização para os bissetores (utilizando o "offset" t como parâmetro) podem ser obtidas pela solução das equações de intersecção dos elementos de "offset" reta e círculo. As fórmulas finais já foram apresentadas por Person (1978).

Reta-Reta

$$a_1.x(t) = b_1.y(t) + c_1 + k_1.t = 0$$

$$a_2.x(t) = b_2.y(t) + c_2 + k_2.t = 0$$

onde,

$$a_1^2 + b_1^2 = 1 \quad e \quad a_2^2 + b_2^2 = 1$$

Bissetor Linear

$$x(t) = (b_1 \cdot c_2 - b_2 \cdot c_1)/\Delta + t \cdot (b_1 \cdot k_2 - b_2 \cdot k_1)/\Delta$$

$$y(t) = (a_2 \cdot c_1 - a_1 \cdot c_2)/\Delta + t \cdot (a_2 \cdot k_1 - a_1 \cdot k_2)/\Delta$$

onde

$$\Delta: \; a_1 \cdot b_2 - b_1 \cdot a_2$$

Círculo-Reta

$$(x(t) - xc_1)^2 + (y(t) - yc_1)^2 = (r_1 + k_1.t)^2$$

$$a_2 . x(t) + b_2 . y(t) + c_2 + k_2.t = 0$$

onde

$$a_1^2 + b_1^2 = 1$$

Bissetor Parabólico

$$x(t) = xc_1 - a_2 \cdot h - k_2 \cdot a_2 \cdot t \pm b_2 \sqrt{r_1(t)^2 - h(t)^2}$$

$$y(t) = yc_1 - b_2 \cdot h - k_2 \cdot b_2 \cdot t + \mp a_2 \sqrt{r_1(t)^2 - h(t)^2}$$

onde

$r_1(t) := r_1 + k_1.t$

$h := a_2.xc_1 + b_2.yc_1 + c_2$

$h(t) := h + k_2.t$

Círculo-Círculo

$(x(t) - xc_1)^2 + (y(t) - yc_1)^2 = (r_1 + k_1.t)^2$

$(x(t) - xc_2)^2 + (y(t) - yc_2)^2 = (r_2 + k_2.t)^2$

Bissetor Hiperbólico/Elíptico

$$x(t) = xc_1 - d_x \cdot h - d_x \cdot \Delta \cdot t \pm d_y \sqrt{r_1(t)^2 - h(t)^2}$$

$$y(t) = yc_1 - d_y \cdot h - d_y \cdot \Delta \cdot t \pm d_x \sqrt{r_1(t)^2 - h(t)^2}$$

$r_1(t) := r_1 + k_1.t$

$r_2(t) := r_2 + k_2.t$

$$d := \sqrt{(xc_1 - xc_2)^2 + (yc_1 - yc_2)^2}$$

onde

$dx := (xc_2 - xc_1) / d$

$dy := (yc_2 - yc_1) / d$

$\Delta := (k_2.r_2 - k_1.r_1) / d$

$h := (r_2^2 - r_1^2 - d^2) / (2d)$

$h(t) := (r_2(t)^2 - r_1(t)^2 - d_2) / 2d$

Apêndice 2

Como possuímos dois objetos possíveis, foram deduzidas quatro intersecções possíveis: três círculos, dois círculos e uma reta, um círculo e duas retas e, finalmente, três retas. Considere o caso em que os dois bissetores são defnidos por três arcos de circunferência:

$(x(t) - xc_1)^2 + (y(t) - yc_1)^2 = (r_1 + k_1.t)^2$

$(x(t) - xc_2)^2 + (y(t) - yc_2)^2 = (r_2 + k_2.t)^2$

$(x(t) - xc_3)^2 + (y(t) - yc_3)^2 = (r_3 + k_3.t)^2$

Através de um método de substituição de variáveis, x(t) e y(t) podem ser expressos em termos lineares de t, ou seja $x(t) = \alpha \cdot t + \beta$ e $y(t) \quad \gamma \cdot t + \delta$. Depois de substituirmos essas expressões em uma das fórmulas dadas, um polinômio de segundo grau é obtido. A solução deste polinômio de segundo grau em t nos fornecerá os valores que definem a intersecção dos dois bissetores O caso em que possuímos dois arcos de circunferência e uma reta pode ser solucionado de modo semelhante ao método proposto para o primeiro caso.

O caso em que os dois bissetores são definidos por um arco de circunferência e duas retas:

$$(x(t) - xc_1)^2 + (y(t) - yc_1)^2 = (r_1 + k_1.t)^2$$

$$a_2 . x(t) + b_2 . y(t) + c_2 + k_2 . t = 0$$

$$a_3 . x(t) + b_3 . y(t) + c_3 + k_3 . t = 0$$

O sistema formado pelas duas equações lineares é resolvido pela regra de Cramer. Determinando os valores de α, β, γ e δ recaimos novamente no método proposto no primeiro caso. E para o último caso em que os dois bissetores são definidos por três retas, utilizamos diretamente a regra de Cramer para encontrar a solução do sistema.

RBCM - J. of the Braz. Soc. Mechanical Sciences
Vol. XVIII - No.4 - 1996 - pp. 395-402

ISSN 0100-7386
Printed in Brazil

Projeto de Cascatas de Pás para Turbina Baseado num Método de Progressão no Tempo

Design of Turbine Blade Rows Using a Time-Marching Method

João Eduardo de Barros Teixeira Borges
Luis Manuel de Carvalho Gato
Rui Manoel Roma de Jesus Pereira
Universidade Técnica de Lisboa
Instituto Superior Técnico
Departamento de Engenharia Mecânica
1096 Lisboa Codex Portugal

Abstract

An inverse method based on the iterative use of a direct time-marching code is described. The design input specification used consists of the imposition of the mean tangencial velocity distribution and the desired distribution of blade thickness normal to the blade camber given as a function of the axial distance. The described inverse method was applied to the design of a turbine cascade typical of a rotor blade row representing a high aerodynamic load. This example brings out clearly the relationship between the blade pressure loading and the derivation of the meand velocity distribution used as design input.
Keywords: CFD, Turbomachine, Inverse Methods, Turbine Cascade

Resumo

Descreve-se um método inverso baseado no uso iterativo de um programa de análise do tipo Progressão no Tempo. A especificação de desenho para o escoamento consiste na imposição ao longo da distância axial da distribuição da velocidade tangencial média, e na distribuição desejada da espessura normal à linha de esqueleto. O método de projeto desenvolvido foi aplicado ao desenho de um rotor de uma turbina sujeito a uma carga aerodinâmica elevada. O exemplo mostra claramente a relação existente entre diferença de pressões entre as duas faces da pá e a derivada da velocidade tangencial média utilizada como uma especificação de projeto.
Palavras chaves: CFP, Turbomáquinas, Métodos Inversos, Cascatas de Turbinas.

Introdução

O projetista confrontado com a tarefa de desenhar turbomáquinas eficientes pode recorrer à métodos inversos em vez de utilizar o processo mais simples e usual de adivinhar uma geometria e analisar o escoamento produzido por esta geometria utilizando um código de análise, a fim de verificar se as características do escoamento assim produzido são aceitáveis. As metodologias inversas tratam o problema de forma oposta, na medida em que primeiramente se especificam as características que se deseja para o escoamento, e se calcula em seguida a geometria da cascata de pás que permite obter essas características. Nos últimos anos tem-se evidenciado um interesse renovado no estudo dos métodos inversos, o qual se manifesta no elevado número de artigos publicados e conferências científicas organizadas sobre o assunto - veja-se a título de exemplo Dulikravich (1991, 1992), Van den Braembussche (1990), Slooff (1989). Como resultado de todo este esforço, pode-se dizer-se que surgiram três grandes tendências para a solução do problema inverso: técnicas de otimização, métodos de formulação completamente inversa e uso iterativo de códigos de análise.

Nas técnicas de otimização descreve-se a geometria da coroa de pás em função de alguns parâmetros e procura-se então, no espaço de desenho definido por esses parâmetros geométricos, a combinação de parâmetros que dê as características do escoamento mais próximas possível das desejadas ou que conduza a um ótimo no que diz respeito a uma função-objetivo dependente do escoamento. Uma forma usual de por em prática os métodos de otimização consiste em minimizar as diferenças entre a distribuição desejada de pressão nas superfícies da pá e a calculada para uma dada

Presented at the 13th ABCM Mechanical Engineering Conference - COBEM 95, Belo Horizonte, December 12-15, 1995.
Technical Editorship: COBEM Editorial Committee

combinação de parâmetros. Em contraste, nos métodos de formulação completamente inversa calcula-se diretamente a geometria da coroa de pás que nos dá o escoamento pretendido, utilizando uma formulação do problema que faz uso imediato da informação correspondente às condições desejadas para o escoamento (por exemplo, através da imposição destas condições como condições de fronteira para as equações diferenciais a resolver). A estratégia de usar iterativamente códigos de análise consiste na junção de um simples programa de cálculo do escoamento com um procedimento automático de alteração da geometria da cascata de pás, por forma a atingir os objetivos desejados. Nesta estratégia começa-se por adivinhar uma geometria inicial e calcular o escoamento em torno dela. As diferenças entre o escoamento calculado e o desejado à partida são usadas para modificar a geometria inicial. Em seguida, procede-se a novo cálculo do escoamento e entra-se num ciclo de iterações, até se obter convergência da geometria.

Estas três metodologias têm sido empregues em conjunção com os chamados Métodos de Progressão no Tempo. Estes últimos procuram obter a solução do cálculo do escoamento como o estado final, estacionário, a que se chega por intermédio de uma evolução das variáveis que definem o escoamento no tempo, evolução esta regida pelas equações de Euler para regime transiente.

No presente artigo descreve-se um método inverso baseado no uso iterativo de um programa de análise do tipo Progressão no Tempo. A especificação de desenho para o escoamento consiste na imposição ao longo da distância axial da distribuição da velocidade tangencial média, V_y, (a qual é definida como uma média ponderada pela massa, ao longo de linhas x = constante) e na distribuição desejada da espessura normal à linha de esqueleto.

A motivação para o uso deste tipo de especificação reside no fato de o valor da velocidade média tangencial depender fortemente do valor do ângulo local da linha de esqueleto, de tal forma que será fácil desenvolver um algoritmo automático de alteração da geometria da linha de esqueleto. É de esperar que este algoritmo dê lugar a uma convergência rápida, devido à forte interdependência existente entre o valor da velocidade tangencial média e o ângulo local da linha esqueleto.

A especificação da distribuição da velocidade tangencial média pode soar algo estranho a princípio, mas na realidade já foi utilizada anteriormente, como por exemplo em Novak e Haymann-Haber, 1983; Hawthorne et al., 1984; Pereira, 1993. Como é claramente mostrado em Novak e Haymann-Haber, 1983, a derivada da média ponderada pela massa da velocidade tangencial em ordem à distância axial é proporcional à carga aerodinâmica das pás, definida como sendo a diferença entre os valores da pressão entre o intradorso da pá. Atendendo a este fato, pode afirmar-se que sob o ponto de vista das especificações de projeto, o presente procedimento é equivalente aos métodos que especificam a carga aerodinâmica e a espessura.

Método Inverso

O presente método inverso aproveita a relação existente, por um lado, entre o valor médio da velocidade tangencial ao longo de um passo, ponderado pela massa, Fig. 1,

$$V_y(x) = \frac{\int_{y_{ss}}^{y_{ps}} \rho V_x V_y dy}{\int_{y_{ss}}^{y_{ps}} \rho V_x dy} \qquad (1)$$

e a distribuição da carga aerodinâmica sobre as pás e, por outro lado, entre os valores do ângulo de inclinação da linha de esqueleto e a velocidade tangencial média, V_y. A primeira relação é utilizada para especificar a distribuição, ao longo da corda, da velocidade tangencial média que se pretende seja introduzida pelas pás, enquanto que a segunda é usada no algoritmo de alteração da geometria para atualizar a geometria da pá.

Efetuando um balanço de quantidade de movimento segundo a direção tangencial y, a um volume de controle do tipo [1234] indicado na Fig. 1, facilmente se conclui (ver Novak e Haymann-Haber, 1983, ou Pereira, 1993) que a derivada da velocidade tangencial média em relação à coordenada axial x, é proporcional à carga aerodinâmica sobre as pás. Pode-se dizer que a diferença de pressão entre o extradorso e o intradorso das pás dá origem a uma força tangencial sobre o fluido que é responsável

pela variação da velocidade tangencial média $\bar{V}_y$. Isto mostra que os valores da derivada de $\bar{V}_y$ devem ser nulos quer a montante, que a jusante das pás, por não serem exercidas forças segundo a direção tangencial nesses locais, devido à condição de periodicidade do escoamento.

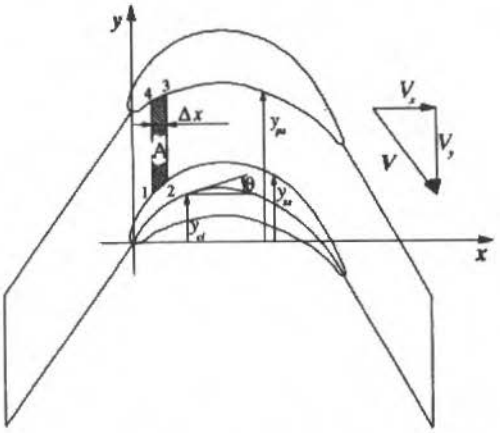

Fig. 1 Cascata de Pás Típica e Linha de Esqueleto do Perfil.

Na posse destes resultados, não é difícil escolher uma evolução apropriada para a evolução de $\bar{V}_y$ ao longo da cascata. De fato, se o objetivo for evitar variações indesejáveis da distribuição de pressão na superfície das pás, será conveniente distribuir uniformemente ao longo da corda a força efetuada pela pá, o que se consegue tendo uma carga aerodinâmica constante, a qual, no nosso caso, se traduz numa derivada constante de $\bar{V}_y$. É óbvio que a carga aerodinâmica e, consequentemente, a derivada da velocidade tangencial média devem apresentar valores nulos nos bordos de ataque e de fuga das pás, tal como acontece a montante e a jusante da cascata. Assim, devem existir regiões de transição na vizinhança dos bordos de ataque e de fuga das pás, onde os valores da derivada de $\bar{V}_y$, variam de zero até ao valor constante desejado.

A distribuição da velocidade tangencial média utilizada no presente trabalho foi escolhida de acordo com o exposto anteriormente, tomando em consideração uma dificuldade adicional originada por, na presente implementação, se ter definido a espessura do perfil como sendo medida na direção normal à sua linha de esqueleto. Consequentemente, exceto se a pá tiver uma linha de esqueleto axial no bordo de ataque, a geometria que resulta da adição da espessura na direção normal à linha de esqueleto apresenta, em geral, uma pequena região que se estende para montante do próprio bordo de ataque. Assim, esta região está, normalmente, sujeita a uma pequena carga aerodinâmica que dá origem a valores não nulos da derivada da velocidade tangencial média junto do bordo de ataque. Outra conseqüência deste fato é que o valor da própria velocidade tangencial média no bordo de ataque é, em geral, um pouco diferente do valor constante verificado a montante da cascata. O mesmo se aplica junto do bordo de fuga, com as necessárias alterações.

Tomando em consideração o exposto anteriormente, a especificação da velocidade tangencial média foi efetuada usando as seguintes expressões:

$$\begin{aligned}
\frac{d\bar{V}_y}{d\xi} &= K\left\{r_1 + (1-r_1)\frac{\xi}{\xi_1}\left(2-\frac{\xi}{\xi_1}\right)\right\}, \quad 0 \le \xi \le \xi_1 \\
\frac{d\bar{V}_y}{d\xi} &= K, \quad \xi_1 \le \xi \le \xi_2 \\
\frac{d\bar{V}_y}{d\xi} &= K\left\{1 + (r_2 - 1)\frac{(\xi-\xi_2)^2}{(1-\xi_2)^2}\right\}, \quad \xi_2 \le \xi \le 1
\end{aligned} \tag{2}$$

onde ξ é a coordenada axial adimensionalisada pela corda das pás medida na direção axial, e r_1, r_2, ξ_1 e ξ_2 são parâmetros cujos valores são escolhidos pelo projetista (com $0 \le r_1 < 1$ e $0 \le r_2 < 1$). A constante K pode ser calculada a partir dos valores $\bar{V}_y$ nos bordos de ataque e de fuga.

A transição entre os valores especificados para a derivada de $\bar{V}_y$ nos bordos de ataque e de fuga, $r_1 K$ e $r_2 K$ e o valor constante na parte central da pá, é efetuada ajustando duas parábolas com derivada nula, respectivamente, em $\xi = \xi_1$ e $\xi = \xi_2$.

A escolha da velocidade tangencial média como parâmetro de projeto justifica-se, não só por permitir controlar de uma forma direta a carga aerodinâmica dos perfis, mas também por facilitar a alteração da geometria do perfil das pás, entre duas iterações. Esta atualização é realizada com base na diferença entre os valores especificados para a velocidade tangencial média e os valores calculados com a geometria da pá na iteração anterior. A expressão utilizada é a seguinte:

$$\mathrm{tg}\theta^{\,n+1} = \mathrm{RF}\left\{\left(\frac{\bar{V}_y(x)}{(\bar{V}_x)_1}\right)_{sp} - \left[\left(\frac{\bar{V}_y(x)}{(\bar{V}_x)_1}\right)^n - \mathrm{tg}\theta^{\,n}\right]\right\} + (1-\mathrm{RF})\,\mathrm{tg}\theta^{\,n}, \qquad (3)$$

onde RF é um fator de relaxação (com valores entre 0,3 e 0,6), θ é o ângulo da linha de esqueleto (Fig. 1), o índice sp indica os valores especificados, o índice 1 refere os valores muito a montante e os índices n e n+1 dizem respeito ao número da iteração.

Atendendo a que $\left(\frac{\bar{V}_y(x)}{(\bar{V}_x)_1}\right)_{sp}$ e $\left(\frac{\bar{V}_y(x)}{(V_x)_1}\right)^n$ determinam os ângulos do escoamento médio, respectivamente, nas geometrias analisadas e naquela que se pretende desenhar, facilmente se conclui que a Eq. (3) se baseia na hipótese de que a diferença entre os ângulos locais do escoamento médio e da linha de esqueleto é a mesma, que para as geometrias analisadas, quer para as geometrias a serem desenhadas. Em geral, esta é uma boa aproximação mas, não sendo exata, são necessárias algumas iterações para obter a geometria final da linha de esqueleto. Depois de conhecer os valores do ângulo da linha de esqueleto, a coordenada y da linha de esqueleto das pás pode ser finalmente calculada integrando numericamente a equação $dy_{cl}/dx = \mathrm{tg}(\theta(x))$.

Resultados

O método de cálculo apresentado na seção anterior foi testado tomando como exemplo o projeto duma coroa de pás de um rotor, com ângulos de entrada e saída de valor elevado, para um escoamento a baixo número de Mach. A relação passo-corda da cascata tem um valor de 0,7 e o número de Mach do escoamento à saída é 0,4, em condições isentrópicas. As condições de projeto são $p_{01} = 2,0$ MPa, $T_{01} = 340$K, $p_2 = 1,791$ MPa, $\beta_1 = 65°$ e o ângulo pretendido para o escoamento à saída é $\beta_2 = -70°$. A espessura do perfil foi definida usando uma distribuição de espessura convencional em projetos de cascatas deste tipo (veja-se Pereira 1993).

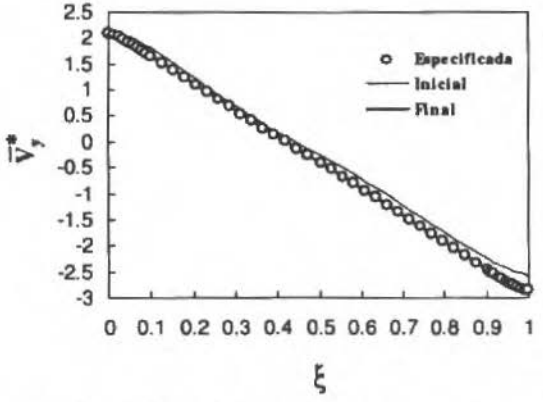

Fig. 2 Velocidade Tangencial Média Especificada, Inicial e Final, em Função da Coordenada Axial.

O programa de análise incorporado no método de desenho das pás utiliza uma formulação explícita, baseada no método da progressão no tempo, e uma discretização em volumes finitos, com uma malha estruturada gerada algebricamente e linhas quase-ortogonais curvas. Os cálculos foram efetuados usando uma malha com 25x141 pontos e quatro níveis de malha múltipla (1x1, 2x2, 4x4, 8x8). O método convergiu ao fim de 15 iterações impondo um valor máximo, inferior a 0,025%, para a variação relativa da coordenada y, entre duas iterações. Como resultado dos cálculos obteve-se um ângulo do escoamento à saída $\beta_2 = -70,2°$ e um valor médio da queda da pressão de estagnação através da cascata que representa cerca de 0,2% do valor da pressão de estagnação à entrada. Estas diferenças são originadas pelos erros numéricos inerentes ao método da progressão no tempo, e são indicativas da precisão com que é efetuado o cálculo do escoamento. Como resultado, após a convergência do método de projeto, o valor obtido para o número de Mach à saída, $Ma_2 = 0,398$, , é ligeiramente menor do que o obtido considerando o escoamento como sendo isentrópico.

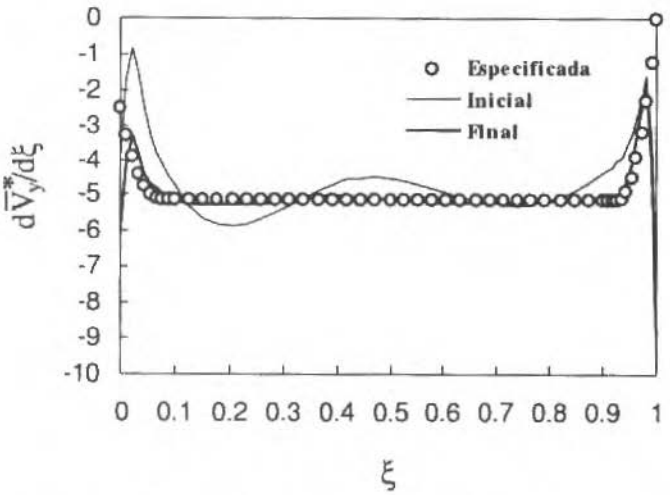

Fig. 3 Derivada da Velocidade Tangencial Média Especificada, Inicial e Final, em Função da Coordenada Axial.

Na Figura 2 mostram-se os valores especificados, iniciais e finais da distribuição da velocidade tangencial média em função da coordenada adimensional ξ. Aqui até o fim desta seção, $\overline{V}_y^*$ representa a velocidade tangencial média adimensionada pela componente axial da velocidade do escoamento muito a montante das pás. Estes resultados indicam que a distribuição desejada para $\overline{V}_y^*$ foi obtida no final do processo iterativo com uma boa precisão. Os resultados de um teste mais exigente, sob este ponto de vista, estão apresentados na Fig. 3, na qual são apresentadas as derivadas das distribuições de velocidade média especificada, inicial e final, em ordem à coordenada axial, em função de ξ. Esta figura revela algumas discrepâncias entre a distribuição imposta para $d\overline{V}^*/d\xi$ e a obtida, após a convergência do método, na proximidade dos bordos de ataque e de fuga dos perfis. Tal como já foi referido, isto deve-se às pequenas cargas aerodinâmicas existentes nestas regiões, em resultado da adoção da definição da espessura das pás na direção normal à linha de esqueleto dos perfis. Esta figura mostra igualmente que entre 7 e 93 por cento da corda da pá especificou-se um valor constante para a derivada de $\overline{V}_y^*$, enquanto que no bordo de fuga se impôs um valor nulo para a carga aerodinâmica. Uma vez que β_1 tem um valor muito elevado, verificou-se ser necessário especificar um valor não nulo para a carga aerodinâmica no bordo de ataque. Nas regiões de transição adotou-se uma evolução parabólica tomando para a Eq. (2), $r_1 = 0,5$, $r_2 = 0$, $\xi_1 = 0,07$ e $\xi_2 = 0,93$.

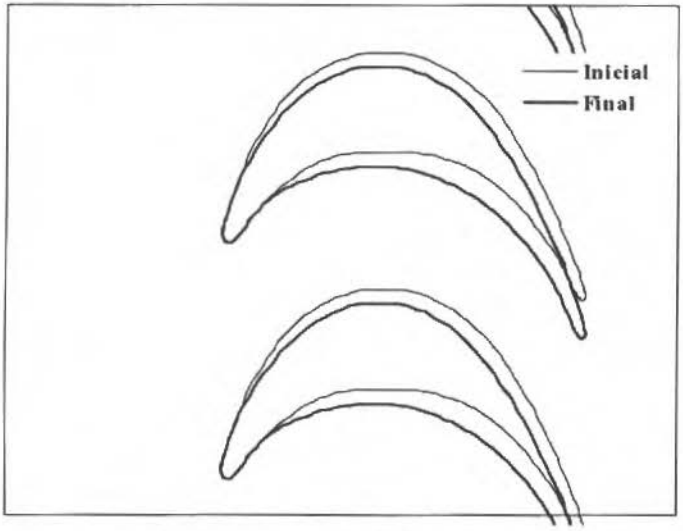

Fig. 4 Geometria Inicial e Final da Cascata

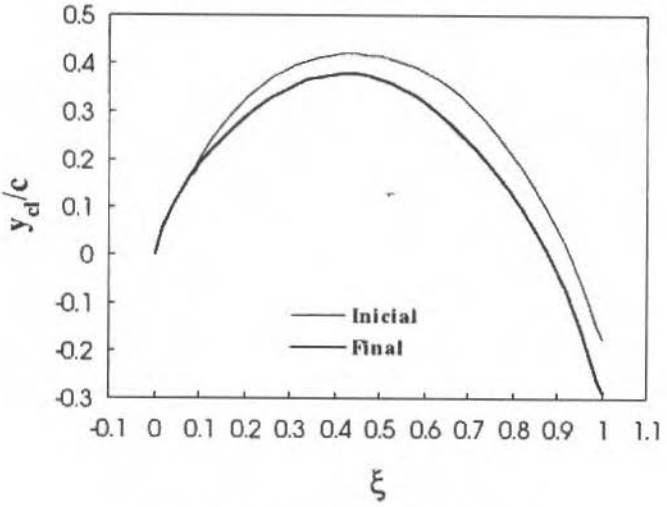

Fig. 5 Linha de Esqueleto Inicial e Final

A Figura 4 ilustra a alteração de geometria sofrida pelos perfis durante o processo iterativo. O perfil inicial foi gerado supondo uma variação linear para a derivada da coordenada y da linha de esqueleto entre $tg(f_1\beta_1)$ e $tg(f_2\beta_2)$, com $f_1 = 1,06$ e $f_2 = 1,0$. Como se pode ver, a geometria obtida após a convergência do método é bastante diferente da geometria de partida. Este exemplo ilustra a capacidade do método para modificar substancialmente a geometria da linha de esqueleto do perfil de forma a aproximar a distribuição calculada de V_y da especificada. No entanto, a Fig. 5 mostra que o método de projeto não modificou apreciavelmente a linha de esqueleto da pá nos primeiros 10% da corda. Este resultado indica que, neste caso, a distribuição de pressão junto ao bordo de ataque é uma função acentuada da distribuição de pressão e, somente em muito menor grau, do ângulo da linha de esqueleto.

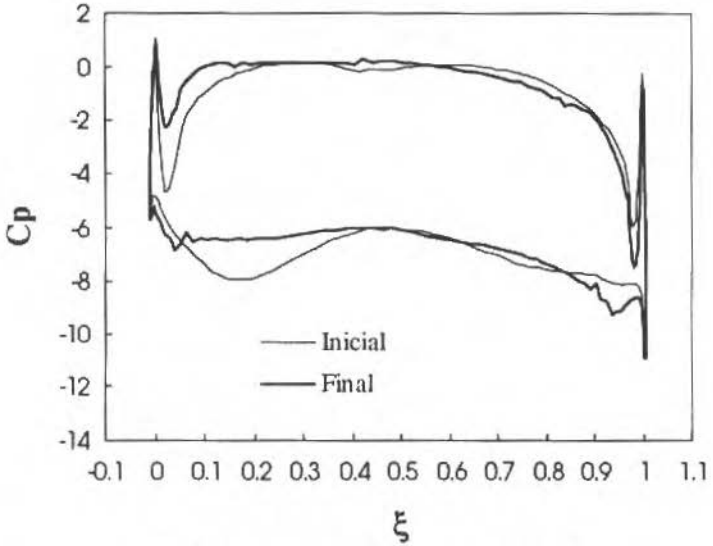

Fig. 6 Distribuição de Pressão em Torno das Pás

A Figura 6 mostra as distribuições de pressão inicial e final, sobre a superfície das pás. O coeficiente de pressão representado na figura foi normalizado pela energia cinética média na cascata, calculada com base nos valores médios das componentes da velocidade dos escoamentos nas regiões muito afetadas, a montante e a jusante, da cascata. Comparando esta figura com as as Figs. 2 e 3, torna-se evidente que se obteve uma carga aerodinâmica constante para $\xi_2 > \xi > \xi_1$, região onde se especificou um valor constante para $d\bar{V}^*/d\xi$. Confirma-se assim que a carga aerodinâmica sobre os perfis apresenta uma evolução semelhante à de $d\bar{V}^*/d\xi$, tal como foi referido na seção anterior.

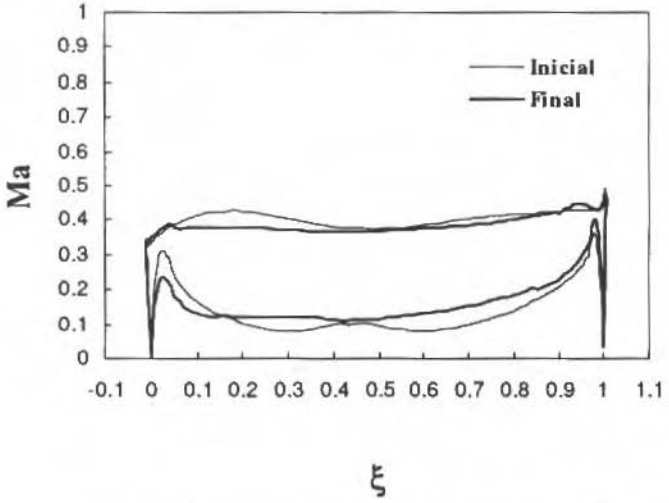

Fig. 7 Distribuição do Número de Mach na Superfície da Pá

A Figura 7 compara as distribuições inicial e final do número de Mach na superfície da pá. Com exceção das regiões muito próximas dos bordos de ataque e de fuga, pode ver-se na figura que a distribuição do número de Mach apresenta uma evolução muito suave e quase-monotônica em resultado da especificação de um valor constante para $d\bar{V}^*/d\xi$ na região central da pá.

Sumário e Conclusões

O presente trabalho descreve um método inverso que usa como dados de entrada uma distribuição da velocidade tangencial média, V_y, juntamente com a imposição da espessura normal da pá. Este método, que foi desenvolvido para o projeto de cascata de pás bi-dimensionais, pode tratar pás com cargas aerodinâmicas elevadas e é baseado no uso interativo de um programa de análise.

Uma vez que a especificação da velocidade tangencial média ($\overline{V}_y$) não tem sido utilizada com freqüência, indicou-se a equivalência desta especificação com a imposição da carga aerodinâmica e mostrou-se que o seu uso é vantajoso no processo de alterar a geometria das pás. Esta alteração foi levada a cabo modificando a linha de esqueleto da pá, seguida da adição da espessura na direção normal à linha de esqueleto.

A metodologia inversa proposta foi aplicada ao desenho de uma cascata de pás para turbina com elevada carga aerodinâmica, com o intuito de mostrar as suas capacidades. Através deste exemplo, mostrou-se que a evolução da carga aerodinâmica é semelhante à variação da derivada de V_y, confirmando assim a afirmação feita acerca da equivalência entre estas duas quantidades. Esta equvalência pode ser utilizada pelo projetista para a escolha da evolução de V_y, permitindo um certo controle sobre a distribuição de pressão nas superfícies da pá. Verificou-se também que esta distribuição de pressões é afetada apreciavelmente pela especificação de espessura normal, exigindo assim que a escolha desta espessura seja feita com cuidado a fim de evitar flutuações indesejáveis na pressão. A escolha apropriada da espessura requer alguma experiência por parte do projetista, o que constitui uma desvantagem deste método, embora esta fato seja comum a todos os métodos que especificam a carga aerodinâmica e a espessura da pá.

Referências

Dulikravich, G. S., 1992, "Aerodynamic Shape Design and Optimization: Status and Trends", Journal of Aircraft, Vol. 29, nº 6, pp. 1020-1027.

Dulikravich, G. S. (Ed.), 1991, "Proceedings of the 3rd International Conference on Inverse Design Concepts and Optimization in Engineering Sciences (ICIDES-III)", Washington D. C.

Hawthorne, W. R. et al., 1984, "Theory of Blade Design for Large Deflections: Part I - Two-dimensional Cascade", ASME Journal of Engineering for Gas Turbines and Power, Vol. 106, pp. 346-353.

Novak, R A. e Haymmann-Haber, G., 1983, "A Mixed-flow Cascade Passage Design Procedure Based on a Power Series Expansion", ASME Journal of Engineering for Power, Vol. 105, pp. 231-242.

Pereira, R. M. R. J., 1993, "Cálculo do Escoamento Compreensível em Cascata de Pás", Tese de mestrado, Instituto Superior Técnico, Universidade Técnica de Lisboa, Lisboa, Portugal.

Slooff, J. W. (Ed.), 1989, "Proceedings of AGARD Specialists' Meeting on Computacional Methods for Aerodynamic Design (Inverse) and Optimization", AGARD CP-463 Löen, Norway.

Vand den Braembussche, R. (Ed.), 1990, "Proceedings of a Special Course on Inverse Methods for Airfoil Design for Aeronautical and Turbomachinery Applications", AGARD-R-780, Rhode-St.-Genèse, Belgium.

RBCM - J. of the Braz. Soc. Mechanical Sciences
Vol. XVIII - No.4 - 1996

ISSN 0100-7386
Printed in Brazil

Abstracts

da Cruz, J. J. and Matuoka, C. A. , "Position Control of Mechanical Manipulators Using the Optimal Root Locus", RBCM - J. of the Braz. Soc. Mechanical Sciences - Vol. 18, No. 4, pp 308-317.

The design of a robust joint independent position control scheme for mechanical manipulators using a pole placement approach based on the Optimal Root Locus is discussed in this paper. Its performance is compared to that of the traditional PD structure, widely used in industrial applications, in situations where the last one is not recommended. The influence of various feedforward schemes is also analysed.
Keywords: Position Control, Mechanical Manipulators, Pole Placement, Optimal Root Locus, Linear Quadratic Regulator.

Barbosa, R. S. and Neto, A. C. "Railway Wheelset Dynamics", RBCM - J. of the Braz. Soc. Mechanical Sciences - Vol. 18, No. 4, pp 318-329 (In Portuguese).

A velocity parametrized railway wheelset model was produced for dynamic behavior analysis. Lateral wheelset excursion related to the track is the first vibration mode. It was observed in the eigen-properties that the wave length of this movement is approximately constant and dependent on the wheel conicity. Modal damping of the first mode is inversely proportional to velocity and becames negative for high speed, resulting on system instability. At low speed, real, distinct and overdamped second mode eigenvalues are inversely proportional to velocity and strongly coupled with contact stiffness. Dynamic wheelset behavior through a variable track trajetory may be observed during model simulation.
Keywords: Railway Wheelset, Dynamic Behavior Analysis, Simulation

Balestieri, J. A. P. and Correia, P. B., "Cogeneration System Design Optimization", RBCM - J. of the Braz. Soc. Mechanical Sciences - Vol. 18, No. 4, pp 330-337.

Cogeneration system design deals with several parameters in the synthesis phase, where not only a thermal cycle must be indicated but the general arrangement, type, capacity and number of machines need to be defined. This problem is not trivial because many parameters are considered as goals in the project.
An optimization technique that considers costs and revenues, reliability, pollutant emissions and exergetic efficiency as goals to be reached in the synthesis phase of a cogeneration system design process is presented. A discussion of appropriated values and the results for a pulp and paper plant integration to a cogeneration system are shown in order to illustrate the proposed methodology.
Keywords: Cogeneration, Optimization, Multiple Programming, Design, Efficient Solutions.

Yu, L. and Righeto A., M., "Recent Advances and Application of Turbulence Depth-Integrated Two-Equation Closure for Modeling Contaminant Discharges", RBCM - J. of the Braz. Soc. Mechanical Sciences - Vol. 18, No. 4, pp 338-354.

This paper presents a brief review and up-to-date development of the depth-integrated turbulence two-equation closure, to be specific, the depth-integrated $\tilde{k}-\tilde{\varepsilon}$ model and $\tilde{k}-\tilde{w}$ model. A numerical simulation of the side discharge of waste heat into natural waters has been taken as an example of the practical application of the $\tilde{k}-\tilde{w}$ model. In addition, the authors also state the existing problems and further development of the present depth-integrated turbulence two-equation models. The main objective of the paper is to integrate the research on the improvement and development of the present depth-integrated turbulence models with the practice of industrial, environmental and sanitary engineering.
Keywords: Turbulence, Depth-Integrated Two-Equation Closure, Contaminant Discharge Modeling.

Esperança, P. T. T. and Sphaier, S. H., "Added Mass and Damping on Bottom-Mounted Rectangular Cylinders", RBCM - J. of the Braz. Soc. Mechanical Sciences - Vol. 18, No. 4, pp 355-373.

Looking for a major comprehension from the reason of the strong variations in the hydrodynamic coefficients of added mass and damping when a two-dimensional body oscillates vertical close to the free surface in finite depth we analyze this problem using eigenfunction expansions. It can make evident the parameters involved on resonances and the behavior for low and high frequencies. Introducing separation of variables the boundary value problem is transformed in an eigenvalue problem of Sturm-Liouville kind. This procedure was used by Yeung (1981) to determine the hydrodynamic coefficients for a truncated vertical cylinder with circular section piercing the free surface oscillating in water of finite depth, Yeung and Sphaier (1989) to consider the interference of vertical walls of a canal in the hydrodynamic coefficients, McIver and Evans (1984) in the

problem of a submerged vertical cylinder oscillating near the free surface and Esperança (1993) for the two-dimensional case.

In the present paper we confirm the occurrence of negative added mass when the body oscillates close to the surface, and obtain finite values of the added mass and damping coefficient in dimensional form for the zero frequency limit as expected. The negative values of the added mass are related to two kind of resonant wave modes occurring close to values of the frequency parameter, wave number times half rectangle width, $m_0^1 a$, is equal to $n\pi$ and $n\pi/2$. For these frequencies the damping coefficient is equal to zero or achieves a local maximum value, and stationary waves characterize the internal flow. Negative added mass for the frequency parameter going to zero is obtained for shallow water, when the emergence of the rectangle is larger than 1/3 of the water depth. A shallow water approach is also presented, allowing us to describe the wave motion for small water depth and clearance. The results derived from the shallow-water solution is in good agreement with the one of the complete solution. Further we present the solution for the case of rectangular cylinder heaving on the free surface and compare the results with results presented by Bai and Yeung (1974), Bai (1977) and by Drimer, Agnon and Stiassnie (1992).

Keywords: Motion of Floating Bodies, Waves, Ship Design, Added Mass and Damping, Botton - Mounted Rectangular Cylinder.

Rade, D., A. and Lallement, G., "Vibration Analysis of Structures Subjected to Boundary Condition Modifications Using Experimental Data", RBCM - J. of the Braz. Soc. Mechanical Sciences - Vol. 18, No. 4, pp 374-382.

This paper addresses the Analysis of Modified Structures by using experimental data. In particular, modifications of the boundary conditions of the structure by grounding of one or several of its degrees of freedom are considered. Three methods are proposed, which are conceived to obtain the eigenvalues and eigenvectors of more constrained configurations, given the experimental Frequency Response Functions measured on a less constrained configuration. The formulations of the three methods are first presented and their performances are then evaluated through applications to an automotive structure tested in laboratory.

Keywords: Structural Modifications, Modal Analysis, Antiresonances

Tsuzuki, M. S. G. and Moscato, L. A., "Use of Voronoi Diagram for Defining the Cutting Path", RBCM - J. of the Braz. Soc. Mechanical Sciences - Vol. 18, No. 4, pp 383-394 (In Portuguese).

In this work the use of Voronoi Diagram for defining the cutting path is discussed. In this fashion the cutting path is determined in two steps: first, the Voronoi Diagram is created, and second, the cutting path is calculated based on the Voronoi Diagram. A possible implementation for both steps is presented. The main purpose of this algorithm is to facilitate the comprehension of the evolved concepts. Results obtained from a prototype are presented.

Keywords: Pocket Milling, Cutting Path, Voronoi Diagram

Borges, J. E. B. T., Gato, L. M. C. and Pereira, R. M. R. J., "Design of Turbine Blade Rows Using a Time-Marching Method", RBCM - J. of the Braz. Soc. Mechanical Sciences - Vol. 18, No. 4, pp 395-402 (In Portuguese).

An inverse based on the iterative use of a direct (analysis) time-marching code is described. The design input specification used consists of an imposition of the mean tangencial velocity distribution and the desired distribution of blade thickness normal to the blade camber given as a function of the axial distance. The described inverse method was applied to the derange of a turbine cascade typical of a rotor blade row representing a high aerodynamic load. This example brings out clearly the relationship between the blade pressure loading an the derivation of the mean velocity distribution used as design input.

Keywords: CFD, Turbomachine, Inverse Methods, Turbine Cascade

Note for Contributors: Articles on Disk

- **Authors are encouraged to submit the final accepted manuscripts on disk, using text editors for Windows or Frame Maker**
- **The disk must be marked with the paper identification number and software used. Two copies of the printout should be included.**

RBCM - J. of the Braz. Soc. Mechanical Sciences
Vol. XVIII - No.4 - 1996

ISSN 0100-7386
Printed in Brazil

JOURNAL OF THE BRAZILIAN SOCIETY OF MECHANICAL SCIENCES
REVISTA BRASILEIRA DE CIÊNCIAS MECÂNICAS

VOLUME XVIII - 1996

Referees - 1996

Abelardo Alves de Queiroz	UFSC
Almir Monteiro Quites	UFSC
Álvaro Costa Neto	USP-EESC
Américo Scotti	UFU
Amilcar Porto Pimenta	CTA-ITA
Antonio Arlindo Guidetti Porto	UNICAMP-CT
Antonio C. P. Brasil Júnior	UnB
Armando Albertazzi	UFSC
Atair Rios Neto	INPE-LAC
Átila Pantaleão da Silva Freire	UFRJ-COPPE
Aureo Campos Ferreira	UFSC
Benedito Di Giacomo	USP-EESC
Benedito Manoel Vieira	CTA-ITA
Breno Pinheiro Jacob	UFRJ-COPPE
Carlos A. Flesch	UFSC
Carlos Alberto de Almeida	PUC-RJ
Carlos Alberto Schneider	UFSC
Carlos Frederico Bremer	USP-EESC
Carlos Henrique Ahrens	UFSC
Celso K. Morooka	UNICAMP - FEM
César Philippi	UFSC
Celso Pupo Pesce	USP-EP
Cláudio S. Kiminami	UFPB
Clóvis Raymundo Maliska	UFSC
Edgar Nobuo Mamiya	UnB
Edison Hiroshi Tamai	USP-EP
Edson Bazzo	UFSC
Edson Gomes	USP-EP
Eduardo Lobo Lustosa Cabral	USP-EP
Eduardo Morgado Belo	USP-EESC
Euclides Mesquita Neto	UNICAMP-FEM
Francisco Domingues Alves de Souza	IPT-DME
Hans Ingo Weber	UNICAMP-FEM
Jair Carlos Dutra	UFSC
João Andrade Carvalho Júnior	INPE
João Batista de Aguiar	USP-EP
José Arnaldo Barra Montevechi	EFEI
José Francisco Ribeiro	UFU
José Guilherme Senna	CTA-IEA
José Jaime da Cruz	USP-EP

RBCM - J. of the Braz. Soc. Mechanical Sciences
Vol. XVIII - No.4- 1996

ISSN 0100-7386
Printed in Brazil

JOURNAL OF THE BRAZILIAN SOCIETY OF MECHANICAL SCIENCES
REVISTA BRASILEIRA DE CIÊNCIAS MECÂNICAS

VOLUME XVIII - 1996

Author Index

M

N

O

P

R

RBCM - J. of the Braz. Soc. Mechanical Sciences
Vol. XVIII - No.4 - 1996 - pp. 411-414

ISSN 0100-7386
Printed in Brazil

FORMULÁRIO DE AFILIAÇÃO

ASSOCIAÇÃO BRASILEIRA DE CIÊNCIAS MECÂNICAS
Av. Rio Branco, 124 - 18º andar - 20040-001 Rio de Janeiro - RJ
Tel.: (021) 221-0438 - Fax.: (021) 222-7128
e-mail: abcmalfs@ omega.lncc.br
CGC 83.431.593/0001-78

INDIVIDUAL

Por favor, preencha os dois lados do formulário.

Nome _____

Endereço Residencial _____

CEP _____ Cidade _____ Estado _____

País _____ Tel.: ( ) _____ Fax: ( ) _____

E-mail _____

Empresa _____

Dept./Divisão _____ Posição _____

Endereço Comercial _____

CEP _____ Cidade _____ Estado _____

País _____ Tel.: ( ) _____ Fax: ( ) _____

E-mail _____

Candidato-me a: ☐ Admissão ☐ Mudança de Categoria

Na categoria de: ☐ Sócio efetivo ☐ Sócio Aspirante

Solicito enviar correspondência para o seguinte endereço:

☐ Comercial ☐ Residencial

Data _____ Assinatura _____

Para uso da ABCM

Aprovado _____ Data _____ Sócio nº _____

FORMAÇÃO E EXPERIÊNCIA PROFISSIONAL

Por favor, liste em ordem cronológica os dados completos de sua formação e experiência profissional. A falta desses dados impedirá o processo de admissão. Obrigado.

FORMAÇÃO ACADÊMICA

Graduação - Área _____ Anos _____ a _____
Instituição _____ País _____

Mestrado - Área _____ Anos _____ a _____
Instituição _____ País _____

Doutorado - Área _____ Anos _____ a _____
Instituição _____ País _____

Outro - Área _____ Anos _____ a _____
Instituição _____ País _____

EXPERIÊNCIA PROFISSIONAL

Empresa _____ Anos _____ a _____
Natureza da atividade _____ Posição _____

Empresa _____ Anos _____ a _____
Natureza da atividade _____ Posição _____

Empresa _____ Anos _____ a _____
Natureza da atividade _____ Posição _____

Indique até um máximo de 8 áreas de acordo com os códigos numéricos do Anexo.

Áreas de Especialização _____

Aplicação _____

Comentários _____

Área de Especialização

Especifique no Formulário de Afiliação os códigos numéricos das suas Áreas de Especialização e de Aplicação (verso).

1000 Fundamentos e Métodos Básicos em Mecânica Teórica e Aplicada
1010 Mecânica do Contínuo
1110 Método dos Elementos Finitos
1120 Método dos Elementos de Contorno
1130 Métodos Assintóticos
1140 Método das Diferenças Finitas
1150 Outro Métodos em Mec. Computacional
1210 Métodos Estocásticos e Estatísticos
1310 Modelagem
1410 Fundamentos de Análise Experimental
1510 Metrologia
1610 Gerência de Projetos
2000 Dinâmica e Vibrações
2110 Cinemática e Dinâmica
2210 Vibrações de Sólidos - Fundamentos
2310 Vibrações - Elementos de Estruturas
2320 Vibrações - Estruturas
2330 Propagação de Ondas em Sólidos
2340 Impacto em Sólidos
2350 Identificação de Parâmetros
2420 Propagação de Ondas em Fluídos
2510 Interação Fluido-Estrutura
2610 Astronáutica - Mec. Celeste e Orbital
2710 Explosão e Balística
2810 Acústica
3000 Controle e Otimização
3110 Projeto e Teoria de Sistemas Mecânicos
3210 Sistemas de Controle Ótimo
3220 Sistemas de Controle Adaptativo
3230 Aplicações em Sistemas e Controle
3310 Robótica
3410 Otimização de Sistemas e Processos
4000 Materiais
4110 Biomateriais
4120 Materiais Metálicos
4130 Materiais Cerâmicos
4140 Materiais Poliméricos
4150 Materiais Conjugados
4210 Conformação Mecânica
4300 Caracterização e Controle Microestrutural
4410 Comp. Mecânico dos Materiais
4420 Comp. Mec. Mat. - Baixas Temperaturas
4430 Comp. Mec. Mat. - Altas Temperaturas
4440 Comp. Mec. Mat. - Carregamto. Variável
4450 Comp. Mec. Mat. - Carregamto. Dinâm.
4500 Mecanismos de Fratura
4600 Mecânica da Fratura
4710 Ensaios Destrutivos
4720 Ensaios Não-Destrutivos
4800 Corrosão
5000 Mecânica dos Sólidos
5010 Elasticidade Linear
5020 Elasticidade Não-Linear
5030 Viscoelasticidade
5040 Plasticidade
5050 Visco-Plasticidade
5060 Mecânica dos Materiais Conjugados
5070 Mecânica dos Meios Porosos
5110 Reologia
5210 Cabos, Hastes e Vigas
5220 Membranas, Placas e Cascas
5230 Estruturas - Geral
5240 Estruturas - Contato com o Solo
5250 Estruturas - Submersas/Semi-submersas
5260 Estruturas - Móveis
5270 Estruturas - Vasos e Contenção
5310 Mecânica dos Solos - Básico
5320 Mecânica dos Solos - Aplicações
5330 Mecânica das Rochas
5410 Efeitos Eletro-Magnéticos em M. Sólidos
5420 Efeitos Térmicos em M. dos Sólidos
5510 Estabilidade de Estruturas
5520 Comportamento após a Flambagem
5530 Estados Limites e Cargas de Colapso
5540 Acomodação e Acúmulo de Dano
5610 Mecânica de Fratura
5650 Tribologia
5655 Atrito e Desgaste
5710 Componentes de Máquinas
5720 Acoplamentos e Juntas Não-Soldadas
5800 Análise Experimental de Tensões
6000 Mecânica dos Fluidos
6010 Reologia
6110 Hidráulica
6210 Escoamento Incompressível
6220 Escoamento Compressível
6230 Escoamento Rarefeito
6240 Escoamento em Meios Porosos
6250 Magneto-Hidrodinâmica e Plasma
6270 Escoamento Multifásico
6310 Camada Limite - Contorno Sólido
6320 Camada Limite - Contorno Livre
6410 Escoamento Interno - Dutos, Canais, etc.
6430 Escoamento com Superfície Livre
6510 Estabilidade de Escoamento
6520 Turbulência
6530 Hidrodinâmica - Veículo de Estrut. Naval
6540 Aerodinâmica
6610 Mec. Fluídos - Aplicações em Máquinas
6650 Lubrificação
6710 Transientes em Fluidos
6810 Téc. Experim. e Visualização Escoamento
7000 Termociências
7010 Termodinâmica
7110 Transp. de Calor - Convec. Monofásica
7120 Transp. de Calor - Convec. Bifásica
7130 Transp. de Calor - Condução
7140 Transp. de Calor - Radiação/Mod. Comb
7150 Transp. de Calor - Dispositivos/Sistemas
7210 Termodinâmica dos Sólidos
7310 Transporte de Massa
7410 Combustão
7420 Combustão em Leito Fluidizado
7510 Acionadores e Dispositivos de Propulsão
8000 Geociências
8010 Micromeritics
8110 Meios Porosos
8210 Geomecânica
8310 Mecânica dos Abalos Sísmicos
8410 Hidrologia, Oceanografia, Meteorologia
9000 Energia e Meio Ambiente
9110 Combustíveis Fósseis
9120 Sistemas Nucleares - Fissão
9125 Sistemas Nucleares - Fusão
9130 Sistemas Geotérmicos
9140 Sistemas Solares
9150 Sistemas Eólicos
9160 Sistemas de Energia Oceânica
9210 Armazenamento de Energia
9220 Distribuição de Energia
9310 Mecânica dos Fluidos Ambiental
9410 Mecânica de Dispositivos de Armazenamento de Resíduo
10000 Biociências
10110 Biomecânica
10210 Ergonomia
10310 Reabilitação
10410 Mecânica nos Esportes

Áreas de Aplicação

Exemplo: um especialista em Mecânica dos Fluídos (família 6000) atuando na área de Turbulência (6520), deverá escolher a Área de Aplicação 350, se estiver trabalhando em Propulsão.

010 Acústica e Controle de Ruído
020 Aplicações em Biociências
030 CAD
040 CAM
050 Componentes de Máquinas
060 Controle Ambiental
070 Controle de Qualidade
080 Criogenia
090 Engenharia e Física de Reatores

100 Engenharia de Petróleo
110 Engenharia Oceanográfica
120 Equipamentos de Processos
130 Equipamentos Industriais
140 Fontes Alternativas de Energia
150 Forjamento
160 Fundição
170 Garantia de Qualidade
180 Indústria Têxtil e Tecnologia Correlata
190 Inspeção e Certificação

200 Instalações Industriais
210 Instrumentação
220 Lubrificação Industrial
230 Mancais e Rolamentos
240 Máquinas Ferramentas
250 Máquinas de Fluxo
260 Máquinas Motrizes
270 Mecânica Fina
280 Metalurgia Geral e Beneficiamento de Minério
290 Metrologia

300 Mineração e Metalurgia Extrativa
310 Óptica
320 Pontes e Barragens
330 Processos de Fabricação
340 Projeto de Estruturas
350 Propulsão
360 Prospecção e Propulsão
370 Servo Mecanismos e Controle
380 Siderurgia
390 Sistemas Hidráulicos

400 Sistemas Pneumáticos
410 Soldagem
420 Solicitações Acidentais - Efeitos de Vento, Sismo, Explosão, Fogo e Inundação
430 Tecnologia de Alimentos
440 Tecnologia Mineral
450 Transporte (excluído veículos)
460 Transmissão de Energia
470 Tratamento Térmico e Termoquímico
480 Tubulações Industriais e Nucleares
490 Usinas Hidrelétricas

500 Usinas Termoelétricas
510 Vácuo
520 Vasos de Pressão, Trocadores de Calor e Equipamentos Pesados
530 Veículos - Terrestres, Espaciais e Marítimos

ISSN 0100-7386
Printed in Brazil

Fourteenth National Heat and Mass Transfer Conference
and
Third ISHMT/ASME Heat and Mass Transfer Conference
December 29-31,1997
First Announcement and Call for Papers

Indian Institute of Technology - Kanpur (India)
Organized under the auspices of
Indian Society of Mechanical Engineering
Co-sponsored by
SESI, IIChE, AESI, Comb Inst (I)
in coorperation with
ASME - American Society of Mechanical Engineers

Deadlines:

15 December, 1996	**- 3 copies of abstract due**
15 January, 1997	**- Abstract Acceptance**
15 April, 1997	**- Full length manuscript due**
15 August, 1997	**- Acceptance after revision**
15 September, 1997	**- Final Mats due at ISHMT HQ**

Prospective authors should send three copies of the abstracts not exceeding 500 words to the coordinating scientist in their zone. The work must be original and unpublished. The abstract should clearly state the objectives of the work, results and conclusions.

The covering letter should contain: (i) Five keywords to describe and categorize the work easily (ii) Name, address, phone number, fax number and e-mail address of the author to whom correspondence should be directed.

3rd International Thermal Energy Congress
Kitakyushu, Japan - July 28 - August 1, 1997

Sponsored by Kyushu University, City of Kitakyushu and
Fukuoka Science & Technology Foundation

Submission of Papers: Three copies of papers, maximum 6 single spaced A4 pages should be submitted to the Congress Coordination prior to December 1, 1996 for reviews. Notification of acceptance will be mailed by January 15, 1997. Author with papers accepted for presentation are requested to submit a manuscript on mats by February 28, 1997 for inclusion in the Congress Proceedings, which will be available at the Congress.

Coordinating Scientist for Both Conferences in
Brazil and South American Countries
Prof. Álvaro T. Prata
Dept. of Mechanical Engineering
Federal University of Santa Catarina
Florianópolis, SC 88040-900, Brazil
Tel.: (+55) (48) 234-5166
Fax: (+55) (48) 234-1519
e-mail: prata@nrva.ufsc.br

Journal of the
Brazilian Society of
Mechanical Sciences

Information for Authors

SCOPE AND POLICY

- The purpose of the Journal of the Brazilian Society of Mechanical Sciences is to publish papers of permanent interest dealing with research, development and design related to science and technology in Mechanical Engineering, encompassing interfaces with Civil, Electrical, Chemical, Naval, Nuclear, Agricultural, Materials, Petroleum, Aerospace, Food, System Engineering, etc., as well as with Physics and Applied Mathematics.
- The Journal publishes Full-Length Papers, Review Papers and Letters to the Editor. Authors must agree not publish elsewhere a paper submitted to and accepted by the Journal. Exception can be made for papers previously published in proceedings of conferences. In this case it should be cited as a footnote on the title page. Copies of the conference referees reviews should be also included. Review articles should constitute a critical appraisal of published information.
- The decision of acceptance for publication lies with the Editors and is based on the recommendations of at least two ad hoc reviewers, and of the Editorial Board, if necessary.

SUBMISSION

- Manuscripts and all the correspondence should be sent to the Editor or, alternatively, to the appropriate Associate Editor.
- Four (4) copies of the manuscript are required. The author should submit the original figures, which will be returned if the paper is not accepted after the review process.
- Manuscripts should be submitted in English or Portuguese. Spanish will also be considered
- A manuscript submitted for publication should be accompanied by a cover letter containing the full name(s) of author(s), mailing adresses, the author for contact, including phone and fax number, and, if the authors so wish, the names of up to five persons who could act as referees.

FORMAT

- Manuscripts should begin with the title, including the english title, the abstract and up to five key words. If the paper's language is not English, an extended summary of about 500 words should be included. The manuscript should not contain the author(s) name(s).
- In research papers, sufficient information should be provided in the text or by refering to papers in generally available Journals to permit the work to be repeated.
- Manuscripts should be typed double-spaced, on one side of the page, using A-4 sized paper, with 2 cm margins. The pages should be numbered and not to excess 24 pages, including tables and figures. The lead author of a RBCM paper which exceeds the standard length of pages will be assessed a excess page charge.
- All symbols should be defined in the text. A separate nomenclature section should list, in alphabetical order, the symbols used in the text and their definitions. The greek symbols follow the English symbols, and are followed by the subscripts and superscripts. Each dimensional symbol must have SI (Metric) units mentioned at the end. In addition, English units may be included parenthetically. Dimensionless groups and coefficients must be so indicated as dimensionless after their definition.
- Uncertainties should be specified for experimental and numerical results.

ILLUSTRATIONS AND TABLES

- Figures and Tables should be referred in consecutive arabic numerals. They should have a caption and be placed as close as possible to the text first reference.
- Line drawings should be prepared on tracing paper or vellum, using India ink; line work must be even and black. Laser print output is acceptable. The drawings with technical data/results should have a boundary on all four sides with scale indicators (tick marks) on all four sides. The legend for the data symbols should be put in the figure as well as labels for each curve wherever possible.
- Illustrations should not be larger than 12 x 17 cm. Lettering should be large enough to be clearly legible (1.5-2.0 mm).
- Photographs must be glossy prints.

REFERENCES

- References should be cited in the text by giving the last name of the author(s) and the year of publication of the reference: either "Recent work (Smith and Jones, 1985) ... or "Recently Smith and Jones (1985) With four or more names, use the form "Smith et al.(1985)" in the text. When two or more references would have the same text identification, distinguish them by appending "a", "b", etc., to the year of publication.
- Acceptable references include: journal articles,dissertations, published conference proceedings, numbered paper preprints from conferences, books, submitted articles if the journal is identified, and private communications.
- References should be listed in alphabetical order, according to the last name of the first author, at the end of paper. Some sample references follow:

Bordalo, S.N., Ferziger, J.H. and Kline, S.J., 1989, "The Development of Zonal Models for Turbulence", Proceedings, 10th ABCM - Mechanical Engineering Conference, Vol. I, Rio de Janeiro, Brazil, pp. 41-44.

Clark, J.A., 1986, Private Communication, University of Michigan, Ann Arbor, MI.

Coimbra, A.L., 1978, "Lessons of Continuum Mechanics", Editora Edgard Blucher Ltda, São Paulo, Brazil.

Kandlikar. S.G. and Shah, R.K., 1989, "Asymptotic Effectiveness - NTU Formulas for Multiphase Plate Heat Exchangers", ASME Journal of Heat Transfer, Vol. 111, pp. 314-321.

McCormak, R.W., 1988, "On the Development of Efficient Algorithms for Three Dimensional Fluid Flow", Journal of The Brazilian Society of Mechanical Sciences, Vol. 10, pp. 323-346.

Silva, L.H.M., 1988 "New integral Formulation for Problems in Mechanics", (in portuguese), Ph.D. Thesis, Federal University of Santa Catarina, Florianópolis, SC, Brazil.

Sparrow, E.M., 1980a, "Forced-Convection Heat Transfer in a Duct Having Spanwise-Periodic Rectangular Protuberances", Numerical Heat Transfer, Vol. 3, pp. 149-167.

Sparrow, E.M., 1980b, "Fluid-to-Fluid Conjugate Heat Transfer for a Vertical Pipe-Internal Forced Convection and External Natural Convection", ASME Journal of Heat Transfer, Vol. 102, pp. 402-407.

ISSN 0100 - 7386

JOURNAL OF THE BRAZILIAN SOCIETY OF MECHANICAL SCIENCES
REVISTA BRASILEIRA DE CIÊNCIAS MECÂNICAS

VOL. XVIII - No. 4 - DECEMBER 1996